

A STUDY OF THE LTE CURVE OF GROWTH METHOD AS USED IN
THE DETERMINATION OF THE SOLAR CHROMIUM ABUNDANCE

by

GARY JOHN GARWOOD

B.S., Kansas State University, 1967

A MASTER'S THESIS

submitted in partial fulfillment of the

requirements for the degree

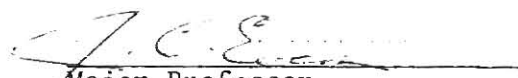
MASTER OF SCIENCE

Department of Physics

KANSAS STATE UNIVERSITY
Manhattan, Kansas

1974

Approved by:


Major Professor

LD
2668

T4
1974

G37
C 2

Document

ACKNOWLEDGMENTS

I would like to thank Dr. John C. Evans for stimulating my interest in the abundance problem. I am grateful for his helpful criticism throughout the course of this study and for the use of his computer codes for the model atmosphere and abundance calculations.

I would also like to thank Kitt Peak National Observatory for providing me with solar line data and computer time for the reduction of the data, and Mr. Larry Testerman for his assistance with the data reduction.

**THIS BOOK
CONTAINS
NUMEROUS PAGES
WITH THE ORIGINAL
PRINTING BEING
SKEWED
DIFFERENTLY FROM
THE TOP OF THE
PAGE TO THE
BOTTOM.**

**THIS IS AS RECEIVED
FROM THE
CUSTOMER.**

TABLE OF CONTENTS

	Page
I. INTRODUCTION	1
II. THE EQUIVALENT WIDTHS	4
III. THE gf-VALUES	14
IV. THE MODEL ATMOSPHERE	29
a) Computation of the Model Atmosphere	29
b) The Microturbulence Model	33
V. THE LINE CALCULATIONS	36
a) Line Depth	36
b) The Line Absorption Coefficient	37
c) The Line Optical Depth	39
d) Line Broadening	40
e) The Theoretical Equivalent Width	43
f) The Theoretical Curve of Growth	44
g) The Abundance Calculation	48
VI. THE ABUNDANCE ANALYSIS	50
a) Objectives of the Analysis	50
b) The Solar Chromium Abundance Resulting from the BF gf-Values and the Analysis for Possible Systematic Errors	53
c) An Outline for Re-doing the Müller and Mutschlecner Study	58
d) Derivation of a Reference Microturbulence Model	59
e) Tests of the Dependence of the Chromium Abundance on the Thermal Model	60
f) The Influence of Systematic Errors Which Depend on Excitation Potential in Both the Empirical and Theoretical Curves of Growth	64
g) The Calculation of an Empirical Set of Neutral Chromium gf-Values	72
h) Tests of the Dependence of the Chromium Abundance on the Microturbulence Model	72
i) The Final Chromium Abundance Derived from the Corrected CB gf-Values and the Müller and Mutschlecner Equivalent Widths	83
j) Conclusions	90
REFERENCES	91

LIST OF TABLES

Table		Page
1	Comparison of Equivalent Widths for the 21 Standard Lines	6
2	Comparison of $\log(gf)$ -Value Measurements	26
3	Abundance Analysis for Beam-Foil gf -Values	51
4	Summary of Linear Least Squares Abundance Analysis for Three Thermal Models with Depth-Independent Microturbulence Model	61
5	Comparison of CB $\log(gf)$ -Values with Corrected $\log(gf)$ -Values	73
6	Summary of Least Squares Abundance Analysis for Five Microturbulence Models with Elste Solar 10 Thermal Model	79
7	Final Cr Abundance Analysis	84
8	Final Cr Abundances Derived for Different Ranges of Lower Excitation Potential at Three Positions on the Solar Disk	89

LIST OF FIGURES

Figure		Page
1	Comparison of Several Sources of Line Equivalent Widths	9
2	Possible Systematic Dependence of Equivalent Width on Line Strength	11
3	Possible Systematic Dependence of Equivalent Width on Wavelength	12
4	Comparison of CB gf-Values with BF gf-Values as a Function of Upper Excitation Potential	17
5	Comparison of CB gf-Values with BF gf-Values as a Function of Upper Excitation Potential after Removal of CB Normalization Function	18
6	Comparison of CB gf-Values with Hill and King gf-Values as a Function of Upper Excitation Potential	20
7	Comparison of CB gf-Values with BF and Shock-Tube Measurements as a Function of Upper Excitation Potential	22
8	Comparison of CB gf-Values with BF and Shock-Tube Measurements as a Function of Upper Excitation Potential after Removal of CB Normalization Function	23
9	Apparent Wavelength Dependence of CB gf-Values Based on BF and Shock-Tube Measurements	24
10	Temperature Distributions for Five Solar Model Atmospheres	31
11	Emergent Intensity as a Function of Photon Energy for Three Solar Model Atmospheres	32
12	Variation of Velocity with Depth for Five Microturbulence Models	35
13	Effect of the Value of Lower Excitation Potential on the Theoretical Curve of Growth	46
14	Effect of Microturbulence on the Theoretical Curve of Growth	47

Figure		Page
15	Empirical Curve of Growth at $\mu = 1.0$ for Lines With BF gf-Values	54
16	Dependence of Computed Line Abundance on Wavelength for 34 Lines with BF gf-Values	55
17	Dependence of Computed Line Abundance on Upper Excitation Potential for 34 Lines with BF gf-Values	56
18	Dependence of Computed Line Abundance on Equivalent Width for 34 Lines with BF gf-Values	57
19	Effect on Computed Abundance of Using Wrong Lower Excitation Potential to Calculate Theoretical Curve of Growth	66
20	Empirical Curve of Growth for 116 Cr I Lines at $\mu = 1.0$ — CB gf-Values Uncorrected	68
21	Empirical Curve of Growth for 116 Cr I Lines at $\mu = 1.0$ — CB gf-Values Corrected for Systematic Errors	69
22	Empirical Curve of Growth for 116 Cr I Lines at $\mu = 0.5$ — CB gf-Values Corrected for Systematic Errors	70
23	Empirical Curve of Growth for 116 Cr I Lines at $\mu = 0.3$ — CB gf-Values Corrected for Systematic Errors	71
24	Dependence of Abundance on Excitation Potential for Five Microturbulence Models	81
25	Dependence of Abundance on Wavelength for Five Microturbulence Models	82
26	Dependence of Abundance on Equivalent Width for Five Microturbulence Models	82

I. INTRODUCTION

Advances in the theory of stellar evolution and nucleosynthesis have led to an increased need for accurate determinations of relative abundances of the elements in stars. In a comprehensive solar abundance study, Goldberg, Müller, and Aller (1960) (hereafter referred to as GMA) used the curve of growth method and the assumption of conditions of local thermodynamic equilibrium (LTE) to compute the abundance of 42 elements. Their method of analysis has become an important model for abundance studies in the sun and other bright stars. However, Pecker (1957a, 1957b) had questioned the validity of the LTE assumption upon which this method is based, and this problem has yet to be resolved (see Athay 1972 for a recent discussion of the problem).

The curve of growth method is most reliable when a large number of lines are used (see Aller 1960, 1963, for a discussion of standard curve of growth techniques). This method of analysis requires: (i) a model atmosphere which agrees well with the observed continuum intensities or fluxes; (ii) a model for small scale mass motions--microturbulence--which intensify the lines (see Ramsey 1973); (iii) a sufficient number of line equivalent widths which cover a range of values and are relatively free of blends; and (iv) reliable laboratory measurements of the oscillator strengths (gf-values) for the lines. The abundance of iron-group elements has been studied extensively in this fashion because of the large number of suitable lines in the solar spectrum.

One of the main sources of error in solar abundance studies has been in the gf-values. The most complete source of gf-values is the extensive compilation by Corliss and Bozman (1962) (hereafter referred to as CB). However, large errors have been found in the CB gf-values for iron (Bridges and Wiese 1970; Wolnik, Berthel and Wares 1970), and for chromium (Wolnik, Berthel,

Carnevale, and Wares 1969; Cocke, Stark, and Evans 1973). The work of Cocke, Stark, and Evans (1973) will hereafter be referred to as CSE.

In this paper, we have made an analysis of the solar chromium abundance, making use of recent data obtained at the Kitt Peak National Observatory (Brault and Testerman 1972) and new gf -values for Cr I (CSE 1973). The main thrust of the investigation is to determine the size of the effect that various systematic errors will produce using the LTE curve of growth technique. In particular, we have analyzed the equivalent widths and gf -values for systematic errors which may depend on wavelength, excitation potential, or equivalent width.

For reference, we have used the work of Müller and Mutschlecner (1964) (hereafter referred to as MM), who attempted to detect deviations from LTE in the solar photosphere by looking for differences in the computed abundances at three limb positions: $\mu = 1.0, 0.5$, and 0.3 (where μ is the cosine of the angular position measured from the center of the disc). They used the CB gf -values in their calculations. We have corrected the CB gf -values for known and suspected systematic errors and repeated the MM calculations using their line equivalent widths.

The effect of the particular choice of thermal and microturbulence models was investigated by doing identical calculations with combinations of three different thermal models and five different microturbulence models. The thermal models were selected by their goodness of fit to the observed continuum intensity data of Labs and Neckel (1968). The abundances derived from individual lines were analyzed for wavelength, excitation potential, and equivalent width dependence, as well as center-to-limb variations.

Section II discusses the equivalent width data. Section III discusses the CB gf -values compared to more recent measurements. Section IV describes

the model atmospheres. Section V outlines the basic steps in the theoretical line calculations. Section VI discusses the analysis of the derived chromium abundance.

II. THE EQUIVALENT WIDTHS

An empirical curve of growth consists of a plot of the logarithm of the gf-value versus the logarithm of the observational equivalent width. This curve is used in the abundance determination process to be described in Section V. The lines used to form this curve are selected on the basis of reliable equivalent widths and laboratory gf-values. The use of blended lines should be avoided except in those cases where the blend can be resolved with reasonable confidence.

In the earlier studies by GMA and MM, the principle sources from which line equivalent widths were measured were the Utrecht Atlas (Minneart, Mulders, and Houtgast 1940), the Michigan Atlas (Mohler, Pierce, McMath, and Goldberg 1950), and an unpublished atlas compiled at the McMath-Hulbert Observatory of the University of Michigan (Mohler and Teske 1961). In their study, MM obtained equivalent widths for 116 Cr I lines at limb distances of $\mu = 1.0$, 0.5, and 0.3.

In the present study, equivalent widths of 60 selected lines were obtained from an early version of the Kitt Peak National Observatory Solar Atlas (Brault and Testerman 1972) in order to estimate the accuracy of the other sets of measurements. This atlas was compiled from data taken with the McMath Solar Telescope. The present atlas consists of direct intensity spectrophotometric tracings of the spectrum at $\mu = 1.0$, and 0.2. However, for the early version, the data for $\mu = 0.2$ was not available.

The spectrograph has a focal length of 13.7 m. and uses a 10-inch Babcock grating of 600 grooves/mm. blazed in the 5th order green (see Pierce 1964, 1969; Brault, Slaughter, Pierce, and Aikens 1971). The data from the spectrograph is digitized and stored on magnetic tape for computer smoothing.

The tracings are generated by the computer in optional scale formats. The line equivalent widths were measured by directly planimetering the line profiles on the tracings. These will hereafter be referred to as the KSU equivalent widths.

The primary concern was that earlier measurements might contain appreciable systematic errors, for which there are several potential sources. One results from underestimating the extent of the wings of the measured line. Another results from unrecognized blending of lines in the crowded regions of the solar spectrum. There is also a tendency to place the continuum too low in regions where the lines are crowded. All of these effects are more pronounced at shorter wavelengths, where the line spacing is small.

We now consider the continuum placement problem. Line profiles are generally normalized with respect to the continuum intensity. This is done by selecting points in the spectrum which are relatively free of absorption lines and assuming that these points are the continuum. This is a satisfactory procedure in the red, but becomes more difficult in practice towards the blue where the crowding of lines is such that few, if any, points between the line profiles are true continuum.

Consequently, abundance analyses using a large number of lines distributed in wavelength, may show wavelength dependence for abundances derived from individual lines. This effect will be discussed further in Section VI.

In order to compare different equivalent width measurements, 21 lines were selected for which at least three determinations were available. These lines, measured at the center of the solar disk, are listed in table 1. In the table, W is the line equivalent width and $\frac{W}{\lambda}$ is called the reduced equivalent width. In this paper, equivalent widths will be expressed as the logarithm of the reduced equivalent width.

TABLE 1

Comparison of Equivalent Widths for the 21 Standard Lines

$$\log \frac{W}{\lambda}$$

RMT No.	Wavelength	KSU	KPNO	MM	MMH	Holweger	GMA
8	5072.92	-5.19		-5.21	-5.21		
10	4496.86	-4.66		-4.70	-4.68		-4.80
	4545.96	-4.70		-4.72	-4.76	-4.73	-4.76
	4580.06	-4.74		-4.73	-4.75		
18	5296.70*	-4.73	-4.74	-4.76	-4.75	-4.78	-4.75
	5348.33*	-4.72	-4.70		-4.75	-4.74	-4.76
	5300.75*	-4.95	-4.95	-4.98	-4.95	-4.98	-4.98
	5247.57*	-4.80	-4.80	-4.82	-4.83	-4.81	-4.84
33	4541.07	-5.19		-5.24	-5.28	-5.26	
	4529.25	-5.28		-5.36	-5.48		
143	4885.95	-5.41		-5.58	-5.61		
144	4836.86*	-5.48	-5.47	-5.45	-5.48	-5.54	
	4814.27*	-5.64	-5.70		-5.60		
	4810.73*	-5.77	-5.80		-5.57		
	4847.19*	-6.38	-6.42		-6.14		
	4825.48*	-5.57	-5.58		-5.43		
145	4737.36*	-4.96	-4.91	-4.91	-4.94	-4.94	
	4730.72*	-5.10	-4.95	-4.99	-5.04	-5.02	
	4724.42*	-5.16	-5.15	-5.17	-5.24		
191	5404.99	-5.56		-5.65	-5.73		
204	5442.41	-5.69		-5.79	-5.80		

* Lines for which $\log \frac{W}{\lambda}$ was evaluated at KPNO by computer reduction of observational data.

Both the KSU (column 3) and KPNO (column 4) values are derived from KPNO (Kitt Peak National Observatory) data. The KSU values are the planimetered measurements from the atlas, while the KPNO values are computer reduced from other data described below. The fifth column in table 1 lists the MM equivalent widths. Column six lists values by Moore, Minneart, and Houtgast (1966), (hereafter referred to as MMH). Column seven contains the equivalent widths by Holweger (1967). The last column lists the GMA values.

The data for the KPNO equivalent widths came from two sources. One is the Fast Center-to-Limb Survey data which is available for wavelengths between 5000 \AA and 6000 \AA at $\mu = 1.0, 0.63, 0.40, 0.25, \text{ and } 0.16$. This data was used for the lines in multiplet 18. The data for the lines in multiplets 144 and 145 was taken from the Fast Survey which is available for $\mu = 1.0$ and 0.2 . The Fast Survey and Fast Center-to-Limb Survey were made in the same manner as the atlas with the exception that they contain fewer scans and thus have a lower signal-to-noise ratio.

The digitized survey data was computer reduced by first resolving any blends with the line of interest. This was accomplished by taking the central intensities of all lines known and suspected in a specified wavelength region and generating a Voigt profile for each line. The damping parameters of these synthetic profiles were then independently adjusted in an iterative manner. After each iteration, the convolution of the individual profiles was compared to the observational profile over the entire interval. This was continued until the best fit to the observed wavelength interval was obtained. The Voigt profile of the line of interest was then integrated over wavelength to obtain the line equivalent width.

Inherent in this procedure is the assumption that all lines are symmetric and that blends can be represented by the convolution of Voigt profiles. These

assumptions are valid to the accuracy required in equivalent width measurements which is on the order of a few percent.

It is interesting to compare the values obtained by the computer to the hand measured equivalent widths, since the computer avoids the possible bias introduced in the visual placement of the continuum and the extension of the line wings. Unfortunately, the amount of computing time required to obtain the KPNO values precludes generating large sets of equivalent width data in this manner.

Both the MM and the MMH equivalent widths have been corrected for blends by the Utrecht method. A description of this procedure is given in the Introduction to Moore, Minneart, and Houtgast (1966). No attempt was made to correct the KSU measurements for unresolved blends. All lines measured either had no apparent blends or contained only clearly recognizable weak lines in the wings. The latter may be handled by assuming the desired line to be symmetric about the line center and reflecting the unblended wing across the bisector of the line core. The profile then maybe extended symmetrically to the continuum, effectively removing the weak blending feature.

Table 1 shows that there is good agreement between the KSU measurements and the KPNO values. The largest difference is 0.15 dex for the λ 4730.72 (multiplet 145) line. However, for the majority, the differences are small. The largest number of independent measurements is available for the lines of multiplet 18, and here the agreement is within 0.06 dex. In figure 1, the MM, MMH, and KPNO values are compared graphically with the KSU values, all measured at the center of the disk. It is seen that the different measurements tend to agree well at the larger equivalent widths, but diverge somewhat for the weaker lines. This is to be expected since strong lines are generally easier to measure than weak lines. Also, differences in methods of treating

**THIS BOOK
CONTAINS
NUMEROUS PAGES
WITH DIAGRAMS
THAT ARE CROOKED
COMPARED TO THE
REST OF THE
INFORMATION ON
THE PAGE.**

**THIS IS AS
RECEIVED FROM
CUSTOMER.**

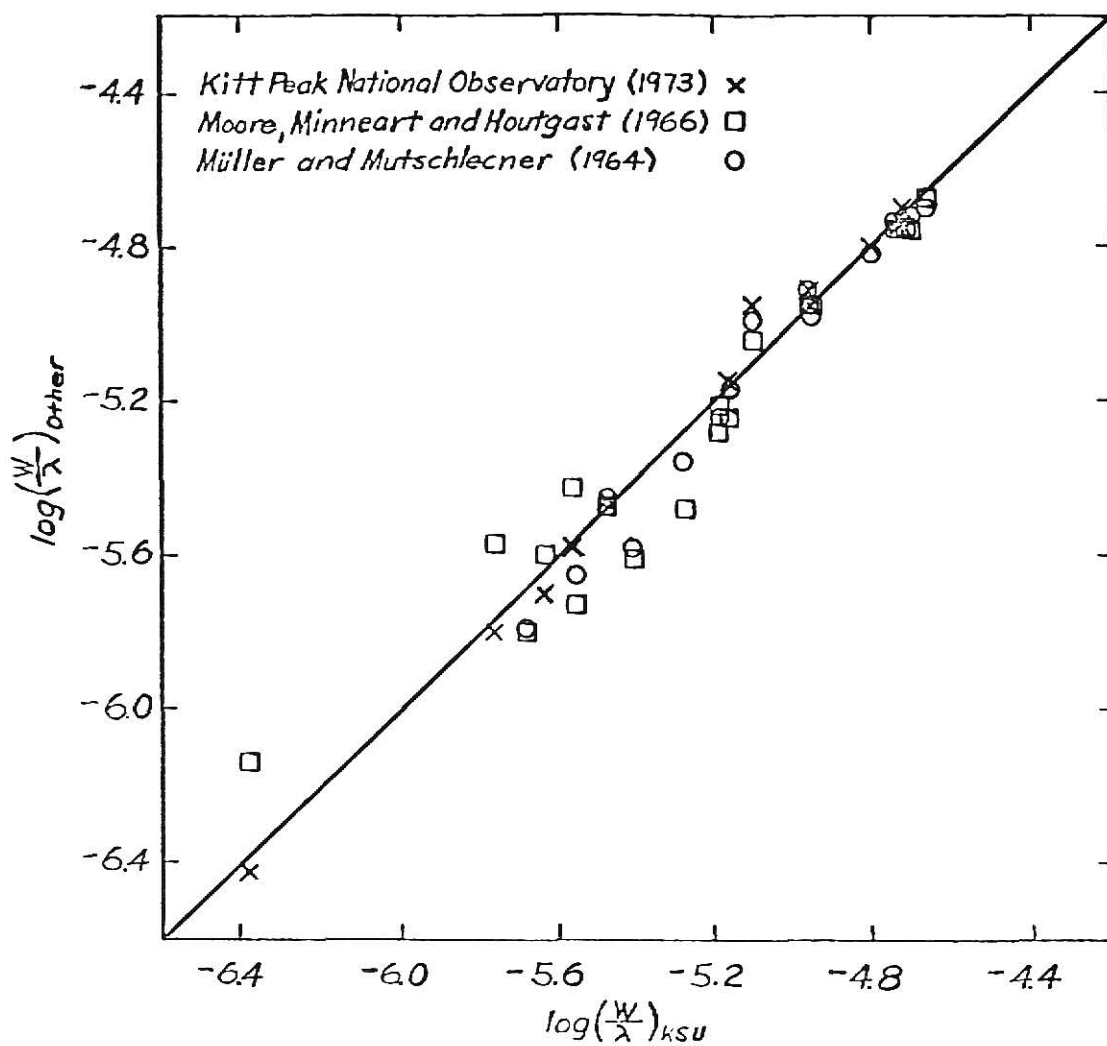


Fig. 1.—Equivalent widths from several different sources (see text for references) are compared using the KSU measurements as a reference. The equivalent widths are given in the form of the logarithm of the reduced equivalent width (W/λ).

weak blends will have less influence on the equivalent width of a strong line.

Indications of possible systematic differences are shown in figures 2 and 3. The ordinate of each figure is the difference between the other values and the KSU value. The lines are the linear least squares fits to the different sets of data, as shown in the figures.

Figure 2 shows a possible dependence on line strength. As in figure 1, it can be seen that the scatter among the different measurements increases with decreasing line strength. The MMH values appear to be too large for weak lines and too small for strong lines. The converse is true for the MM values.

Figure 3 shows an apparent dependence of equivalent width on wavelength. It appears to be negligible for all sets of equivalent widths, but the KSU values tend to decrease towards the blue relative to the others, which may reflect the previously mentioned tendency to place the continuum too low in the blue.

However, the linear trends shown in figures 2 and 3 are of limited significance due to the small number of points on which they are based.

This analysis has revealed no obvious systematic error in the MM equivalent widths when compared to our KSU and KPNO values. From the large scatter in the MMH points in figures 1 through 3, it appears that the MMH equivalent widths may contain some large random errors.

The same analysis was repeated using all 60 KSU measured lines. The results obtained were nearly identical to those for the 21 selected lines. However, for the data sets considered, the number of lines in common was not greatly increased by expanding the comparison data set.

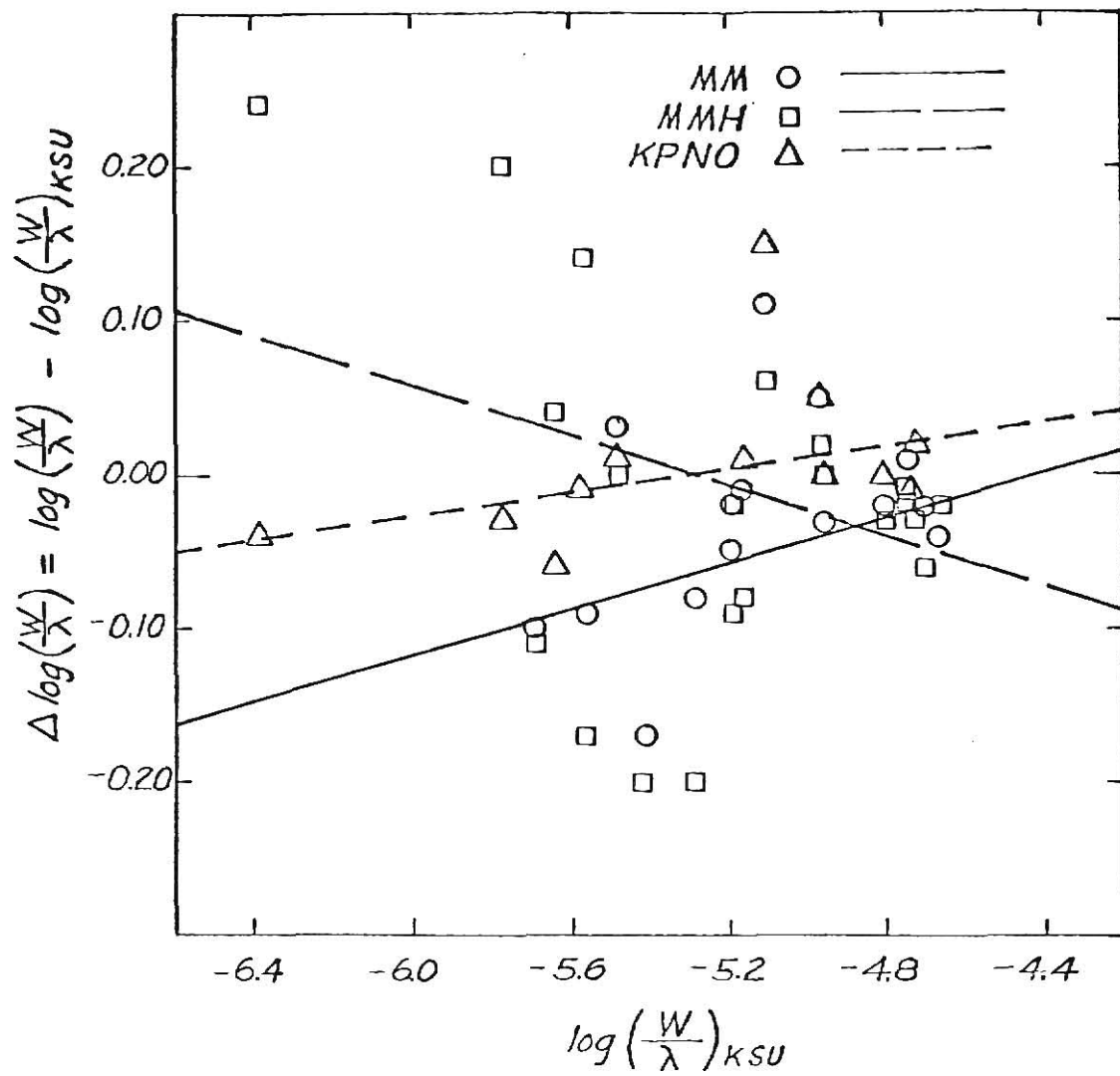


Fig. 2.—A possible systematic error dependent on equivalent width for the MM, MMH, and KPNO measurements, compared to the KSU measurements. The lines are the least squares fits to the different data sets as shown.

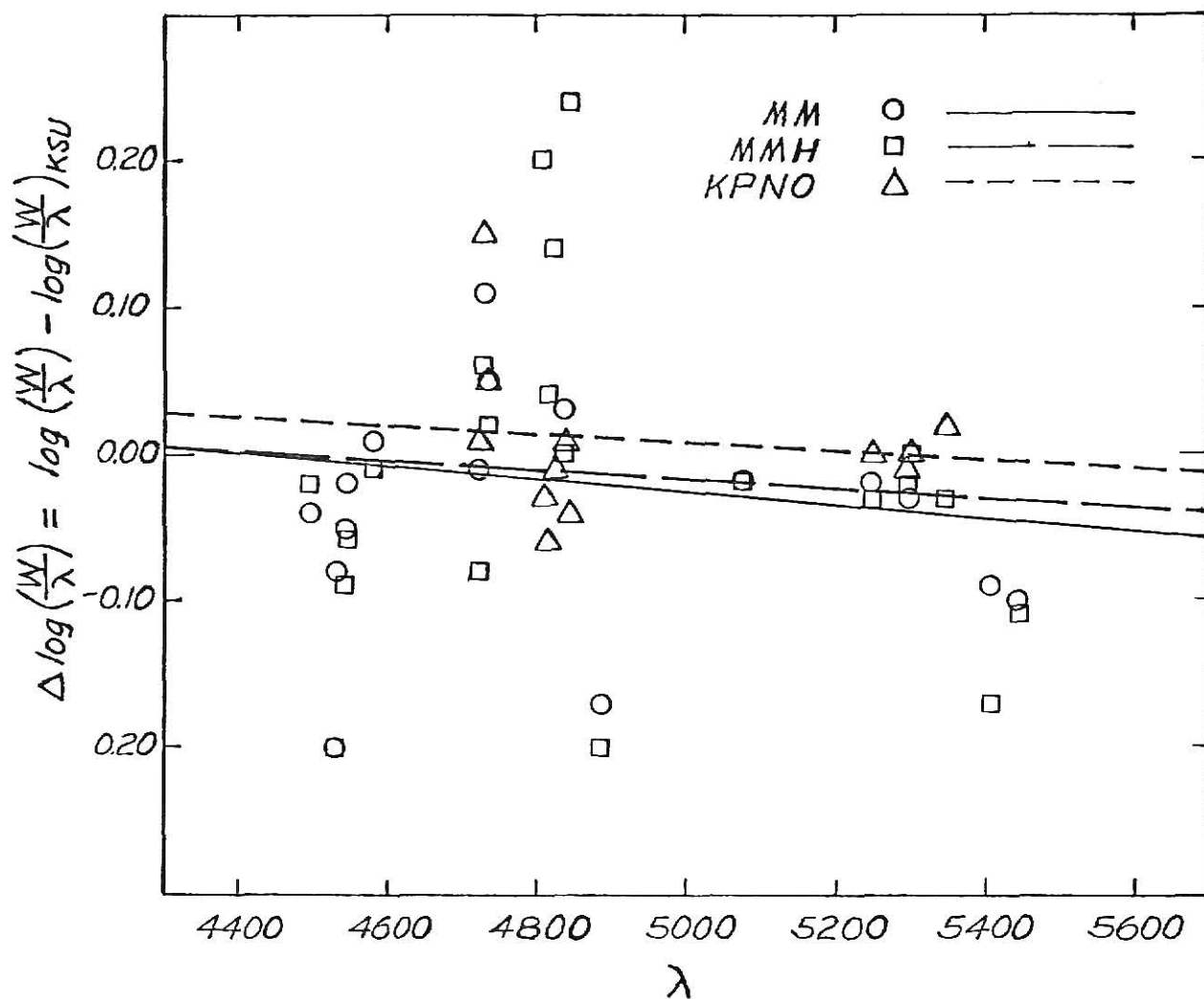


Fig. 3. — A possible systematic error dependent on wavelength for the MM, MMH, and KPNO measurements using the KSU measurements for reference. The Lines are the least squares fits to the data sets as shown.

On the basis of the above, it was concluded that the MM equivalent widths are probably satisfactory, and the remaining analysis was done using their values. The complete list of equivalent widths for the 116 lines is given in table 7.

III. THE gf-VALUES

One of the biggest problems in abundance studies is to obtain reliable gf-values, where f is the oscillator strength of the transition of interest and g is the statistical weight of the lower level for the transition.

Historically, a variety of experimental techniques have been used to derive gf-values. A discussion of commonly used procedures may be found in Chapter 7 of Aller (1963). Unfortunately, most sets of experimental gf-values are characterized by rather large random errors and, in many cases, systematic errors. The effect of random errors can be reduced by using a large number of lines in the abundance analysis, as was done by MM (1964). Systematic errors in the calibration of experimental apparatus are more difficult to detect and are the subject of much concern in abundance studies.

Part of our problem with chromium is that published lists of gf-values are somewhat limited. Only two, those of CB (1962) and of Hill and King (1951), contain values for all the lines to be used in the present study. The CB gf-values include a large number of lines of seventy elements and have been used extensively in abundance studies. In the last ten years significant systematic errors have been found for a number of elements in the CB compilation as a result of improved laboratory measurements (see Cocke, Stark, and Evans 1973).

For some time, a number of people have questioned the validity of the normalization function used in the CB study. The normalization function was introduced because experimental gf-values for lines of very low and very high upper excitation potential (χ_u) were larger than predicted theoretically from the Thomas-Kuhn f-sum rule (see the Introduction to Corliss and Bozman 1962 and Chapter 4 in Aller 1963). The normalization function is flat over most

of the range of χ_u . Its principle effect is a decrease in the experimental gf-values for which χ_u is greater than approximately 6.0 eV.

Warner (1964a, 1964b) found that abundances computed for a number of iron-group elements using the CB gf-values had a dependence on χ_u which was similar in shape to the CB normalization function. Pagel (1965) speculated that the observed dependence on χ_u for the iron-group elements could be due to non-LTE overpopulation of states of high χ_u in both the laboratory arc and the solar photosphere. Huber and Tobey (1968) measured Fe I and Cr I gf-values with an absorption shock-tube and did not observe the dependence on χ_u that exists in the CB (1962) and Corliss and Warner (1966) data. In addition, their absolute gf-values for Cr I were about 0.64 dex smaller than the CB values. Similar results were obtained by Wolnik, Berthel, Larson, Carnevale and Wares (1968) and Wolnik, Berthel, Carnevale, and Wares (1969), who measured gf-values for Cr I and Cr II using an emission shock-tube.

The accumulation of measurements by a variety of techniques has strengthened the argument that the CB normalization function should be removed and that errors also exist in the magnitude of the gf-values. Bridges and Wiese (1970) found that Fe I gf-values measured by shock-tube absorption, emission in wall-stabilized arcs, and lifetime measurements were in good agreement. For a general review of lifetime measurements and absolute gf-values obtained by beam-foil spectroscopy, see Wiese (1970).

Withbroe (1969) has suggested that the dependence on χ_u in the CB work may be due to an underestimate of 250-500°K in the CB arc temperature. Bell and Upson (1971) give evidence that much of the effect may be caused by an error in the calibration of the intensity scale of the CB photographic plates.

The present study makes use of the CSE beam-foil measurements (hereafter referred to as the BF gf-values). They determined the absolute gf-values for

44 Cr I lines from measured branching ratios and from lifetime measurements by Cocke, Curnutte, and Brand (1971) using the beam-foil technique. They found that the branching ratios for strong transitions are in general agreement with those of CB, but the absolute gf-values are smaller by about 0.7 dex. This is in general agreement with other studies cited above. The CB gf-values may then be corrected for the zero-point error by reducing them uniformly by 0.7 dex.

It is important to know of any χ_u -dependence in the gf-values. In some cases it can have an appreciable effect on the computed abundance. Evans and Schroeder (1972) discuss the effect of an excitation dependent error on the curve of growth. This will be discussed further in Section VI.

The BF gf-values do not appear to have a χ_u -dependence and will be used as a standard for comparison. Figure 4 shows the difference between the CB $\log(gf)$ and the BF $\log(gf)$ as a function of χ_u . The solid line is the linear least squares fit to the data points. The dashed lines represent a deviation of a factor of two either side of the solid line. The CB gf-values used here have not had the normalization function removed. If the BF gf-values have no χ_u -dependence, then the χ_u -dependence of the CB gf-values is 0.11 dex/eV, as shown in figure 4.

This analysis was repeated with the normalization function removed from the CB gf-values. The normalization function drops off rather sharply above $\chi_u = 5.9$ eV and can be approximated closely by using several linear segments of different slope. The corrections are:

for $\chi_u = 5.9$ to 6.5 eV,

$$[\log(gf)_{CB}]_{\text{corrected}} = \log(gf)_{CB} + 0.333(\chi_u - 5.9),$$

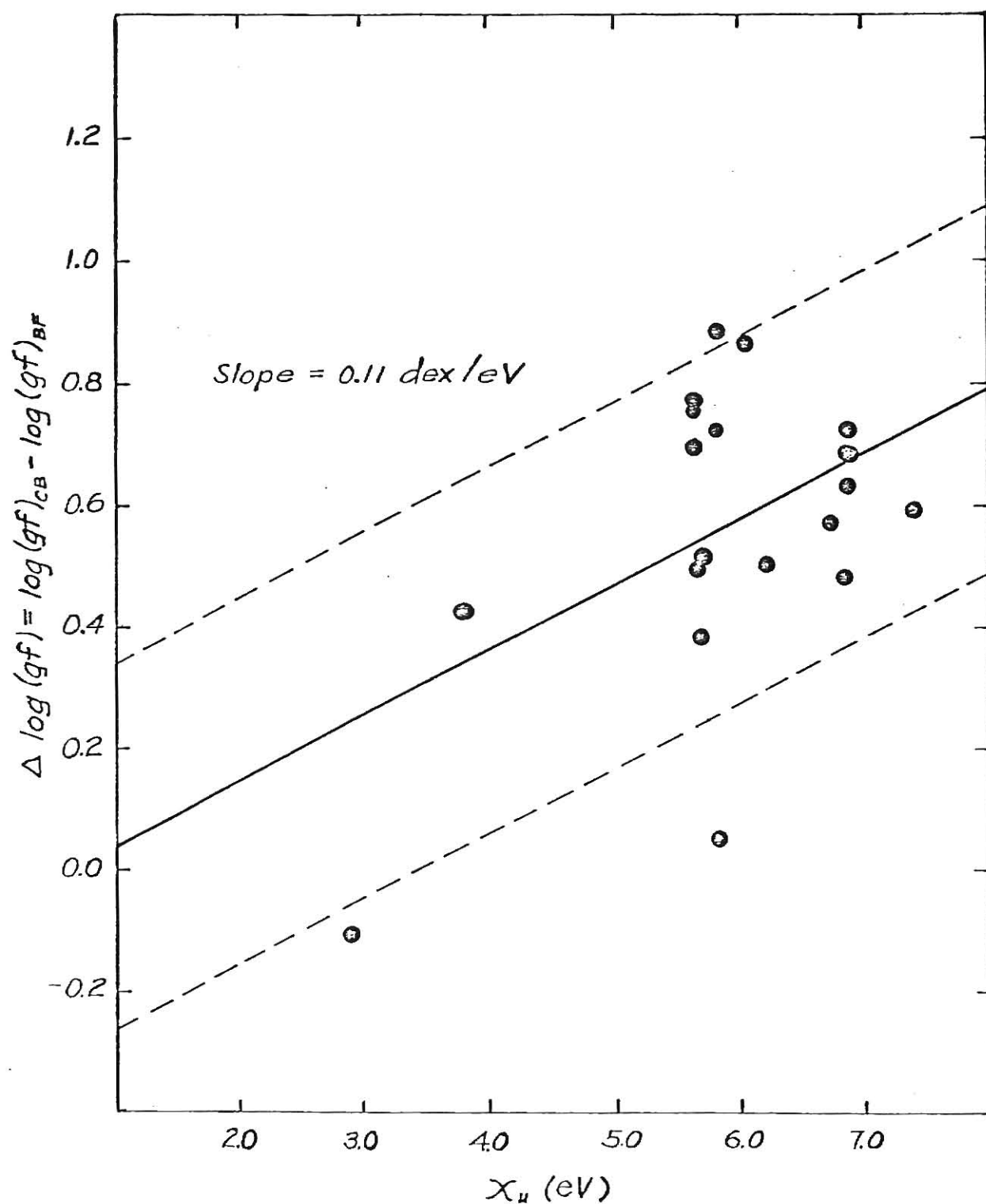


Fig. 4.—A comparison of CB Cr I gf-values with the BF gf-values plotted against upper energy level. The solid line is the least squares fit to the data, and the dashed lines represent a deviation of a factor of two from the solid line.

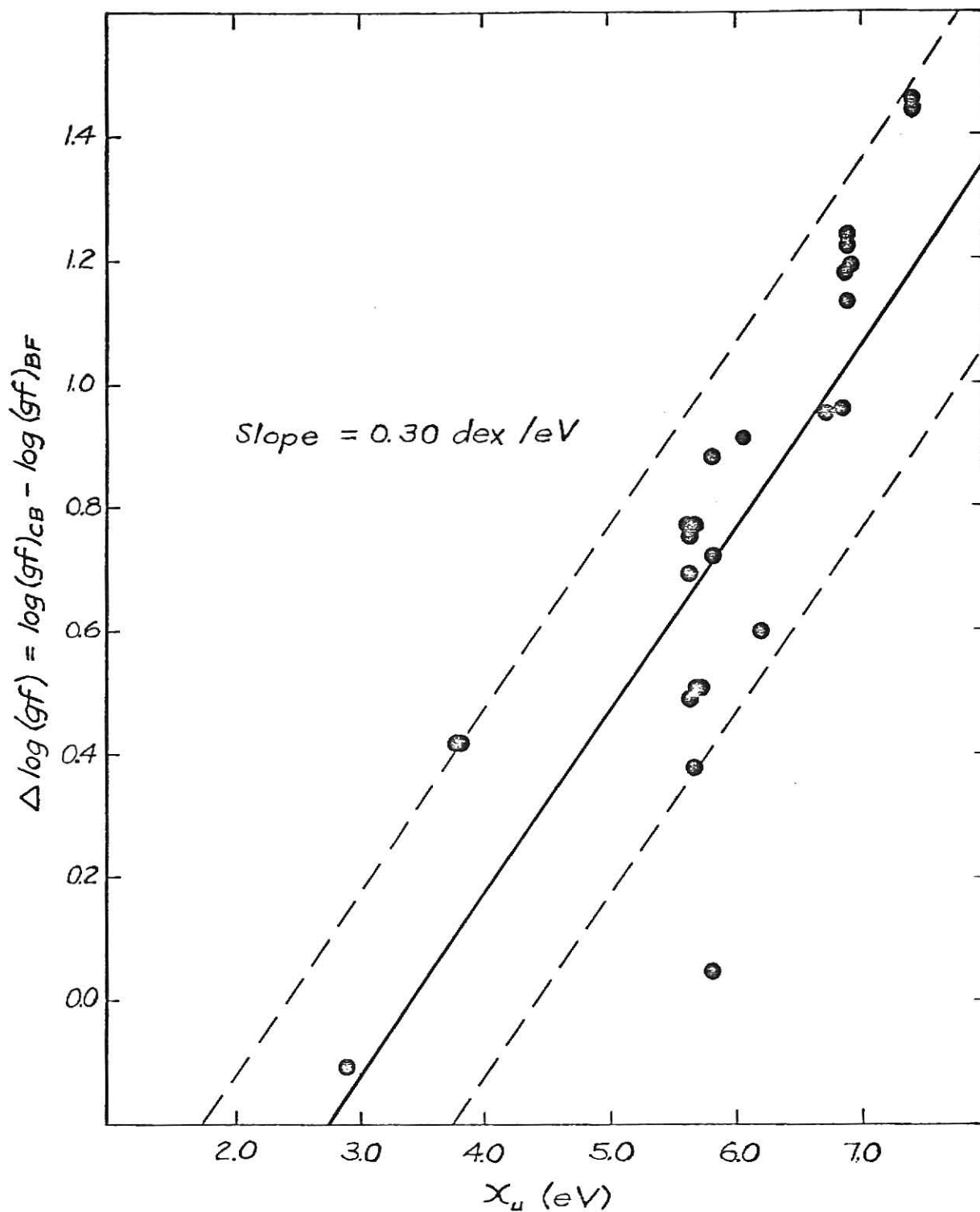


Fig. 5.— The same as figure 4 except that the normalization function has been removed from the CB data.

for $\chi_u = 6.5$ to 7.0 eV,

$$[\log(gf)_{CB}]_{\text{corrected}} = \log(gf)_{CB} + 0.600(\chi_u - 6.5) + 0.2,$$

and for $\chi_u > 7.0$ eV,

$$[\log(gf)_{CB}]_{\text{corrected}} = \log(gf)_{CB} + 0.850(\chi_u + 7.0) + 0.5.$$

Figure 5 shows the effect on figure 4 of removing the normalization function. It can be seen that the gf-values of only a few lines have been changed, but that the slope has increased from 0.11 dex/eV to 0.30 dex/eV.

Besides CB, the other large source of Cr I gf-values is that of Hill and King (1951), mentioned earlier. Making use of the CB data, we checked the Hill and King gf-values for possible χ_u -dependence. Figure 6 shows the difference between the uncorrected CB $\log(gf)$ and the Hill and King $\log(gf)$ as a function of χ_u . Again the solid line is the least squares fit and the dashed lines are factors of two on either side. Since the slope is negative, the Hill and King data has a stronger positive χ_u -dependence than does the CB data. The slope is -0.19 dex/eV. However, figures 4 and 5 show that the effect of removing the normalization function is to increase the slope of the CB χ_u -dependence by about 0.19 dex/eV. Consequently, the Hill and King data and the corrected CB data have about the same dependence on excitation potential.

We conclude that there is no apparent advantage of using the Hill and King gf-values and will use the corrected CB gf-values in the present study.

The apparent excitation dependence of the CB gf-values derived from the BF gf-values alone (figures 4 and 5) is based on a relatively small number of lines. It is desirable to use a more extensive set of recent laboratory measurements to validate the existence of the χ_u -dependence in the CB gf-values.

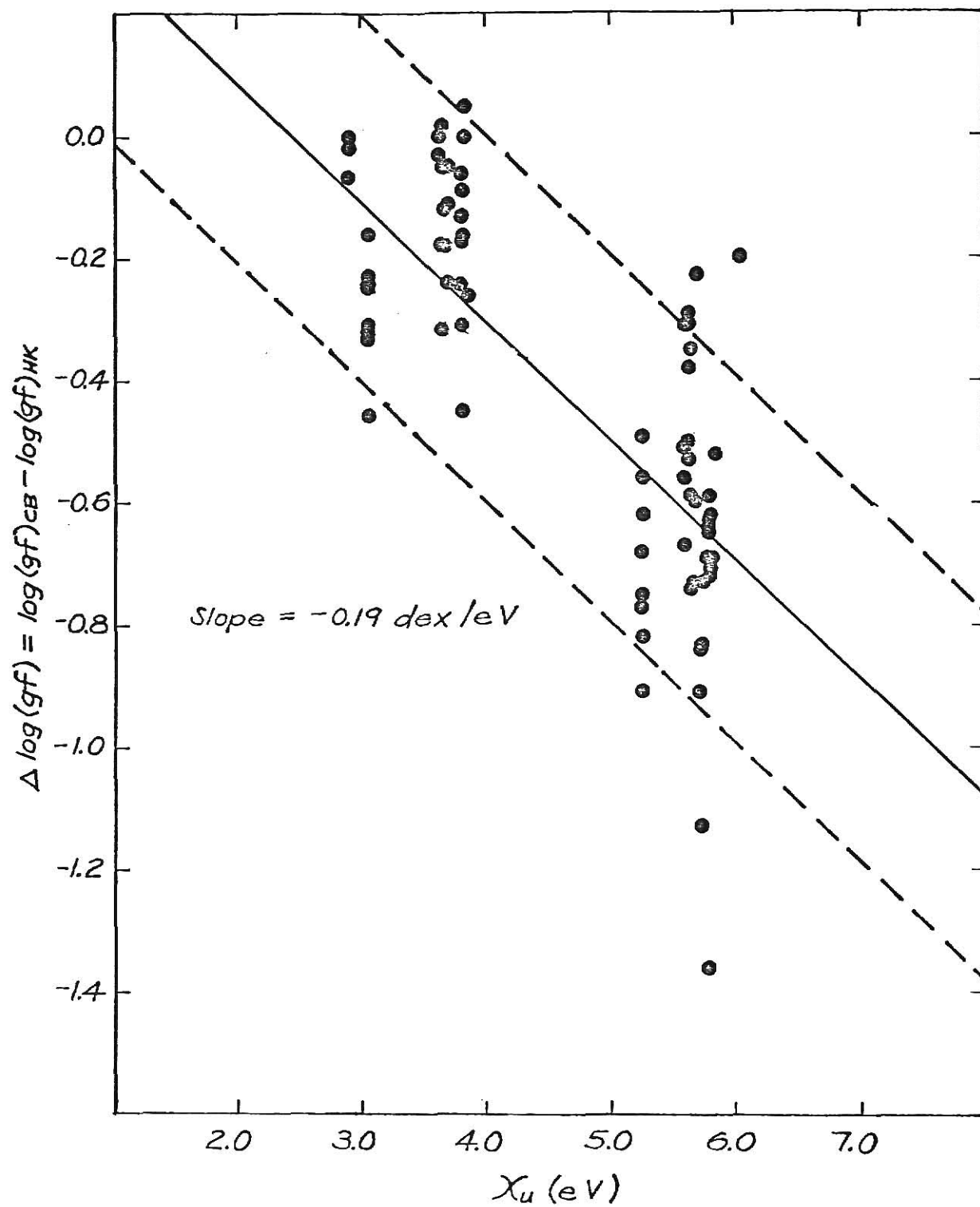


Fig. 6.— A comparison of the CB gf-values with the Hill and King gf-values. Here, the normalization has not been removed from the CB data.

The most extensive lists of recent gf-value measurements come from shock-tube experiments. Shock tube measurements have an advantage over arc measurements because the state of the gas is more homogeneous. The temperature can be determined rather accurately and LTE conditions have been found to prevail (see Byard 1968 and Wolnik, et. al. 1969 for detailed discussions of shock-tube measurements). Three sets of shock-tube gf-values were added to the BF gf-values to test for an excitation potential dependence. These studies are those of Huber and Tobey (1968), Byard (1968), and Wolnik, et.al. (1969).

Figure 7 shows a possible χ_u -dependence in the uncorrected CB data on the basis of the combined set of gf-values. The slope is 0.076 dex/eV, which is slightly less than that obtained with the BF data alone. Figure 8 shows the same plot with the CB normalization function removed. The slope has increased to 0.21 dex/eV, which is about 0.1 dex/eV less than with the BF data alone. The data used in figure 7 is nearly identical to that in figure 3 of Cocke, Curnutte, and Brand (1971). In their paper, they state that they do not believe a significant excitation dependence exists in the CB data. However, if indeed the normalization function should be removed, figure 8 strongly suggests an excitation dependent error in the CB data of about the same magnitude as found by Evans and Schroeder (1972) for Fe I. Figure 8 also agrees well with the separate results of Byard (1968) and Wolnik, et.al. (1969) for Cr I. The slope in figure 8 is within 0.03 dex/eV of the slope in figure 3 of Wolnik, et.al., who used only shock-tube gf-values and removed the CB normalization function.

In figure 9 the $\Delta \log(gf)$ -values are replotted as a function of wavelength. In this figure, the slope is $-0.35 \text{ dex}/1000\text{\AA}$. This result also agrees closely with Wolnik, et.al. (1969).

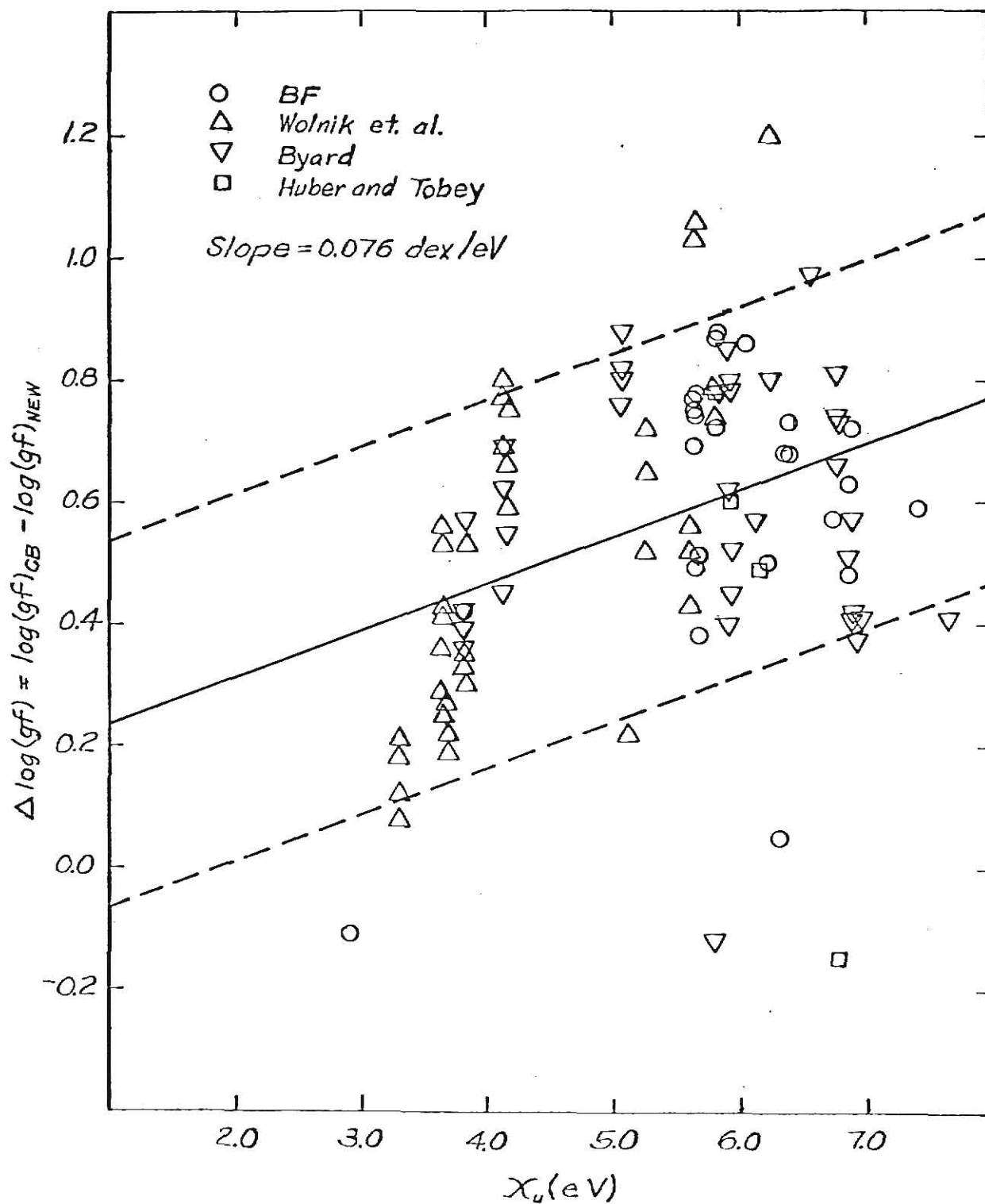


Fig. 7.—A comparison of CB gf-values with several other laboratory measurements as indicated. The BF data is the same as that of figure 4. The added data points are all shock-tube measurements.

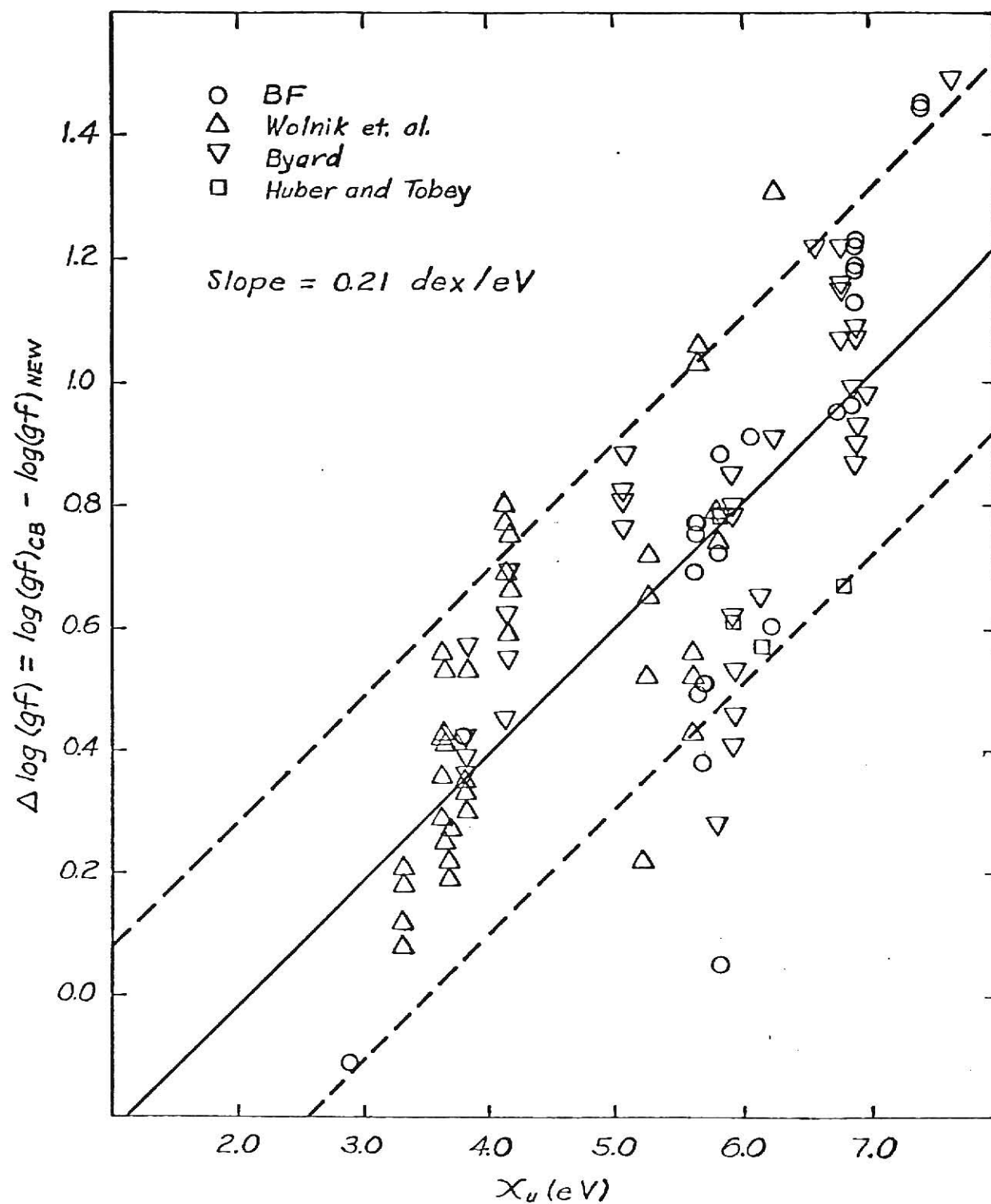


Fig. 8.—The same plot as figure 7 except that the normalization function has been removed from the CB data.

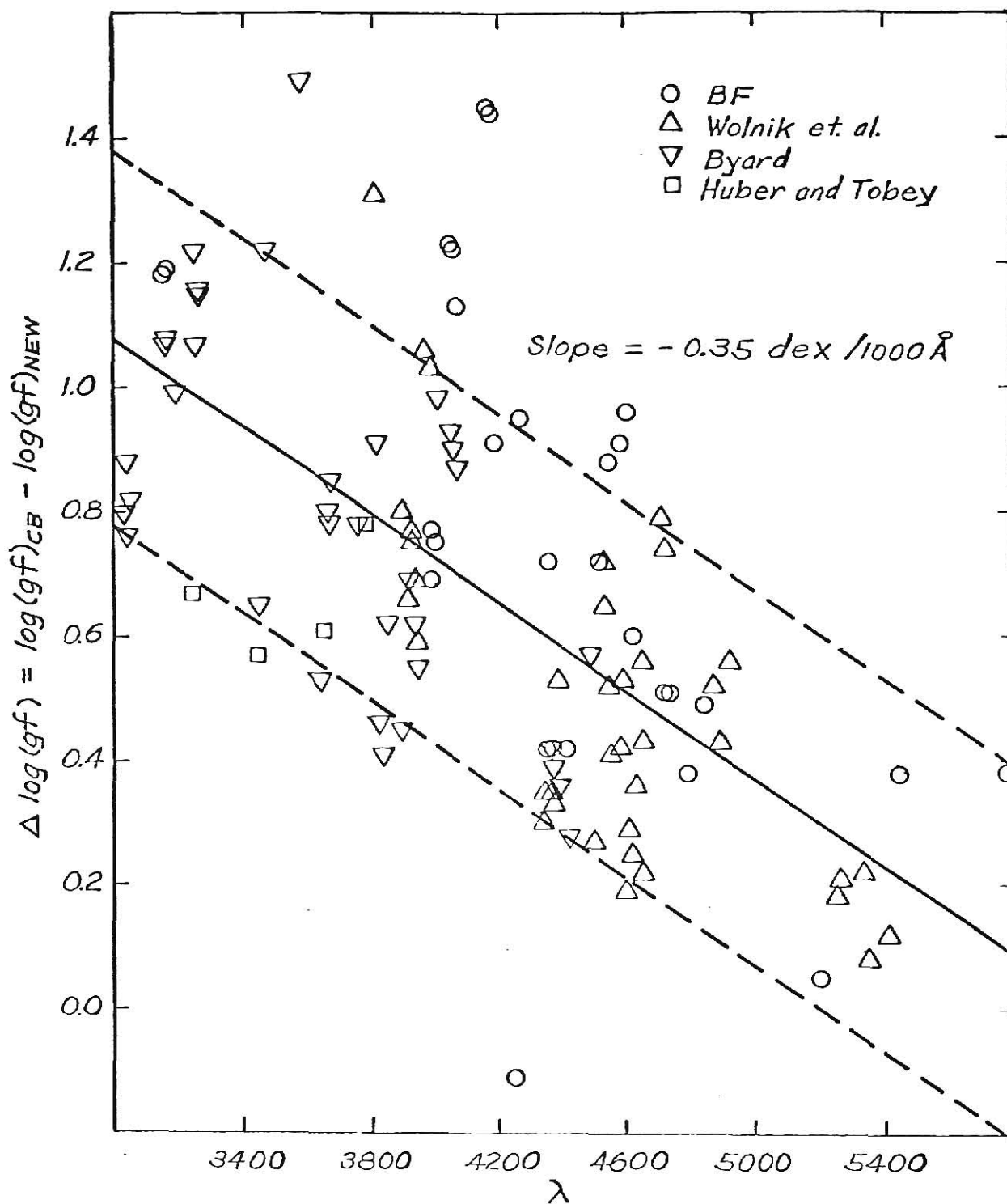


Fig. 9.—The gf-value differences of figure 8 plotted against wavelength to show an apparent wavelength dependence in the CB data.

Table 2 is a partial list of $\log(gf)$ -values used in this study. The first two columns give the revised multiplet number and wavelength of the line as given by Moore (1945). Columns three and four contain the BF $\log(gf)$ -values of Cocke, Curnutte, and Brand (1971) and CSE (1973), respectively. The fifth column is the originally published CB $\log(gf)$ -values, whereas column six contains those CB values which are changed by removal of the normalization function. The last two columns are the data of Byard (1968), and Wolnik, et.al. (1969). It should be pointed out that the Byard and Wolnik $\log(gf)$ -values in table 2 are not the complete set used in figures 7 through 9, but only those common to the BF lists.

We now address the problem of correcting the CB data. It is possible to substitute directly the BF and shock-tube gf -values for the CB gf -values. However, since the relative χ_u -dependence differs among the different sets of gf -values, some correction between data sets should be made. As an example, Foy (1972) used several different sets of gf -values in a curve of growth abundance calculation for iron. He selected one set as a standard set and corrected the χ_u -dependence and zero-point of each of the remaining sets to agree with the standard set.

It is not clear that such a procedure is possible for the large number of chromium lines which we require. There are not enough BF and shock-tube values to substitute for all, or even most, of the CB data set. Also, since we desire to examine the magnitude of the influence of systematic errors, it would be instructive to carry the excitation dependent error in the CB values further through the analysis.

Therefore, we will do the abundance calculations using the CB gf -values corrected only by removing the normalization function. The computed line abundances can be corrected for the zero-point shift found by CSE (1973), and

TABLE 2
Comparison of $\log(gf)$ -Value Measurements

$\log(gf)$						
RMT No.	Wavelength	Beam-Foil (1971)	Beam-Foil (1973)	Corliss & Bozman	Corliss & Bozman*	Wolnik, et.al.
1	4254.35	-0.16		-0.27		
22	4351.05	-1.49		-1.07		
	4412.25	-2.48		-2.06		
	4373.25	-2.21		-1.79		
38	3963.69	0.56		1.34		0.28
	3969.75	0.52	0.52	1.25		
	3976.67	0.50	0.47	1.24		0.23
	3983.91		0.35	1.04		0.18 [†]
	3969.06	-0.60	-0.64	0.13		
	3984.34	-0.42	-0.44	0.33		0.18 [†]
	3991.67	-0.51		0.24		
	3976.01		-2.21			
42	3767.43		-1.48	-0.47		
104	4374.16		-0.49	0.38		
	4346.83	-0.52		0.20		
115	3163.76	-0.18	0.072	0.72	1.23	0.15
	3155.15	-0.18	0.021	0.72	1.22	0.15
	3148.45	-0.23	-0.018	0.64	1.14	
	3160.61		-1.20			
144	4836.86	-1.26	-1.07	-0.53		
	4814.27		-1.21			
	4810.73		-1.30			
	4847.18		-1.85			
	4825.51		-1.96			
145	4737.35	-0.03		0.48		
	4730.71	-0.18		0.39		
	4724.42	-0.49		0.02		
150	4540.72	-0.059		0.78		
	4511.90	-0.35		0.37		
167	4880.06		-1.60			
	4874.65		-1.68			
168	4792.51	-0.07		0.31		
173	4569.53		-1.04			
179	4179.26	-0.21		0.71	0.76	

[†] $\log(gf)$ for unresolved blend of 3883.91 and 3984.34

* gf -values which are changed after removal of normalization function

TABLE 2 (Cont'd)

RMT No.	Wavelength	Beam-Foil (1971)	Beam-Foil (1973)	Corliss & Bozman	Corliss & Bozman*	Byard	Wolnik, et.al.
196	4575.12	-0.93		-0.07	-0.02		
204	5442.41	-0.80		-0.42			
207	5166.23		-1.74				
	5196.44	-1.09	-0.28	-0.24			
209	4626.80		-1.85				
227	5783.15	-0.42		-0.04			
233	4622.49	0.07		0.57	0.67		
247	4263.14	0.33		0.90	1.28		
251	4039.10		0.40	1.13	1.64	0.73	
	4048.78		0.30	1.04	1.54	0.64	
	4058.77		0.28	0.93	1.43	0.56	
	4057.81		-1.70				
	4039.30		-0.80				
	4049.78		-0.80				
286	4595.59	0.39		0.86	1.34		
305	4161.42	0.36		0.95	1.81		
	4165.52	0.29		0.88	1.73		

these abundances then analyzed for a χ_u -dependence. Since a gf-value that is too large would produce an abundance that is too small, the resulting χ_u -dependence would be expected to be the negative of that in figure 8.

IV. THE MODEL ATMOSPHERE

a) Computation of the Model Atmosphere

To compute a theoretical line profile, the emergent monochromatic continuum intensity as a function of limb distance and the monochromatic continuum absorption coefficient as a function of depth must be known, as well as several quantities peculiar to the particular line. This information was obtained from a model solar atmosphere.

The calculation of the model was done with a digital computer code developed by Professor J. C. Evans at Kansas State University, which is a modification of a code developed by Professor G. Elste at the University of Michigan. A brief discussion of the computational procedure will be given here. For additional information, the reader should refer to the theses by Dreiling (1970), Nichols (1970), and Wenstrand (1972).

The calculation is carried out using rather standard simplifying assumptions. These are: (i) the atmosphere may be approximated by a semi-infinite plane-parallel plasma; (ii) the atmosphere is in a steady-state and in hydrostatic equilibrium; (iii) the atmosphere may be approximated by a finite number of layers (27 in this code); and (iv) each layer is homogeneous and in a state of local thermodynamic equilibrium (LTE). Discussions of the validity of these assumptions and where they are used may be found in most textbooks on stellar atmospheres (e.g. Aller 1963 and Mihalas 1970).

The parameters of the computation are the temperature distribution, the logarithm of the effective surface gravity, and the chemical composition. In this code, we used a 15 element composition which accounts for the major contributors to the ionization equilibrium and the dominant opacity sources in the sun. The computation of the ionization equilibrium and the monochromatic

continuum absorption coefficient was done assuming three ionization stages: neutral, singly ionized, and doubly ionized.

The computation requires an initial estimate of the electron pressure for each layer, with which first estimates of the ionization equilibrium and the continuum absorption coefficient are computed for each layer. These two quantities are used to solve the hydrostatic equation for the gas pressure distribution. With the gas pressure and ionization equilibrium, a new estimate is made of the run of the electron pressure with depth. The code continues to iterate on electron pressure until the gas and electron pressures converge. The convergence is quite rapid and numerically stable. Physically, this is due to the fact that the negative ion of hydrogen is the dominant opacity source, and that most of the hydrogen is neutral.

Figure 10 shows the temperature distributions for five solar model atmospheres. The Athay Solar Model 10 (Athay 1967) is a theoretical model. The four other models are semi-empirical, based in part on solar observational data. They are the Harvard Smithsonian Reference Atmosphere (HSRA) (Gingerich, Noyes, Kalkofen, and Cuny 1971), the Holweger Solar Model (Holweger 1967), the Elste Solar Model (Elste 1970), and the Bilderberg Continuum Model (Gingerich and de Jager 1968). It is evident from figure 10 that the greatest deviations among these five temperature distributions occur at very large and very small values of the continuum optical depth at 5000 \AA (τ_0), which is used as a depth scale. The temperature models agree closely in the vicinity of $\log \tau_0 = 0$, where most line formation occurs. Consequently, it would be expected that the calculated line abundances are not strongly dependent on which particular model atmosphere is used.

To check that this is indeed the case, the abundance calculations were done separately with three of the five model atmospheres: the Elste Solar

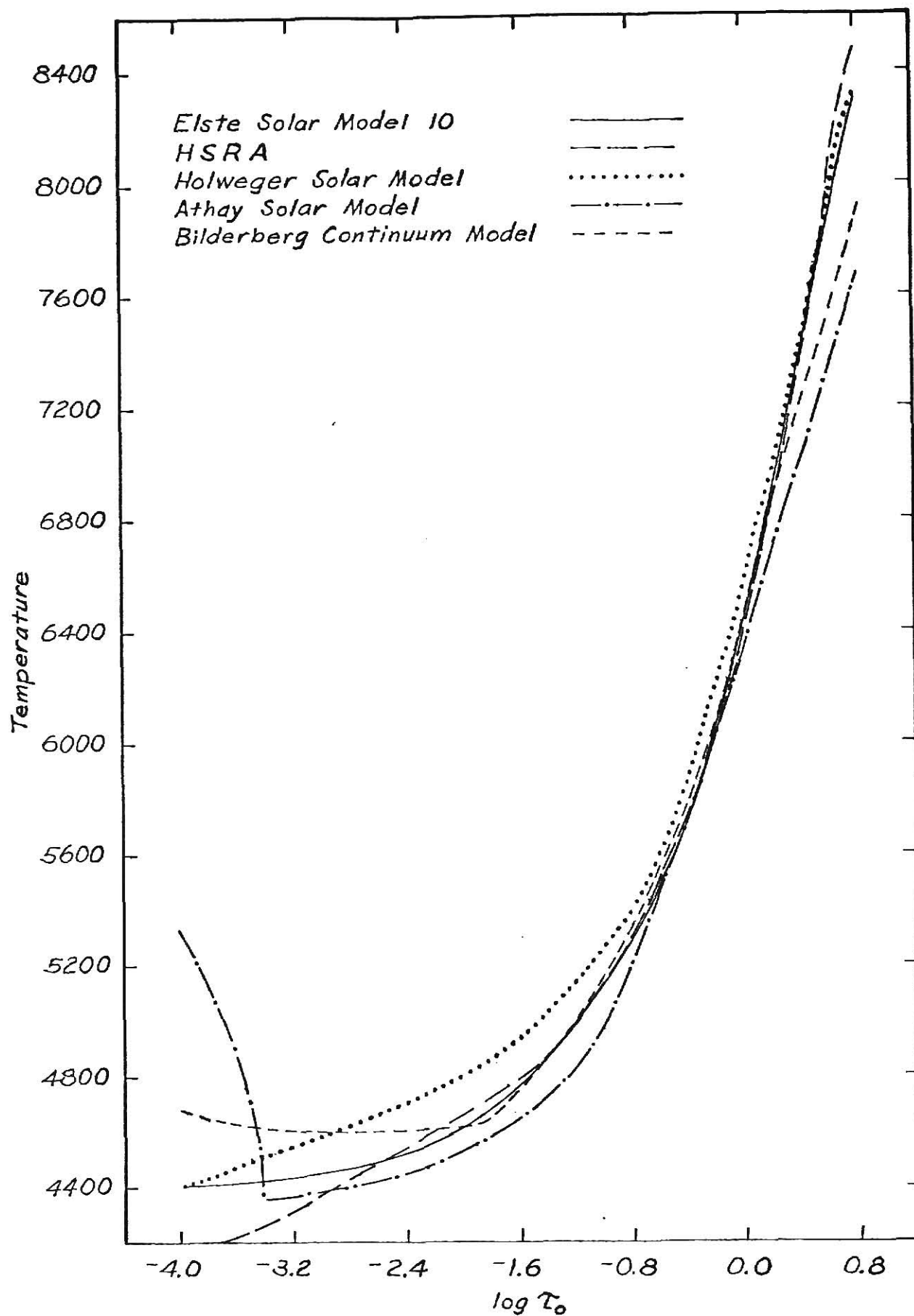


Fig. 10.— A graph of temperature versus the logarithm of the continuum optical depth at 5000 Å (a reference depth scale) is shown for the five solar models indicated.

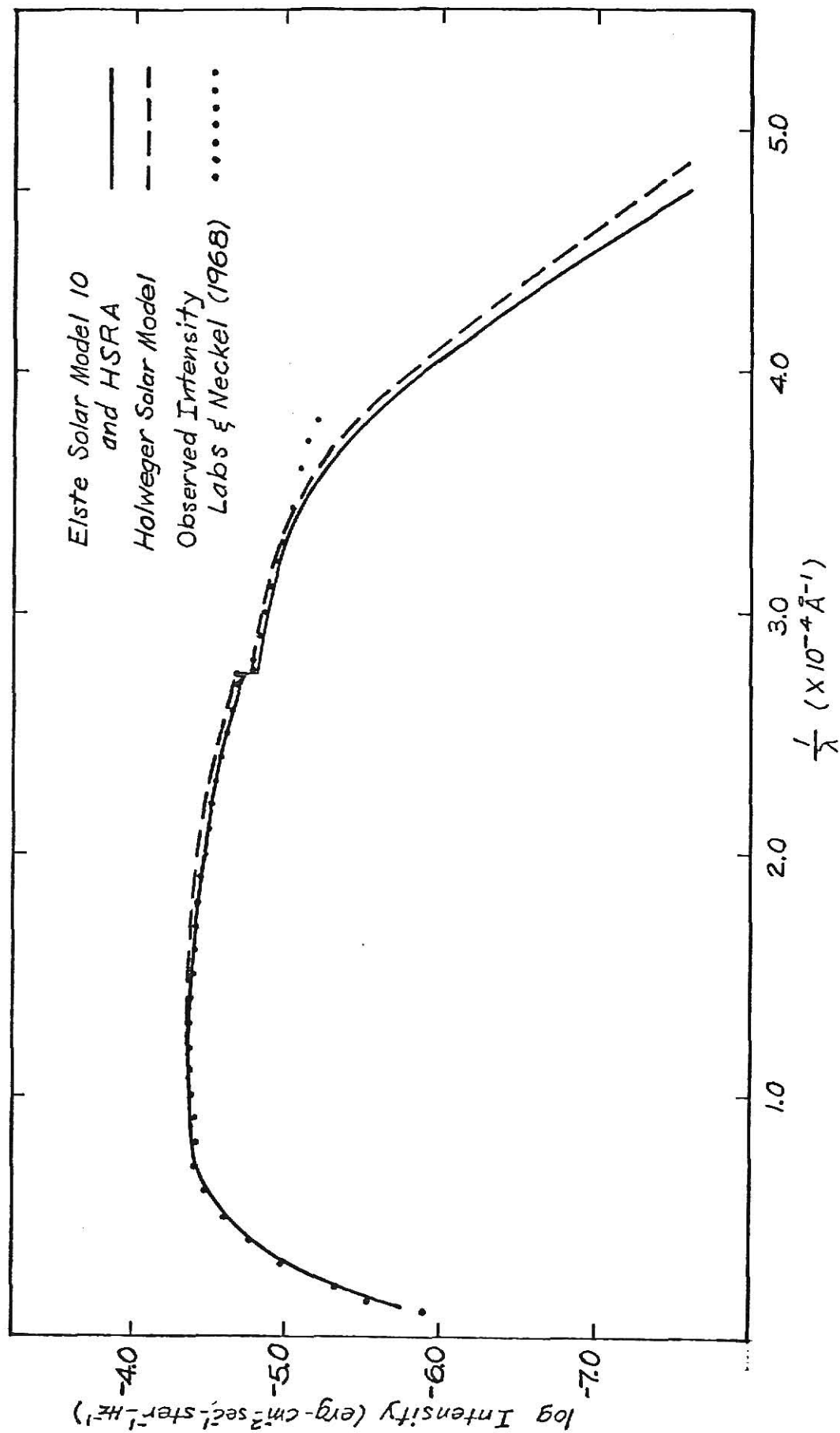


Fig. 11.— The plot of the logarithm of emergent monochromatic continuum intensity against $\frac{1}{\lambda}$ for the three thermal models indicated and the observational data of Labs & Neckel (1968). The Elste Solar Model 10 and the HSRA model are indistinguishable on this scale.

Model 10, the HSRA, and the Holweger Solar Model. A plot of the emergent monochromatic continuum intensity is shown in figure 11 on a $1/\lambda$ scale for these three model atmospheres. The use of a $1/\lambda$ scale for the abscissa is convenient, since it is proportional to energy. On the scale of figure 11, the Elste Solar Model 10 and the HSRA are identical and are represented by the solid line. The Holweger model is the dashed line. The points represent the observational data of Labs and Neckel (1968). All three models agree well with the observed intensities at wavelengths longer than about 3000 \AA ($1/\lambda = 3.3 \times 10^{-4} \text{ \AA}^{-1}$). The fit is poor below 3000 \AA , but this will not affect the abundance calculations since all the lines to be used have wavelengths greater than 3900 \AA ($\frac{1}{\lambda} = 2.6 \times 10^{-4} \text{ \AA}^{-1}$).

b) The Microturbulence Model

Photospheric and chromospheric velocity fields are important phenomena which influence the line formation in stellar atmospheres. Although mass motions are of apparently greater importance in giant and supergiant stars, they have significant effects in the solar atmosphere and should be included in the line calculations.

Two kinds of mass motion are generally considered in model atmosphere and line profile calculations (Ramsey 1973). One is called microturbulence, the other macroturbulence. The distinction between these and the effects they produce will be discussed in the following section on line calculations. Only microturbulence is important in abundance calculations since it can increase the line equivalent width.

Gray and Evans (1973) give a general discussion of current research on microturbulence and related phenomena. Athay (1972) presents a detailed discussion of microturbulence in the sun. Recent studies referenced in these

two papers suggest that the distinction between microturbulence and macro-turbulence may not be as clear as was once thought, and the current trend is to consider more generalized velocity fields (e.g. Edmonds and Webb 1972). However, classical microturbulence is probably adequate for the curve of growth calculations of this study.

The microturbulence model consists of a microturbulent velocity for each layer in the model atmosphere. To account for the observed center-to-limb widening of solar lines, the velocity may be split into two components, one along the solar radius (radial component) and the other perpendicular to it (tangential component).

A wide variety of solar microturbulence models has been used. Some are homogeneous, having no depth gradient (i.e. depth-independent). Others have positive or negative gradients for the radial component. Some models are anisotropic, having radial and tangential components of different magnitude.

Figure 12 shows five different microturbulence models which were used in this study. In the Schmalberger (1963) and Holweger (1967) models, both the radial and tangential velocities increase with depth, whereas they decrease with depth in the outer layers of the de Jager and Neven (1972) model. The Athay and Canfield (1969) model is depth-independent except in the outermost layers. Only the de Jager-Neven model is isotropic (no center-to-limb dependence). The final model is our own, which is depth-independent and has a larger tangential than radial component.

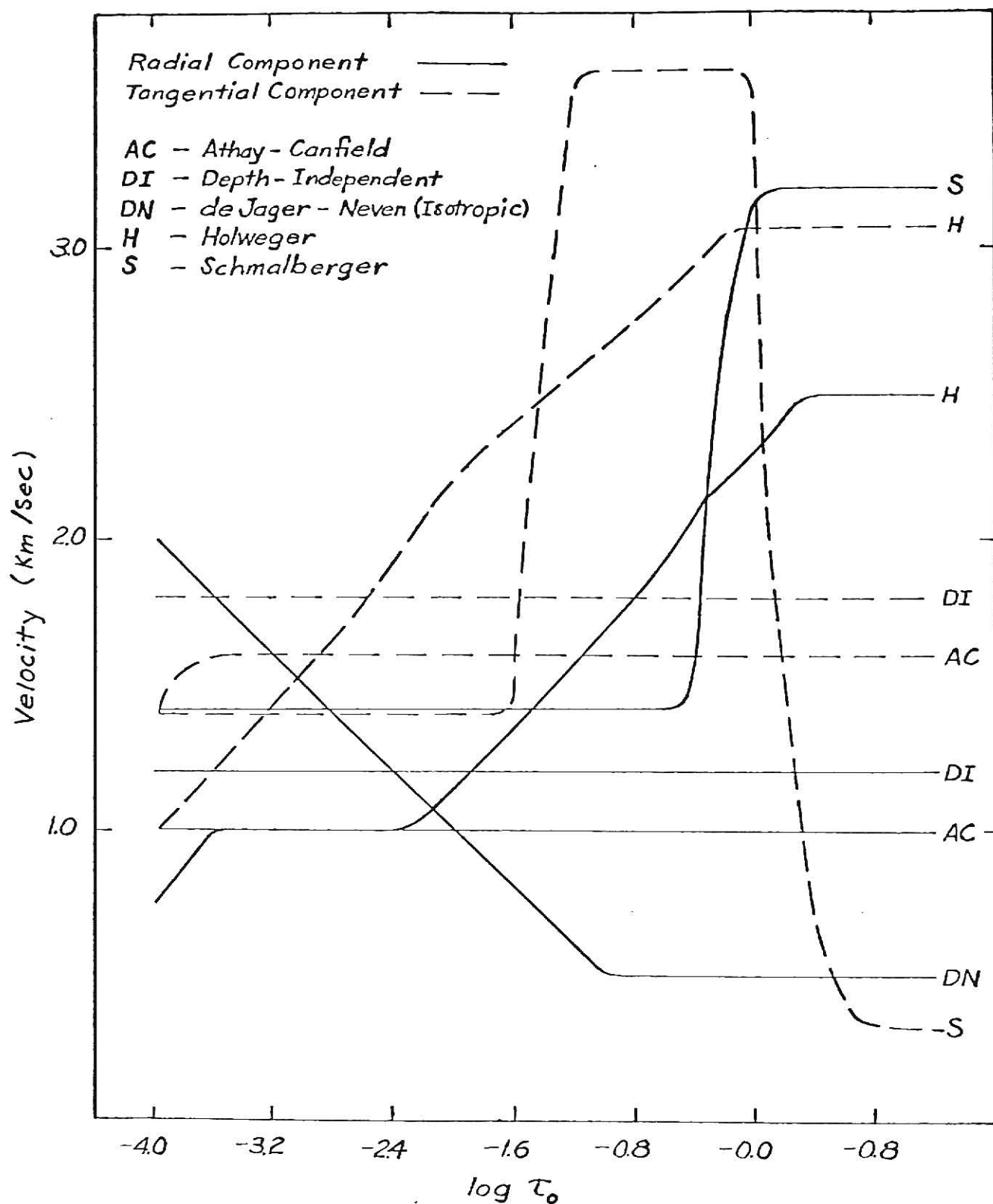


Fig. 12.—A comparison of five different microturbulence models plotted against $\log \tau_0$. Note that the radial and tangential components of the microturbulence are different in all models except the de Jager-Neven model.

V. THE LINE CALCULATIONS

a) Line Depth

The line calculation is a step leading up to the calculation of a theoretical curve of growth which follows the basic procedure of Aller, Elste, and Jugaku (1957). Details of their curve of growth procedure may be found in Aller (1960) and in Chapter 8 of Aller (1963). The theoretical curve of growth will be discussed at the end of this section.

The monochromatic line depth at a limb position μ is defined as

$$r(\mu) = \frac{I_{\lambda}^c - I_{\lambda}^l}{I_{\lambda}^c}, \quad (1)$$

where I_{λ}^c is the continuum intensity in the wavelength vicinity of the line and I_{λ}^l is the intensity in the line, both for a given limb distance μ . I_{λ}^c and I_{λ}^l may be obtained from the solutions of the equation of radiative transfer for the continuum and the line radiation, respectively (see Aller 1963, Mihalas 1970, Cowley 1970, and Athay 1972 for a detailed discussion of the radiative transfer problem).

The calculations of line equivalent widths were made using a computer code developed by Professor J. C. Evans. Additional information about this code is given in the theses by Dreiling (1970), Nichols (1970), and Wenstrand (1972). The depth-dependent quantities which are needed in the line calculations are: (i) the 5000 \AA continuum absorption coefficient per hydrogen particle κ_0^c , generated by the atmosphere code; (ii) the monochromatic absorption coefficient per hydrogen particle for the line κ_{λ}^l ; (iii) the monochromatic continuum optical depth τ_{λ}^c , which is also generated by the atmosphere code; and (iv) the line optical depth τ_{λ}^l .

The continuum line optical depth at any wavelength λ is related to the continuum or line optical depth scale at 5000 \AA by

$$\tau_{\lambda} = \int_0^{\tau_0} \frac{\kappa_{\lambda}}{\kappa_0^c} d\tau_0, \quad (2)$$

where

$$\tau_0(z) = \int_0^z \kappa_0^c \rho dz, \quad (3)$$

and κ_{λ} is either the monochromatic continuum or monochromatic line absorption coefficient at the wavelength λ , τ_0 is the continuum optical depth at 5000 \AA , ρ is the mass density, and z is the geometric depth in the radial direction. The form of equation (2) serves to specify the optical depth at any wavelength λ in terms of the reference optical depth τ_0 defined at 5000 \AA in the continuum. Both κ_0^c and τ_0^c are part of the model atmosphere.

b) The Line Absorption Coefficient

The line absorption coefficient per hydrogen particle is given by Aller (1963) as

$$\kappa_{\lambda}^l = (1 - e^{-hc/\lambda kT}) \left(\frac{N}{N_H} \right) \frac{e^2 \sqrt{\pi}}{mc^2} \frac{\lambda^2}{\Delta\lambda_D} fH(a,v), \quad (4)$$

where $(1 - e^{-hc/\lambda kT})$ is the correction for stimulated emission, N is the number density of absorbing particles in the lower level of the transition producing the line, N_H is the number density of hydrogen particles, $\Delta\lambda_D$ is the Doppler width of the line, f is the oscillator strength for the transition, and $H(a,v)$ is the broadening or Voigt function.

Following a procedure contained in Evans (1966), N may be written as

$$N = \left(\frac{n_{p,s} u_2}{n_2} \right) \left(\frac{1}{U} \right) N_i, \quad (5)$$

where $n_{p,s}$ is the number density of particles of chemical species i in the s th excitation state of the p th ionization stage (i.e., the number density in the lower level of the transition of interest), $N_i = n_1 + n_2 + n_3$ is the total number density of particles of species i distributed over the first three ionization stages, u_2 is the partition function of the second ionization stage, and

$$U = u_2 \frac{n_1}{n_2} + 1 + \frac{n_3}{n_2}. \quad (6)$$

We may use the Saha equation to compute the ratios, n_1/n_2 and n_3/n_2 , in equation (6) and a combination of the Saha and Boltzmann equations to compute the ratio, $n_{p,s}/n_2$, in equation (5) in the form

$$\log \left(\frac{n_{p,s} u_2}{n_2} \right) = \log g_{p,s} + \Delta\chi\theta + (p-2)[9.0801 - 2.5 \log \theta - \log Pe], \quad (7)$$

where $g_{p,s}$ is the statistical weight of the lower level,

$$\Delta\chi = \begin{cases} \chi_1 - \chi_{1,s}, & \text{if } p = 1, \\ -\chi_1, & \text{if } p = 2, \\ -\chi_{3,s} - \chi_2, & \text{if } p = 3, \end{cases}$$

χ_1 and χ_2 are the ionization energies in electron volts for singly and doubly ionized particles, $\chi_{1,s}$ and $\chi_{3,s}$ are the excitation potentials of level s in electron volts,

$$\theta = \left(\frac{1}{kT} \right) \frac{1}{\log_e 10} = \frac{5040}{T} ,$$

and P_e is the electron pressure.

The line absorption coefficient per hydrogen particle, equation (4), can now be expressed in the form

$$\begin{aligned} \kappa_{\lambda}^{\ell} = & \epsilon_i \frac{\sqrt{\pi} e^2}{mc^2} \frac{\lambda^2}{\Delta\lambda_D} \frac{g_{p,s}}{U} \\ & \times [10^{\Delta\chi\theta + (p-2)(9.0801 - 2.5 \log \theta - \log P_e)}] \\ & \times [1 - 10^{-\chi_{\lambda}\theta}] fH(a, \nu), \end{aligned} \quad (8)$$

where ϵ_i is the relative abundance $\frac{N_i}{N_H}$. The last factor is the correction for stimulated emission, where χ_{λ} is energy of the stimulating photon in electron volts.

We may use equation (8) and atomic data for the atomic species of interest to compute the line absorption coefficient as a function of wavelength over the line profile and depth in the atmosphere.

c) The Line Optical Depth

Once the line absorption coefficient has been obtained, the line optical depth may be computed from equation (2). It is found that the logarithm of τ_o is approximately proportional to the geometric depth. Consequently, it is convenient to change the variable of integration from τ_o to $x = \log \tau_o$.

Making this substitution in equation (2), we have

$$\tau_{\lambda}^{\ell} = \int_{-\infty}^x \frac{\kappa_{\lambda}^{\ell}}{\kappa_o} \left(\frac{10^x}{\text{Mod}} \right) dx , \quad (9)$$

where $\text{Mod} = \log_{10} e = 0.43429$. The same equation, with the continuum absorption coefficient in place of the line absorption coefficient, is used to calculate the continuum optical depth.

The integrand of equation (9) is evaluated at 27 depths corresponding to the 27 layers of the model atmosphere, which range from $x = -4.0$ to $x = 1.2$ in steps of $\Delta x = 0.2$. For each depth, κ_{λ}^{ℓ} is obtained from equation (8) and κ_0^c is obtained from the model atmosphere.

d) Line Broadening

Spectral lines are broadened by a variety of physical mechanisms. Some affect the equivalent widths of lines while others do not. In Section IV we remarked that macroturbulence and microturbulence produce different effects on line profiles. We shall now discuss these and other broadening mechanisms.

Macroturbulence is a large scale mass motion which involves convective cells having a large linear extent compared to the photon mean free path. Consequently, the entire line formation region is contained within the cell and the photon-particle interactions which form the line are not directly affected. Instead, the entire line profile produced in a cell is Doppler shifted and the observed profile is the superposition of the profiles of all macroturbulence cells which contribute to the radiation incident on the spectrograph (see Ramsey 1973 for a recent study of macroturbulence broadening).

Since the macroturbulence broadening mechanism and the line formation mechanisms are independent of each other, the equivalent width of the line is not changed. Likewise, broadening due to solar rotation does not affect the equivalent width.

Broadening mechanisms which do affect the equivalent width are microscopic in nature. The microscopic broadening mechanisms important to this

study are: (i) thermal broadening due to random motion of the absorbing particles; (ii) microturbulence, (iii) natural broadening or radiation damping; (iv) the quadratic Stark effect; and (v) van der Waals interactions. These mechanisms produce two kinds of line shape: (i) a Gaussian profile called Doppler broadening; and (ii) a Lorentz profile called pressure broadening.

Microturbulence is defined physically as consisting of turbulence cells whose linear extent is less than the photon mean free path. It is assumed that the microturbulence cells have a Maxwellian velocity distribution as do the thermal motions of particles. However, a number of authors have argued that there is little to warrant this assumption and that other velocity distributions should be investigated (e.g. see Cowley 1970). In this study, we shall retain the assumption of a Maxwellian velocity distribution.

The thermal and microturbulence profiles are both Gaussian and the convolution of the two profiles is the Gaussian profile called the Doppler broadening. The 1/3-width or Doppler width of the convolution is given by

$$\Delta\lambda_D = \frac{\lambda}{c} \sqrt{\xi_{\text{therm}}^2 + \xi_{\text{turb}}^2}, \quad (10)$$

where $\xi_{\text{therm}} = \frac{2kT}{m}$ is the most probable thermal speed of the absorbing particles and ξ_{turb} is the most probable speed of the microturbulence cells.

The remaining broadening mechanisms produce a Lorentz line shape and are frequently called pressure broadening. For the lines in this study, they are only of marginal importance. They are: (i) radiation damping, caused by the finite lifetime of the excited state of an atom; (ii) quadratic Stark broadening, caused by the varying electric fields of ions and electrons near the absorbing atoms; (iii) van der Waals broadening, caused by energy shifts from perturbing hydrogen and helium atoms; and (iv) interruption damping due to collisions.

Each effect is characterized by a damping constant. The radiation damping constant is computed from the classical theory of a damped oscillator (Mihalas 1970). The damping constants for the quadratic Stark effect and the van der Waals interactions are computed from the Lindholm-Foley theory (Mihalas 1970). The total damping constant is the sum of the individual damping constants

$$\Gamma = \Gamma_R + \Gamma_S + \Gamma_W , \quad (11)$$

where Γ_R , Γ_S , and Γ_W are the radiation, quadratic Stark, and van der Waals damping constants, respectively.

The half-width of the line profile in units of Doppler widths is given by

$$a(x) = \frac{\Gamma}{4\pi} \frac{\lambda}{\sqrt{\xi_{\text{therm}}^2 + \xi_{\text{turb}}^2}} . \quad (12)$$

The convolution of the Gaussian profile due to Doppler broadening and the Lorentz profile due to pressure broadening produces a Voigt profile or broadening function, which may be written as

$$H(a, v) = \frac{a}{\pi} \int_{-\infty}^{\infty} \frac{e^{-y^2}}{(v-y)^2 + a^2} dy , \quad (13)$$

where λ_0 is the wavelength of line center, ξ is the thermal velocity of an atom absorbing at wavelength $\lambda(1 - \xi/c)^{-1}$ in its own reference frame,

$$v = \frac{\lambda - \lambda_0}{\Delta\lambda_D} ,$$

$$y = \frac{\Delta\lambda}{\Delta\lambda_D} = \frac{\xi}{\xi_0} ,$$

$$\Delta\lambda = \frac{\xi\lambda}{c} ,$$

and

$$\Delta\lambda_D = \frac{\lambda}{c} \sqrt{\xi_{\text{therm}}^2 + \xi_{\text{turb}}^2} = \frac{\lambda}{c} \xi_0 .$$

For further details, the reader should consult Chapter 9 in Mihalas (1970).

e) The Theoretical Equivalent Width

The theoretical equivalent width may be obtained by integration of the expression for the line depth over the line profile. We used the line depth equation in the Planckian gradient form of Gussman (1967), as modified by Evans and Elste (1971). In this form, with an LTE source function, the monochromatic line depth is

$$r(\mu) = \int_{-\infty}^{\infty} D_{\lambda}(x, \mu) E(x, \Delta\lambda, \mu) dx \quad (14)$$

where

$$D_{\lambda}(x, \mu) = \frac{1}{I_{\lambda}^c(\mu)} \left(\frac{dB_{\lambda}}{dx} \right) \exp(-\tau_{\lambda}^c/\mu),$$

$$E(x, \Delta\lambda, \mu) = 1 - \exp(-\tau_{\lambda}^{\ell}/\mu),$$

and where τ_{λ}^{ℓ} and τ_{λ}^c are computed from equation (9). The $\Delta\lambda$ -dependence comes from the variation of the line optical depth over the line profile.

The equivalent width may now be obtained by integrating equation (14) over wavelength. As indicated earlier, we will express the equivalent width in the form of the reduced equivalent width, or

$$\log \left(\frac{W}{\lambda} \right) = \log \left[\frac{1}{\lambda} \int_0^{\infty} r(\mu) d\lambda \right]. \quad (15)$$

f) The Theoretical Curve of Growth

The theoretical curve of growth is formed by plotting the theoretical equivalent width (equation 15) against a quantity which is proportional to the number of absorbing atoms or ions producing the line. The ordinate is obtained by varying the number of absorbing particles, i.e. the quantity ϵ_i in equation (8).

Following Aller, Elste, and Jugaku (1957), the abscissa is defined as the unsaturated or weak-line equivalent width

$$\log(W/\lambda)_{\text{unsaturated}} = \log \epsilon + \log C , \quad (16)$$

where

$$\log C = \log gf\lambda + \log L . \quad (17)$$

The quantity L is given by Dreiling (1970) as

$$L = \log \left[\frac{\sqrt{\pi}}{c} \int_{-\infty}^{\infty} \sqrt{\xi_{\text{therm}}^2 + \xi_{\text{turb}}^2} Z_i g_{\lambda}^{\mu} dx \right] , \quad (18)$$

where Z_i is essentially the variation in the population of the atomic level of interest with depth in the atmosphere, and g_{λ}^{μ} is the intensity weighting function. The reader should refer to Aller (1963) for a discussion of the weighting function.

From equations (16) and (17) it is seen that the abscissa is proportional to Ngf , where N is the number density of the element of interest. A curve of growth shows how the line equivalent width grows as the number density of the atomic species increases, subject to the physical conditions specified by the model atmosphere. Strictly speaking, each spectral line has its own unique curve of growth. In practice, one curve of growth may be used for

many lines. Of the parameters which differ from line to line, the curve of growth is most sensitive to wavelength and the excitation potential of the lower level.

The dependence on wavelength is relatively weak, permitting a wavelength range of several hundred ångströms to be considered at one time. The curve of growth is much more sensitive to excitation potential, as may be seen in figure 13. Here, the curve of growth has been plotted for three different values of lower excitation potential (in eV) at a wavelength of 4600 \AA and $\mu = 1.0$. The difference between the curves is greatest for strong lines, so care must be taken that, in a group of lines used with one theoretical curve of growth, there are no strong lines with excitation potentials greatly different from that used to calculate the theoretical curve. Once a group of lines of similar wavelength and excitation potential have been selected, the theoretical curve of growth is computed for a dummy line with wavelength, gf-value, and lower excitation potential equal to the mean of the group.

The curve of growth shows that, initially, the equivalent width increases linearly with N_{gf} , and this region is known as the linear portion of the curve. The line becomes progressively deeper in the Doppler core along the linear portion. The curve then begins to level off as the number of absorbers increases further to form what is known as the saturation portion. In this region, the line broadens primarily in the Doppler core and shows little change in the central depth. It is here that the curve is particularly sensitive to temperature and microturbulence (see the paper by Gray and Evans (1973) for a discussion of the sensitivity of the curve of growth to various physical effects).

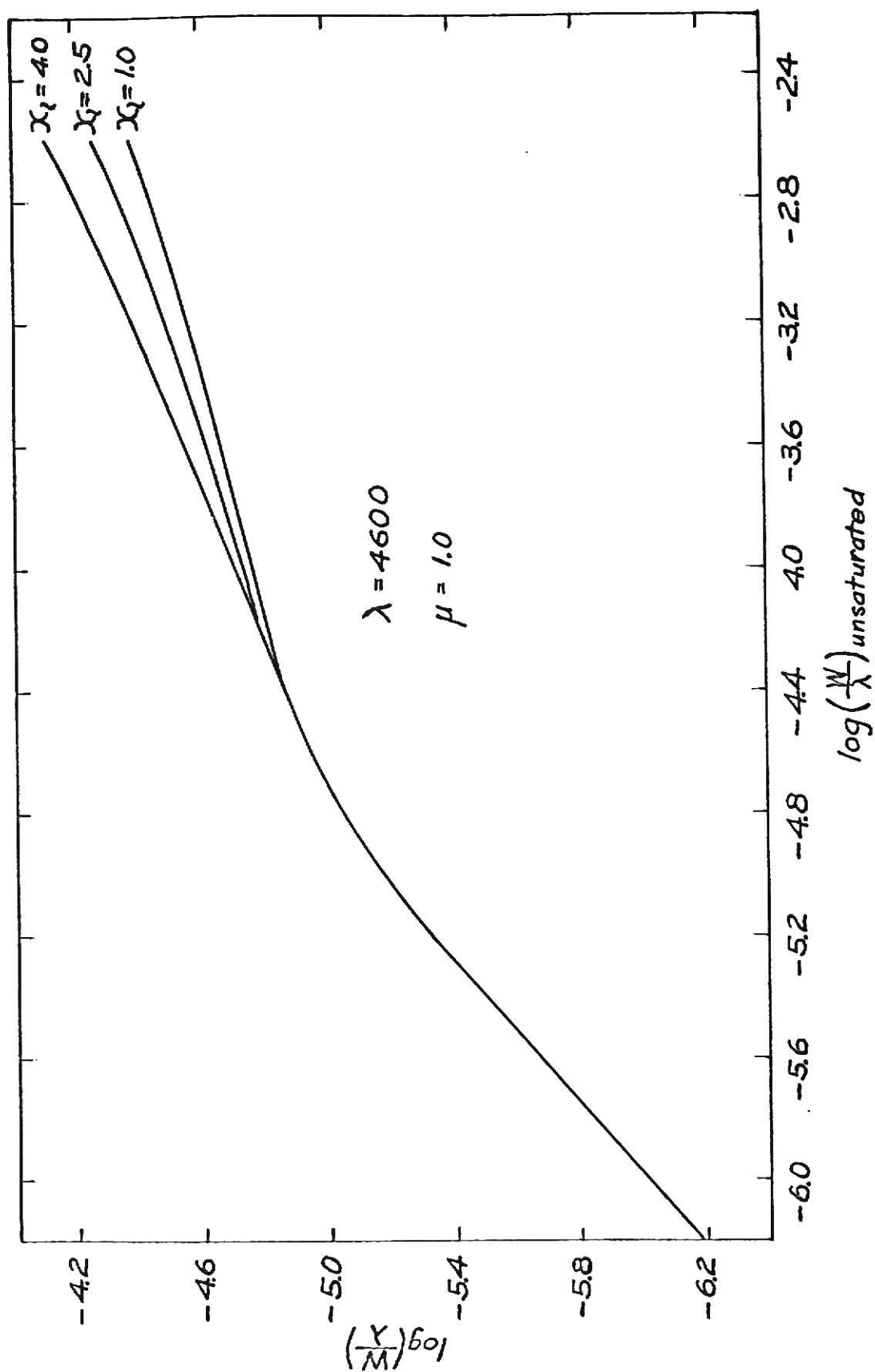


Fig. 13.—A theoretical curve of growth for three different values of lower level excitation potential (in eV) in Cr I.

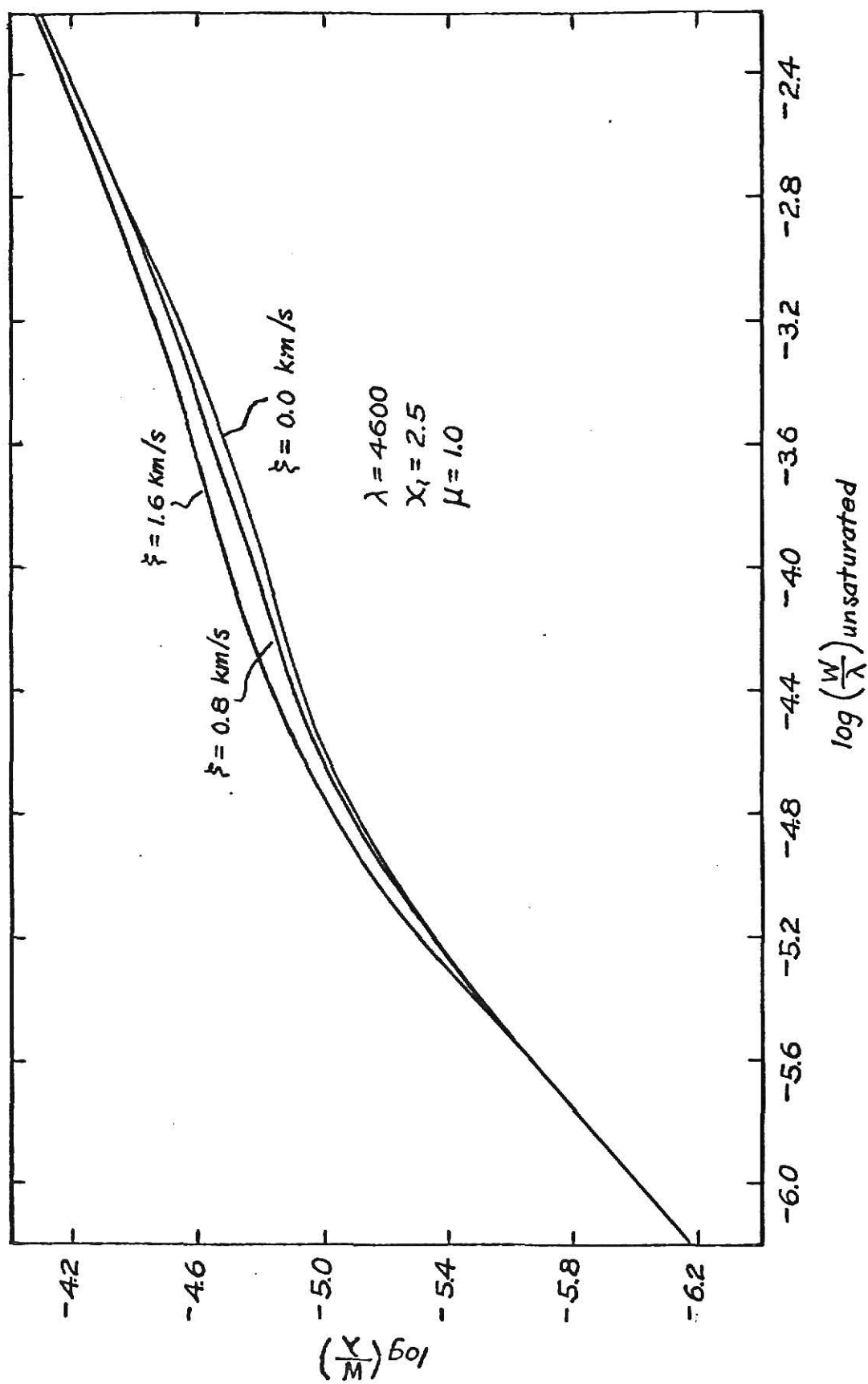


Fig. 14.— The theoretical curve of growth for three different values of microturbulence.

The effect of different values of microturbulence is shown in figure 14. One should note that increasing the microturbulent velocity raises the saturation portion of the curve.

Finally, as N increases still further, the increase in the equivalent width occurs in the damping wings of the line, and the curve begins to turn upwards again. This is known as the damping portion of the curve.

g) The Abundance Calculation

In view of the above considerations, the 116 Cr I lines were arranged in groups having approximately the same wavelength and lower excitation potential (χ_0). This was done such that, in each group, the wavelengths differed by no more than about 300 \AA from the wavelength of the theoretical curve of growth, and no χ_0 differed by more than about one electron volt from that used for the theoretical curve. Furthermore, all lines from the same multiplet were placed in the same group.

Next, an empirical curve of growth was formed for each group. This is done by computing the value of $\log C$ for each line in the group, using equations (17) and (18) and the laboratory gf -value of the line. The empirical curve of growth is constructed by plotting for each line the observed equivalent width $\log(W/\lambda)$, versus $\log C$.

The abundance can then be determined by superimposing the theoretical curve on the empirical so that a best fit to the data points is obtained. The difference between the theoretical and empirical abscissas is then equal to $\log \epsilon$.

The computer code calculates the abundance in a slightly different manner. It computes the theoretical curve of growth for each group of lines

and the position of each line on the empirical curve. Then the difference between the theoretical and empirical abscissas is computed for each line, which yields an abundance for each line in the group. An average abundance is then computed from the individual line abundances. This technique is found to produce results which agree closely with the graphical fitting procedure.

VI. THE ABUNDANCE ANALYSIS

a) Objectives of the Analysis

The abundance analysis was carried out with three objectives in mind. The first was to determine whether there are significant systematic errors in the abundance results which depend on: (i) wavelength, (ii) excitation potential, or (iii) equivalent width. The second objective was to investigate the effect of different thermal and microturbulence models on the results of the abundance analysis. Finally, the last goal was to re-do the solar chromium abundance calculations of Müller and Mutschlecner and to derive a set of empirical Cr I gf-values for use in the atmospheric study of other solar-type stars.

The results of our study and those of CSE provide a means of comparing two different approaches to abundance calculations. The MM study follows the classic GMA method which emphasizes average of large numbers of lines, while CSE emphasizes selectivity and quality of data rather than large numbers of lines.

In order to carry out the analysis, for each line a data card was generated by the abundance computer code discussed in Section V. This card contained λ , $\log(gf)$, χ_u , $\log(W/\lambda)$, and $\log \epsilon$. A third computer code was written expressly for this study; this code analyzes the dependence of $\log \epsilon$ derived for each line on the values of λ , χ_u , and $\log(W/\lambda)$ for that line. The code provides a plot of each dependence and a listing of values from a linear least squares analysis. We shall refer to this analysis for systematic errors as the dependence analysis.

TABLE 3

Abundance Analysis for Beam-Foil gf-Values

RMT No.	Wavelength	log(gf) _{BF}	log W/ λ				log ϵ
			KPNO	MM	KSU	MMH	
1	4254.35	-0.16				-4.03	-6.59
22	4351.05	-1.49		-4.68*	-4.67	-4.70	-6.24
	4412.25	-2.48		-5.21*	-5.20	-5.21	-6.53
	4373.25	-2.21		-5.00*	-5.04	-4.99	-6.52
38	3963.69	0.56 [†]			-4.94*	-4.85	-7.66 [§]
	3969.75	0.52 [†]			-5.70*	-5.45	-8.63 [§]
	3976.67	0.47			-4.60*	-4.78	-6.57
	3983.91	0.35			-4.59*	-4.62	-6.43
	3969.06	-0.64				-5.90	-7.68 [§]
	3984.34	-0.44		-4.82*	-4.86	-4.87	-6.39
	3991.67	-0.51			-4.74*	-4.85	-6.08
	3976.01	-2.21				-4.96	-4.93 [§]
42	3767.43	-1.48				-4.71	-4.98 [§]
104	4374.16	-0.49			-4.60	-4.84*	-5.88 [§]
	4346.83	-0.52		-5.06*	-4.76	-5.05	-6.33
115	3163.76	0.072				-4.79	-6.30
	3155.15	0.021				-4.49	-5.28 [§]
	3160.61	-1.20				-4.57	-4.29 [§]
144	4836.86 [†]	-1.07	-5.47*	-5.45	-5.48	-5.48	-6.27
	4814.27 [†]	-1.21	-5.70*		-5.64	-5.60	-6.39
	4810.73 [†]	-1.30	-5.80*		-5.77	-5.57	-6.41
	4847.18 [†]	-1.85	-6.42*		-6.38	-6.14	-6.45
	4825.51	-1.96	-5.58*		-5.57	-5.43	-5.52 [§]
145	4737.35	-0.03	-4.91*	-4.91	-4.96	-4.94	-6.47
	4730.71	-0.18	-4.95*	-4.99	-5.10	-5.04	-6.41
	4724.42	-0.49	-5.15*	-5.17	-5.16	-5.24	-6.45
150	4540.72 [†]	-0.059		-4.89*		-4.94	-6.36
	4511.90	-0.35		-5.05*		-5.16	-6.41
167	4880.06 [†]	-1.60				-6.00	-6.30
	4874.65 [†]	-1.68				-6.30	-6.52

[†] Lines used by Cocke, Stark, and Evans

[‡] gf-value probably in error

[§] Not used in abundance analysis (Fig. 16, 17, 18)

* Value used for computing log ϵ

b) The Solar Chromium Abundance Resulting from the BF gf-Values
and the Analysis for Possible Systematic Errors

An abundance calculation and dependence analysis was carried out for the Cr I lines for which BF gf-values were available. It was necessary to use a variety of sources for equivalent widths for these lines. The chromium abundance was computed from each of 43 lines at the center of the disk, using the Elste thermal model and our depth-independent microturbulence model introduced in Section IV (the derivation of this model is discussed in part d) of the present section). Table 3 lists the values of $\log(gf)$, $\log(W/\lambda)$, and $\log \epsilon$ for each of these lines. In cases where several equivalent widths were available, the ones felt to be most reliable were used and these are indicated in the table by an asterisk.

Figure 15 is the empirical curve of growth for these lines. The solid line in the figure is the theoretical curve of growth for a wavelength region centered at 4600 \AA and for $\chi_0 = 3.0 \text{ eV}$. One line, $\lambda 4254.35$ (RMT No. 1), is off scale and does not appear in the figure. The two points farthest to the right in figure 15, $\lambda 3963.69$ (RMT No. 38) and $\lambda 3969.75$ (RMT No. 38), are believed to have erroneous gf-values. The nine lines farthest from the mean curve of growth were excluded from the calculation of the mean abundance and are so designated in the figure and in table 3. The filled triangles in figure 15 are the lines used by CSE. These plus the lines shown by filled circles comprise a group of 34 lines for which the data is believed to be reliable.

These 34 lines yield a mean abundance of $\log \epsilon = -6.40$. On a scale of $\log N_H = 12.0$, this gives a chromium abundance of $\log N_{Cr} = 5.60$. The results of the dependence analysis appear in figures 16, 17, and 18. The scatter in the points is large, but there is no significant dependence in any case.

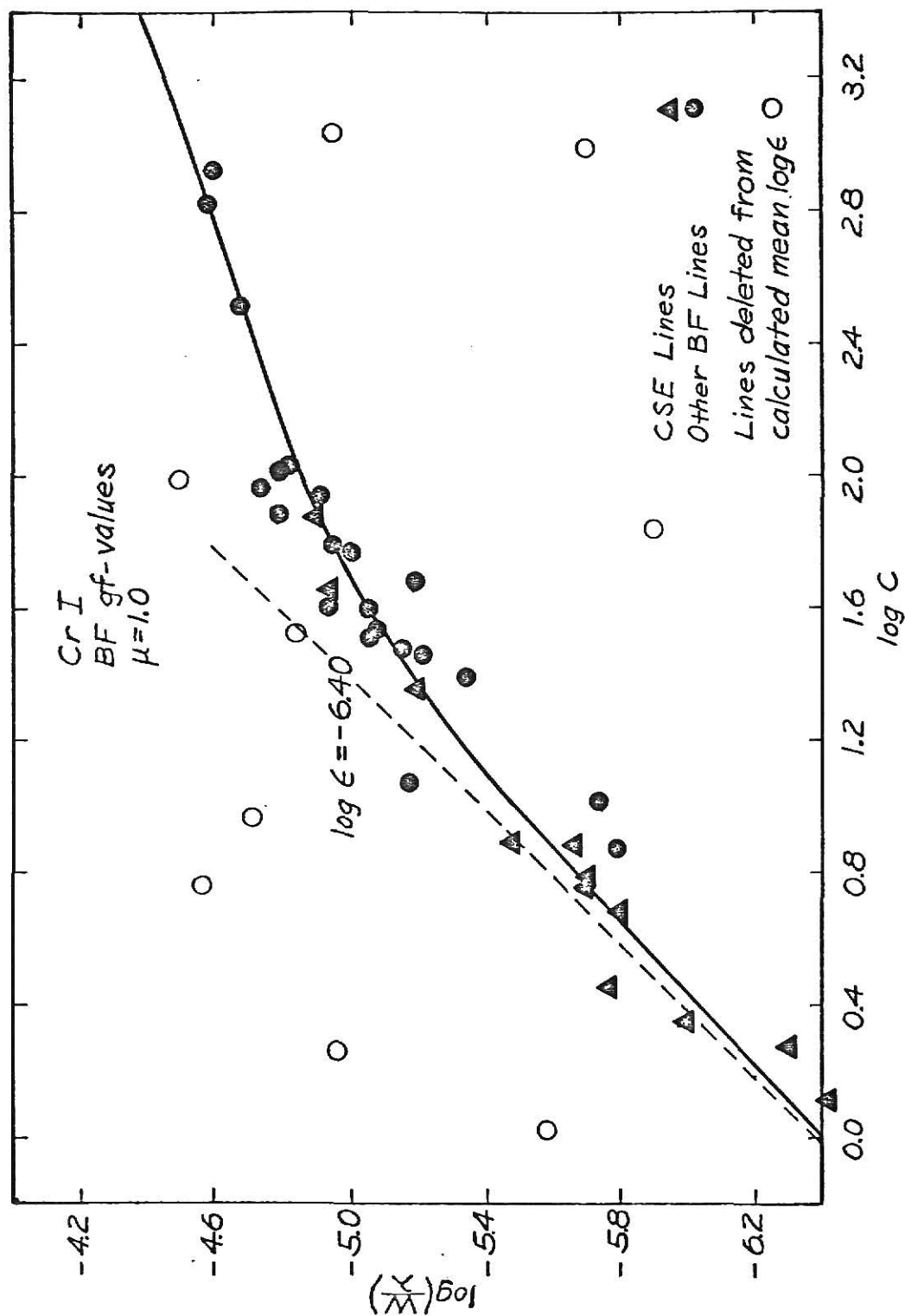


Fig. 15.— The empirical curve of growth constructed with the Cr I beam-foil gf-values of Cocke, Curnutte, and Brand (1971) and Cocke, Stark, and Evans (1973). The filled triangles are points used by CSE to compute the abundance. The circles are additional points from table 3 included in this study. The open circles were not used to compute $\log \epsilon$. The solid line is the theoretical curve of growth, to which has been fitted the 33 points designated by the filled triangles and the filled circles, plus λ 4254.35, which is off scale and does not appear.

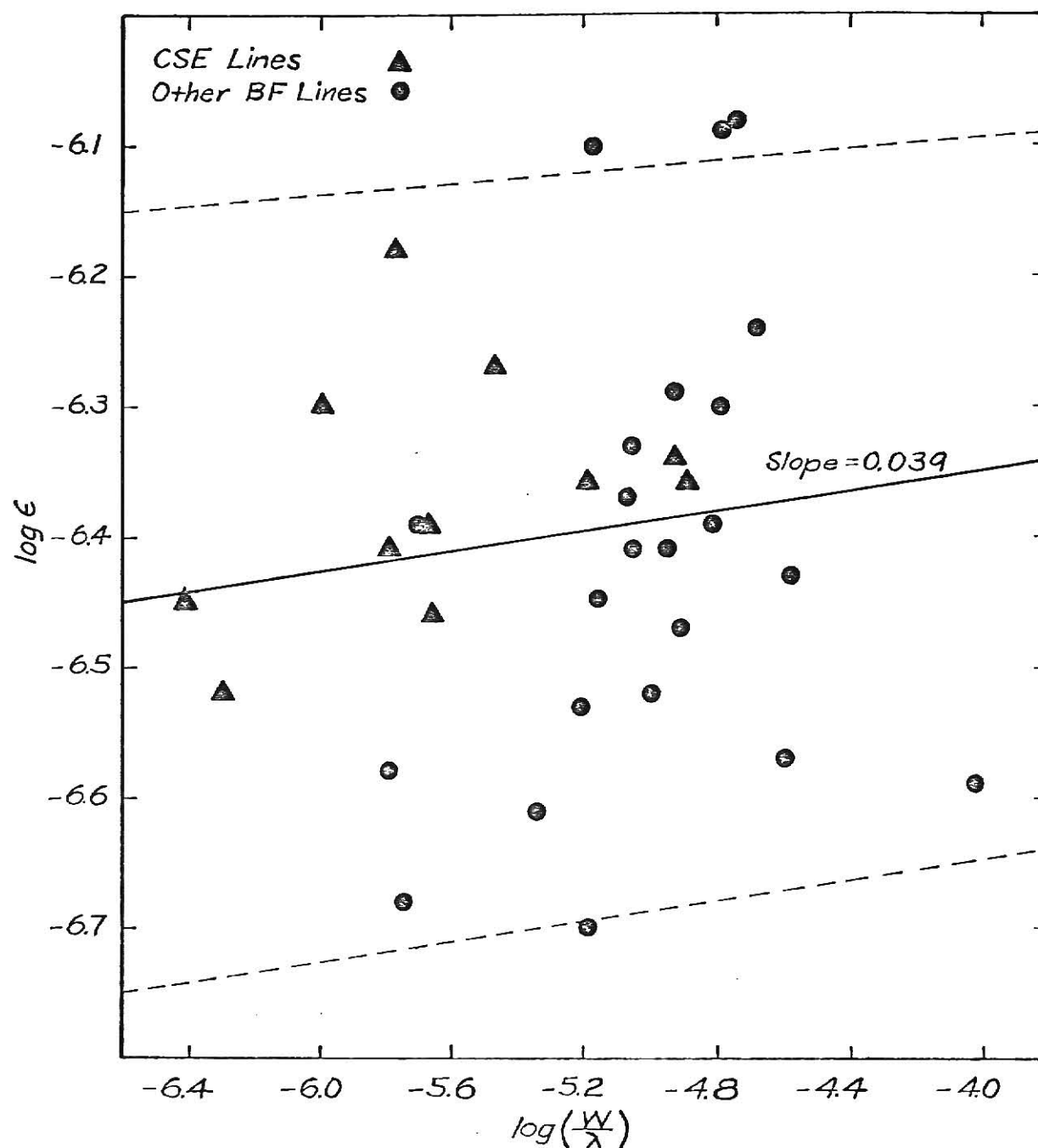


Fig. 18.— The dependence of $\log \epsilon$ on equivalent width for the 34 lines designated by filled triangles and filled circles in figure 15. The triangles are lines used by CSE in their abundance calculation. The solid line is a linear least squares fit to the data with slope as indicated.

CSE computed the chromium abundance using the 11 designated lines in table 3 plus two additional weak lines not included in the table. These 13 lines were carefully selected on the basis of reliability of the gf-values and equivalent widths and such that all were weak lines. The abundance calculation was done using the Elste thermal model but with no microturbulence included, since it is not important for weak lines. They obtained $\log N_{\text{Cr}} = 5.80 \pm 0.11$. Our value agrees reasonably well with their result, in spite of the scatter of the points on figure 15, which is greater than for their curve of growth (see figure 1 in Cocke, Stark, and Evans 1973). The discrepancy may be partly due to the microturbulence included in the present calculation, and partly due to the differences in equivalent widths, since CSE measured all lines from KPNO data.

c) An Outline for Re-doing the Müller and Mutschlecner Study

It is desired to repeat the chromium abundance study of MM using their equivalent widths. The following is an outline of the procedure we have used in re-doing their calculations.

(i) The CB gf-values used by MM have been corrected with the 0.7 dex zero-point shift obtained by CSE, and the CB normalization function has been removed, as discussed in Section III.

(ii) We have developed our own reference microturbulence model on the basis of the dependence analysis. MM used a depth-independent and isotropic microturbulence model with 2.1 km/s velocities.

(iii) As a test on the level of influence of the thermal models, the abundance analysis has been carried out using the Elste, the HSRA, and the Holweger solar models.

(iv) Since the precise dependence on upper excitation potential in the CB gf-values could not be determined from BF gf-values, the influence of an excitation dependent error in the curve of growth has been considered.

(v) The abundance calculation has been done using the Elste thermal model with each of the five microturbulence models in figure 12 to test the influence of the microturbulence model.

(vi) Final line abundances have been computed and analyzed for dependence on λ , χ_u , and $\log(W/\lambda)$, and from these the abundance of chromium in the sun has been determined.

d) Derivation of a Reference Microturbulence Model

The initial calculations were done using the Elste thermal model and a depth-independent and isotropic microturbulence model. If the assumption of LTE is valid, then lines throughout the range of measured equivalent widths and at all limb distances should yield the same chromium abundance. The approximate magnitude of the microturbulence velocity was obtained by analyzing the computed line abundances for a systematic dependence on equivalent width which would result if the wrong microturbulence were used.

If the microturbulence is too large, the saturation portion of the theoretical curve of growth will be too high. As a result, lines in this region will give abundances smaller than do the weak lines which are not affected by the microturbulence. Conversely, if the assumed microturbulence is too small, the moderately strong lines will yield larger abundances than the weak lines.

The calculations were done first with three isotropic, depth-independent microturbulence models which had velocities of 0.0, 0.8, and 1.6 km/s,

respectively. Using the argument above, it was found that the 0.0 and 0.8 km/s velocities were too small at the center of the disk, whereas the 1.6 km/s velocity was too large. Thus, the magnitude of the turbulence velocity appears to be somewhat larger than 1.0 km/s.

We found that a microturbulence velocity adequate to remove the equivalent width effect at the center of the disk would not remove it completely at the limb. This fact suggests an anisotropic model with a tangential velocity greater than the radial velocity, since the lines widen towards the limb. The tangential component would be dominant near the limb where the observer's line-of-sight is more nearly parallel to the photosphere. The radial and tangential velocities finally adopted were $\xi_{\text{rad.}} = 1.2$ km/s and $\xi_{\text{tang.}} = 1.8$ km/s. In this fashion, we have derived our depth-independent and anisotropic microturbulence model (shown in figure 12) as a reference against which we may compare the other models.

It is interesting to note that this model agrees well with that of Athay and Canfield (1969). Their model was developed to fit theoretical line profiles of the strong Mg-b and Na D lines to observed profiles. It is depth-independent except in the outer layers (see figure 12), and the magnitudes of the radial and tangential components are similar to those of our model.

e) Tests of the Dependence of the Chromium Abundance on the Thermal Model

Using our reference microturbulence model, the abundance calculations were made with the Elste, HSRA, and Holweger thermal models at $\mu = 1.0, 0.5$, and 0.3 as a test of the dependence of the results on the thermal model. The mean chromium abundance and the dependence analysis appear in table 4. The calculations summarized in part A of table 4 were made with the CB gf-values from which the normalization function had been removed.

TABLE 4

Summary of Linear Least Squares Abundance Analysis for Three Thermal Models
with Depth-Independent Microturbulence Model

A. Results using CB gf-Values with normalization function removed

Relation	Thermal Model	$\mu = 1.0$		$\mu = 0.5$		$\mu = 0.3$	
		Slope	Intercept	Slope	Intercept	Slope	Intercept
$\log \epsilon$ vs λ	Elste	0.136 dex/ 10^3\AA	-7.60 dex	0.170 dex/ 10^3\AA	-7.80 dex	0.177 dex/ 10^3\AA	-7.82 dex
	HSRA	0.140	-7.60	0.170	-7.77	0.179	-7.81
	Holweger	0.127	-7.43	0.150	-7.56	0.160	-7.59
$\log \epsilon$ vs χ_u	Elste	-0.129 dex/eV	-6.24 dex	-0.111 dex/eV	-6.38 dex	-0.112 dex/eV	-6.35 dex
	HSRA	-0.133	-6.21	-0.104	-6.39	-0.091	-6.45
	Holweger	-0.162	-5.94	-0.150	-6.02	-0.160	-5.95
$\log \epsilon$ vs $\log \frac{W}{\lambda}$	Elste	0.060	-6.63 dex	0.033	-6.81 dex	0.055	-6.68 dex
	HSRA	0.058	-6.62	0.026	-6.81	0.021	-6.84
	Holweger	0.114	-6.21	0.118	-6.23	0.164	-5.97
Mean $\log \epsilon$	Elste		-6.94 dex		-6.97 dex		-6.96 dex
	HSRA		-6.92		-6.95		-6.94
	Holweger		-6.81		-6.83		-6.81

TABLE 4 (Cont'd)

B. Results using CB gf-Values with normalization function removed,
zero-point correction, and χ -dependence removed*

Relation	Thermal Model	$\mu = 1.0$		$\mu = 0.5$		$\mu = 0.3$	
		Slope	Intercept	Slope	Intercept	Slope	Intercept
$\log \epsilon$ vs λ	Elste	0.113 dex/ 10^3\AA	-6.79 dex	0.146 dex/ 10^3\AA	-6.99 dex	0.154 dex/ 10^3\AA	-7.01 dex
	HSRA	0.115	-6.78	0.145	-6.95	0.154	-6.99
	Holweger	0.0972	-6.58	0.120	-6.72	0.130	-6.74
$\log \epsilon$ vs χ_u	Elste	0.001 dex/eV	-6.24 dex	0.019 dex/eV	-6.37 dex	0.017 dex/eV	-6.35 dex
	HSRA	0.001	-6.22	0.030	-6.40	0.042	-6.47
	Holweger	0.001	-6.11	0.012	-6.20	0.003	-6.13
$\log \epsilon$ vs $\log \frac{W}{\lambda}$	Elste	-0.044	-6.47 dex	-0.080	-6.68 dex	-0.062	-6.57 dex
	HSRA	-0.049	-6.47	-0.089	-6.70	-0.099	-6.74
	Holweger	-0.016	-6.19	-0.023	-6.25	0.019	-6.02
Mean $\log \epsilon$	Elste	-6.24 dex		-6.27 dex		-6.26 dex	
	HSRA	-6.22		-6.25		-6.24	
	Holweger	-6.11		-6.13		-6.11	

* χ -dependence removed using slope in Part A of Table 4 at $\mu = 1.0$

It is apparent that the mean solar chromium abundance is not strongly dependent on the particular thermal model used. The mean $\log \epsilon$ for the 116 lines differs by only 0.02 dex between the Elste and HSRA models at all positions on the disk, while the Holweger model gives values about 0.1 dex larger than the other two thermal models. For each limb position, the results of the least squares analysis for dependence of $\log \epsilon$ on λ , χ_u , and $\log(W/\lambda)$ are listed in table 4 as the slope and the intercept of the linear fit to the data.

The dependence of $\log \epsilon$ on λ may be due to systematic errors in either the gf-values or the equivalent widths. Since the majority of the MM lines lie in the interval $\lambda\lambda$ 4000-5000 Å (see table 7), the effect is small and does not appear to be significant. A much larger wavelength dependence would be predicted on the basis of figure 9. However, the lines in figure 9 cover a broader wavelength range than the 116 MM lines and contain more lines in the blue.

The dependence of $\log \epsilon$ on $\log(W/\lambda)$ is also small, since most of it has been removed by optimizing the values of the radial and tangential components of the microturbulence model.

There is a significant systematic dependence of $\log \epsilon$ on χ_u . This ranges among the three models from about 0.3 dex to 0.5 dex over the 3 eV spread in excitation potential of the lines. This effect could be an indication of departures from the conditions of LTE, particularly if there were a strong center-to-limb effect. However, none of the models shows a significant center-to-limb effect. In Section II, it was argued that the CB gf-values have an apparent dependence on χ_u of about + 0.2 dex/eV, when the normalization function is removed. This has the same order of magnitude as the $\log \epsilon$ dependence, and it is of opposite sign. This suggests that the $\log \epsilon$ dependence on χ_u results from systematic errors in the CB gf-values.

The computed mean chromium abundance in part A of table 4 must be corrected for the 0.7 dex zero-point error in the CB gf-values mentioned earlier. Also, if we assume that the χ_u -dependence of $\log \epsilon$ is due to systematic errors in the CB gf-values, this effect can be removed. The dependence on χ_u is somewhat different at the three limb positions, so we decided to apply the correction by removing the slope at $\mu = 1.0$ for each model (e.g., -0.129 dex/eV for the Elste thermal model), rotating about the intercept. The same correction was then applied to the two other limb positions.

After these two corrections were made to the CB gf-values, the abundance for each line was recomputed. The corrected abundances were again subjected to the dependence analysis at each of the three limb positions. These calculations are summarized in part B of table 4. There is only a small change in the wavelength dependence and a somewhat larger change in the equivalent width dependence. As far as the mean abundances are concerned, the influence of the thermal model is about ± 0.1 dex.

f) The Influence of Systematic Errors Which Depend on Excitation Potential in Both the Empirical and Theoretical Curves of Growth

The results in parts A and B of table 4 can be used to look for another effect caused by systematic errors in gf-values mentioned in Section III. Such errors can distort the shape of the curve of growth (Evans and Schroeder 1972). This is due to the tendency for weak lines to have higher excitation potentials than strong lines. Thus a χ -dependent error in the gf-values can produce a shift in the positions on the empirical curve of growth of weak lines relative to strong lines. The computed abundances will be shifted by the same amount from their true values. If the effect is large enough it may even be falsely attributed to a large microturbulence velocity.

Table 4 confirms a correlation between the dependence on excitation potential and the equivalent width dependence. Part A of table 4 shows for each model an equivalent width dependence having a small positive slope at all limb distances. This becomes a small negative slope in each case after removal of the χ -dependence, as can be seen in part B of the table. This suggests that the small dependence on equivalent width is probably due to the above mentioned cause.

The abundance calculation itself can be the source of systematic errors if it is not carried out with care. In Section V, we mentioned the importance of grouping lines by excitation potential in doing the abundance calculation. If a line has an excitation potential greatly different from that used to compute the theoretical curve of growth, the abundance derived for that line may be in error. In figure 19, we illustrate this point. The abundance calculation was performed three times for a particular group of lines having a lower excitation potential of about 2.5 eV. In one calculation, the excitation potential for the theoretical curve of growth was 2.5 eV. For the other two, the excitation potential was set at 4.0 eV and 1.0 eV, respectively. The ordinate of figure 19 shows the deviation of the abundances derived in the last two cases from those computed with the proper lower excitation potential. We find that if the value of χ_0 used in the computation of the theoretical curve of growth is too small, the abundances derived from the stronger lines are too large. On the other hand, if the value of χ_0 is too large, the abundances derived from the strong lines are too small. In either case, the error is enhanced with increasing equivalent width.

An important and somewhat surprising result can be seen in table 4. If one compares the mean abundance computed before and after the correction of the zero-point error and the χ -dependence of the gf-values, it is seen that

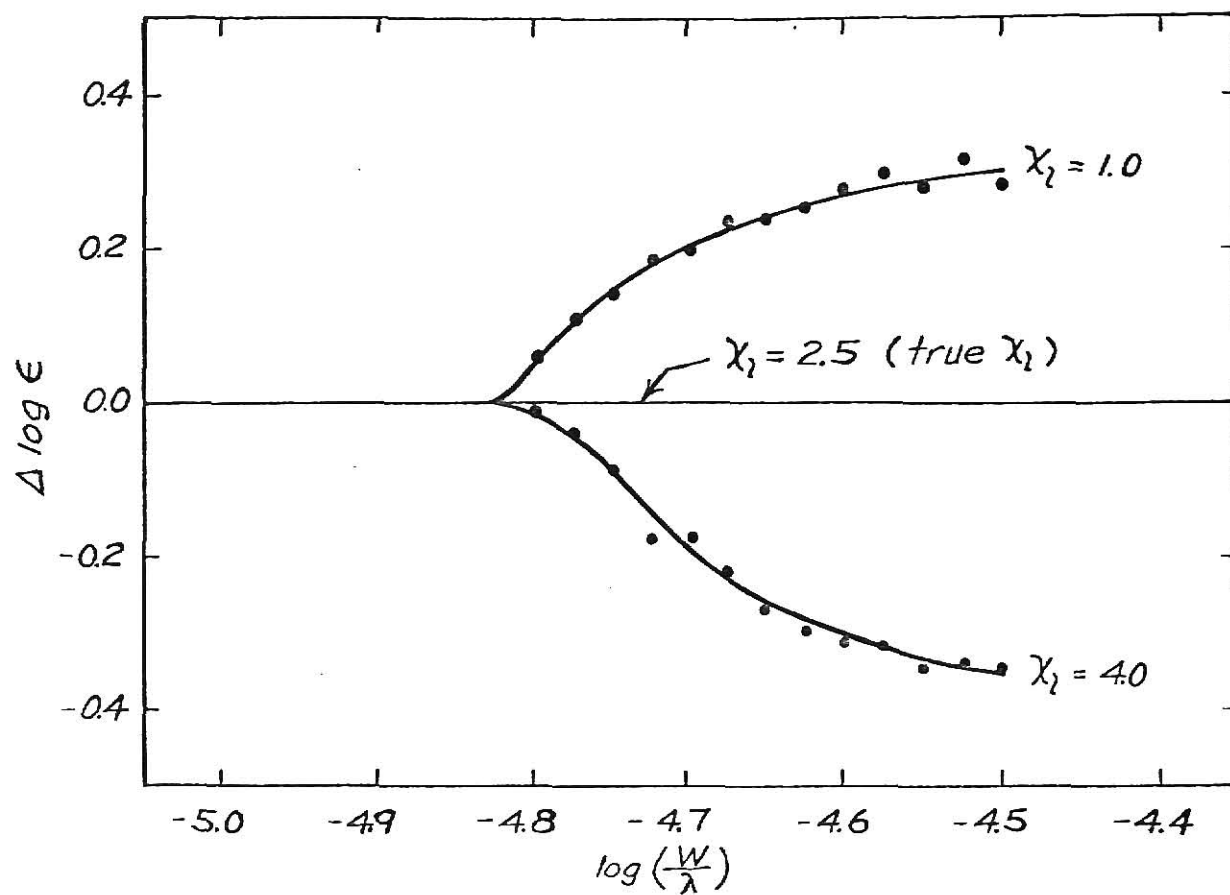


Fig. 19.— The effect of using the wrong lower excitation potential to calculate the theoretical curve of growth. For the lines in this example $\chi_l \approx 2.5$, and $\Delta \log \epsilon$ is the difference between the value of $\log \epsilon$ computed with $\chi_l = 1.0$ or 4.0 and the value of $\log \epsilon$ with $\chi_l = 2.5$.

the mean abundance differs by exactly 0.7 dex at all limb distances in each model. This suggests that the most important systematic error in abundance studies is the 0.7 dex zero-point error in the CB gf-values. This, of course was the largest of the systematic errors and it may be fortuitous that the other errors were not as significant. Nevertheless, systematic errors dependent on excitation energy can be a significant source of error for abundance calculations which involve only a few lines.

Figure 20 is the empirical curve of growth for the abundance calculation at the center of the disk with the Elste thermal model and the depth-independent, anisotropic microturbulence model. The gf-values used in this calculation are uncorrected, and $\log \epsilon = -6.94$. The solid line is the superimposed theoretical curve of growth.

Figure 21 is the same curve of growth after the gf-values were corrected for the zero-point error and the χ -dependence. Here $\log \epsilon = -6.22$. The lines of high excitation potential have been shifted 0.2-0.3 dex to the left relative to lines of low excitation potential. However, the majority of lines remain substantially unchanged in their relative positions after removal of the χ -dependence. We do not appear to have as strong a correlation between line strength and excitation potential as that observed by Evans and Schroeder (1972) for iron curves of growth. Figures 22 and 23 are the curves of growth at $\mu = 0.5$ and $\mu = 0.3$, respectively, after correction of the gf-values. The abundances from these curves are $\log \epsilon = -6.26$ at $\mu = 0.5$ and $\log \epsilon = -6.24$ at $\mu = 0.3$. Comparison of figures 21 through 23 reveals no center-to-limb effect in the curve of growth.

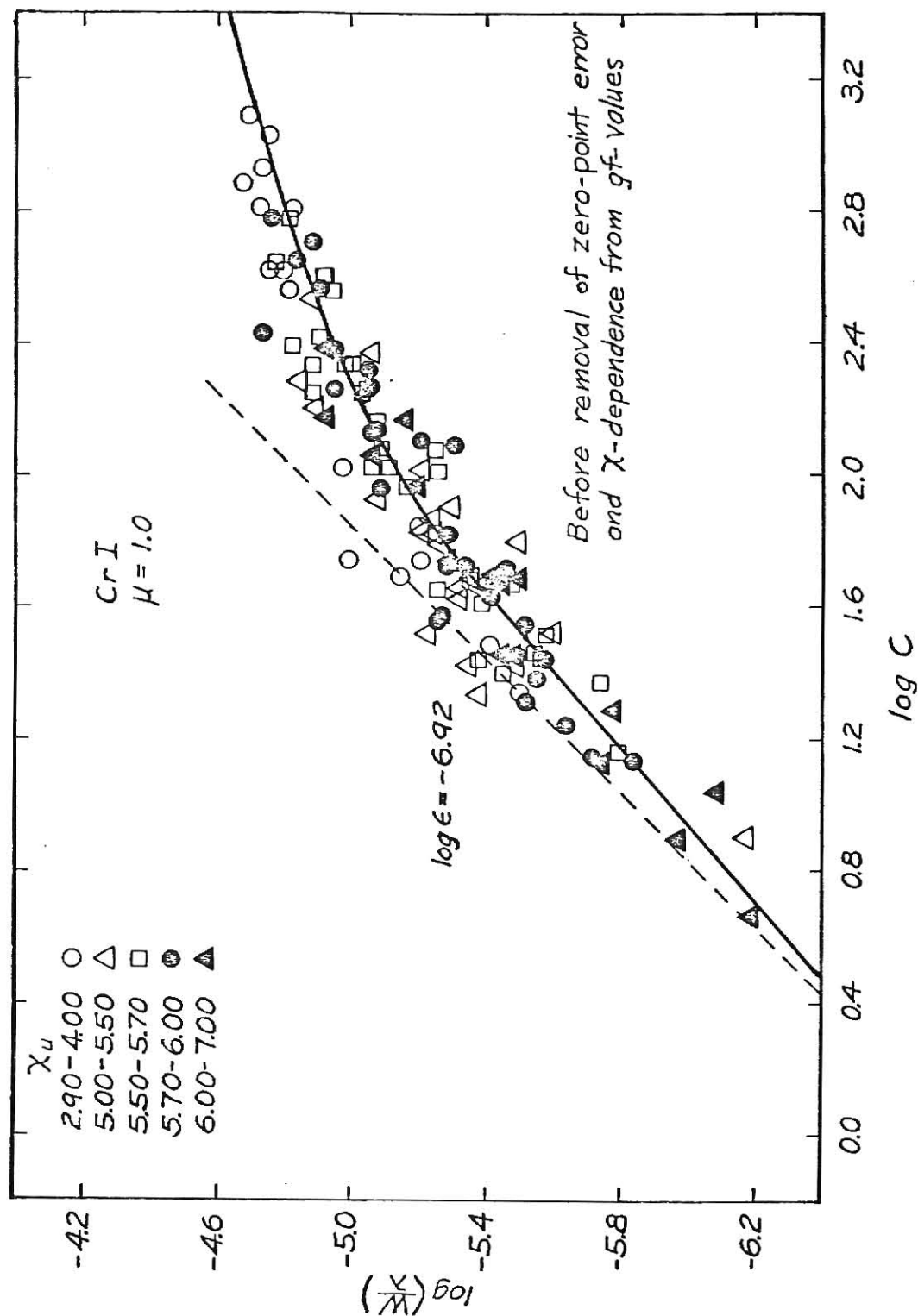


Fig. 20.— The empirical curve of growth for the 116 MM Cr I lines. The calculation was made with the Elste thermal model and the depth-independent microturbulence model at $\mu = 1.0$, using uncorrected CB gf-values. The symbols designate the points by range in upper excitation potential in electron volts. The solid line is the theoretical curve of growth, as it was fit to the empirical curve to obtain $\log \epsilon = -6.92$.

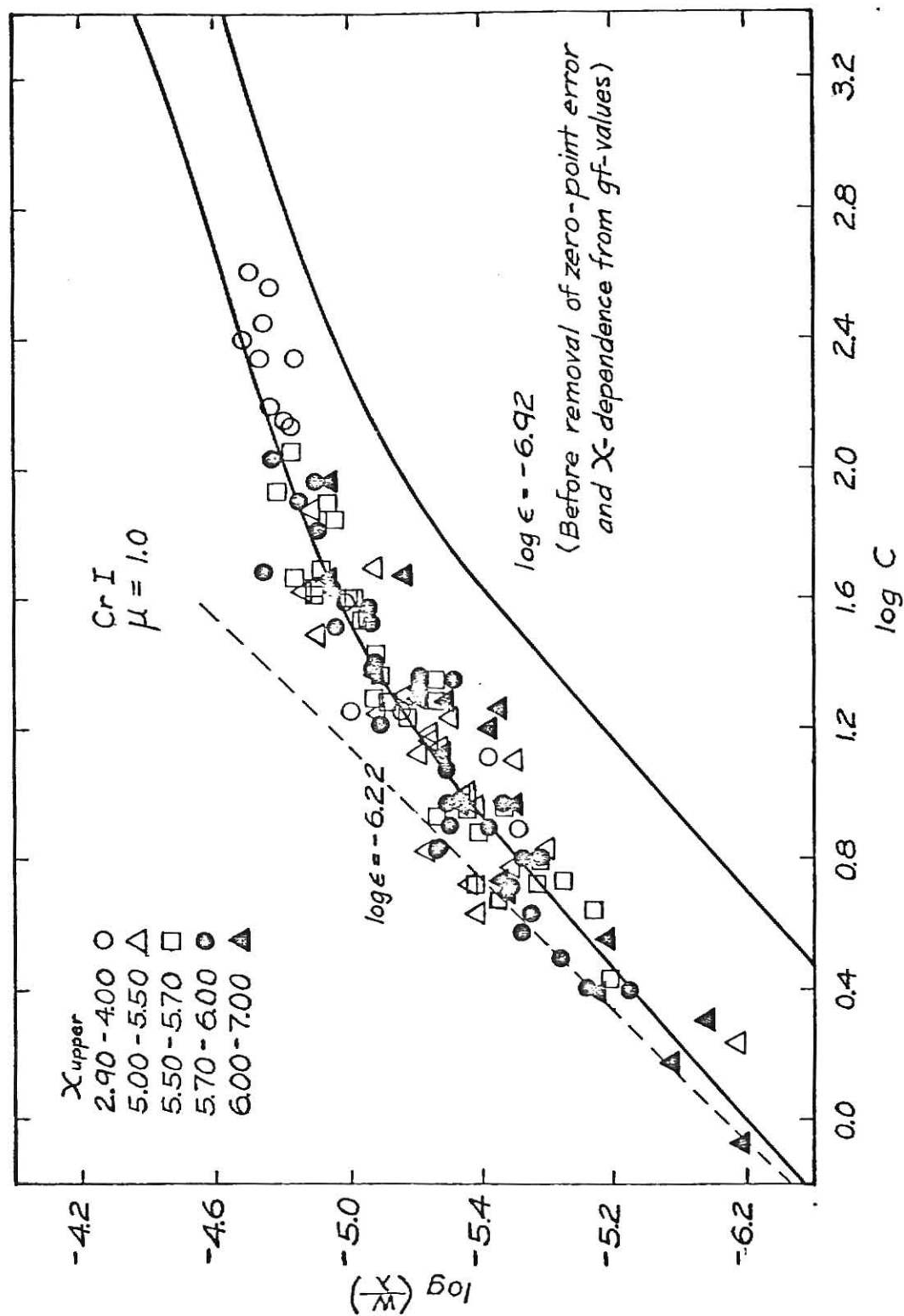


Fig. 21.— The empirical curve of growth for the 116 MM Cr I lines at $\mu = 1.0$, after correction of the zero-point error and the χ -dependence in the gf-values. This curve of growth gives $\log \epsilon = -6.22$. The lower curve is the position of the theoretical curve from figure 20.

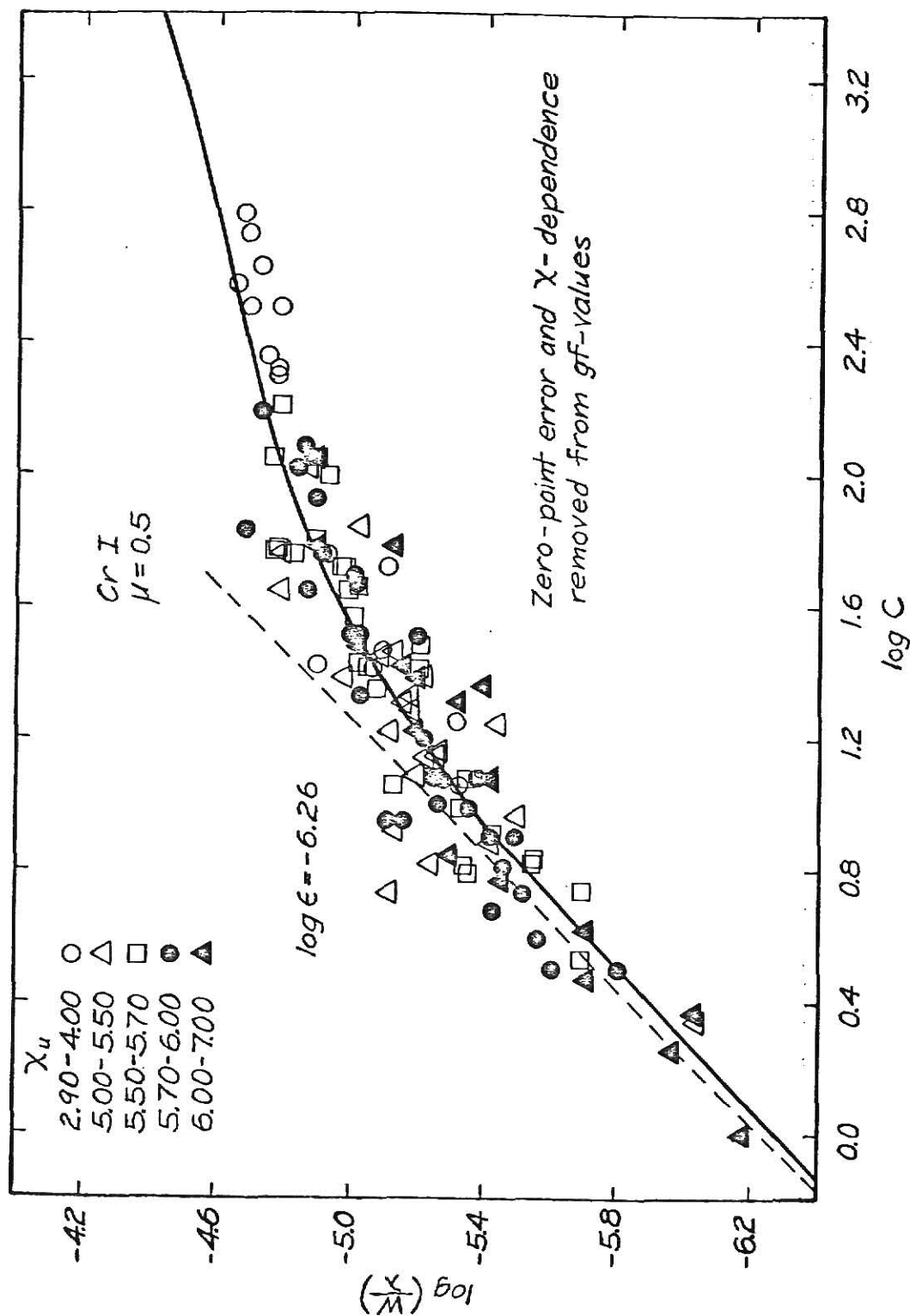


Fig. 22.— The empirical curve of growth for the 116 MM Cr I lines at $\mu = 0.5$, after the correction of the zero-point error and the χ -dependence in the gf -values.

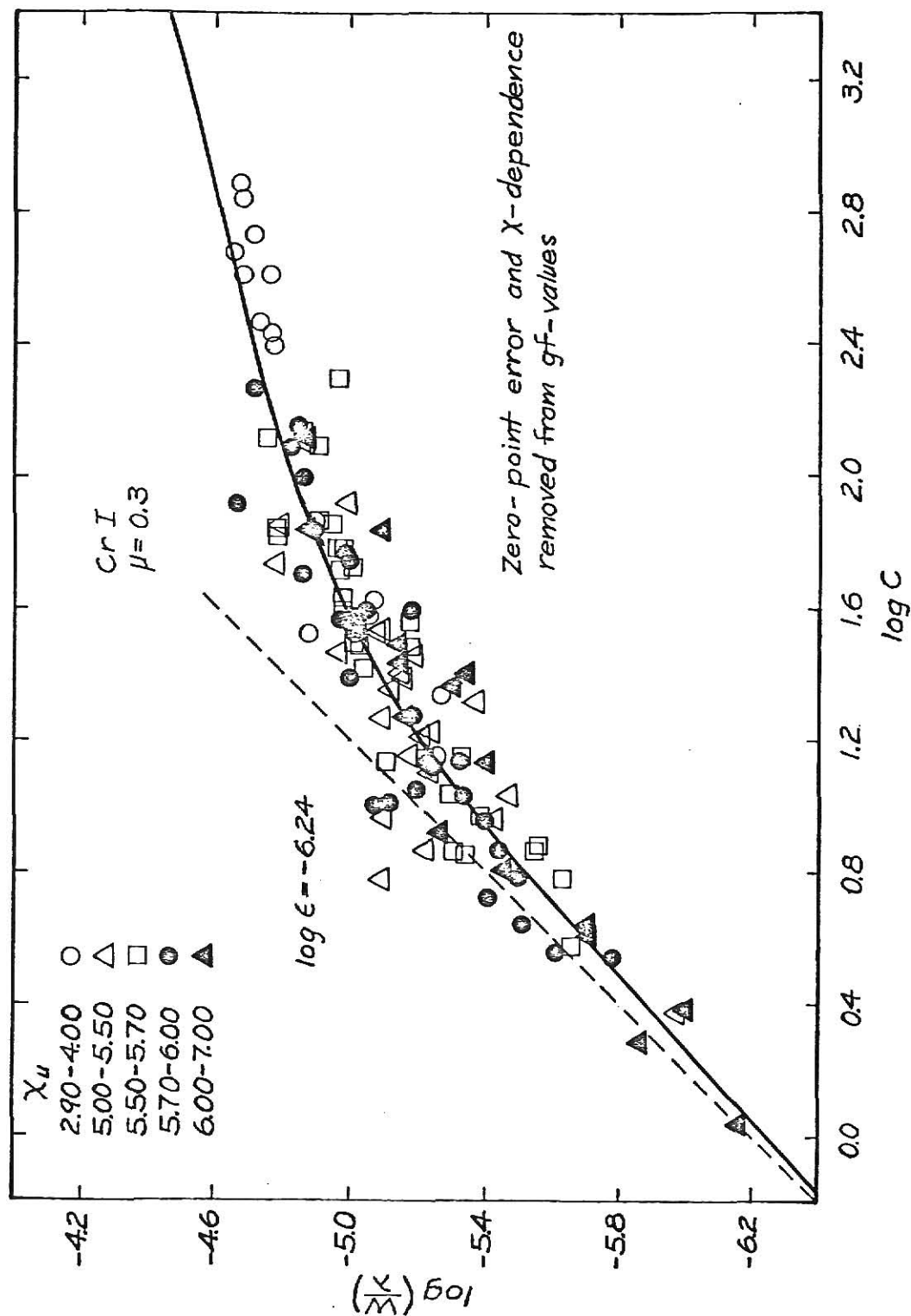


Fig. 23.— The empirical curve of growth for the 116 MM Cr I lines at $\mu = 0.3$, after correction of the zero-point error and the χ -dependence in the gf -values.

g) The Calculation of an Empirical Set of Neutral Chromium gf-Values

In solar studies, the line equivalent width data is likely to be more reliable than the laboratory gf-values. Much of the scatter of points on the curve of growth is probably due to random errors in the gf-values. We can derive a set of empirical gf-values from our computed mean abundance. This has been done at $\mu = 1.0$ by changing the gf-value of each line to that value which yields a computed abundance equal to the mean abundance. This provides a set of gf-values which may be useful for the study of the atmospheres of other solar-type stars since all of these gf-values yield the same abundance in the sun.

Table 5 summarizes our investigation of the errors in the neutral chromium gf-values for the 116 MM lines. The first two columns are the revised multiplet number and wavelength taken from Moore (1945). The third column is the upper excitation potential in electron volts. The next three columns list the original and the corrected CB gf-values. The seventh column contains the empirically derived gf-values. In the eighth column, $\Delta \log(gf) = \log(gf)_{\text{EMP}} - \log(gf)_{\text{CB}}$. The last column gives the BF gf-values, where they are available.

h) Tests of the Dependence of the Chromium Abundance on the Microturbulence Model

In view of the great differences among microturbulence models currently in use, it is important to know how different models may affect the abundance calculation. Since figure 12 presents a representative sample of the different models in use, it was decided to do abundance calculations with each of the five microturbulence models, using the Elste thermal model. The calculations

TABLE 5

Comparison of CB $\log(\text{gf})$ -Values with Corrected $\log(\text{gf})$ -Values

RMT No.	Wavelength	χ_u	$\log(\text{gf})_{\text{CB}}$	$\log(\text{gf})_{\text{CB}_1}^*$	$\log(\text{gf})_{\text{CB}_2}^+$	$\log(\text{gf})_{\text{EMP}}^\#$	$\Delta\log(\text{gf})$	$\log(\text{gf})_{\text{BF}}$
6	6330.10	2.90	-2.52	-2.52	-2.89	-3.06	-0.54	
8	5072.92	3.38	-2.26	-2.26	-2.70	-2.81	-0.55	
9	4964.93	3.44	-2.30	-2.30	-2.74	-2.71	-0.41	
10	4496.86	3.70	-0.91	-0.91	-1.39	-1.49	-0.58	
	4545.96	3.67	-0.97	-0.97	-1.44	-1.76	-0.79	
	4580.06	3.65	-1.20	-1.20	-1.67	-1.63	-0.43	
18	5296.70	3.32	-1.36	-1.36	-1.79	-1.67	-0.31	
	5300.75	3.32	-1.96	-1.96	-2.39	-2.39	-0.43	
	5247.57	3.32	-1.44	-1.44	-1.87	-1.93	-0.49	
20	5123.47	3.45	-2.58	-2.58	-3.03	-3.11	-0.53	
21	4600.76	3.69	-1.02	-1.02	-1.50	-1.61	-0.59	
	4591.40	3.66	-1.18	-1.18	-1.65	-2.03	-0.85	
	4613.37	3.65	-1.37	-1.37	-1.84	-1.91	-0.54	
22	4351.05	3.81	-1.07	-1.07	-1.56	-1.38	-0.31	-1.49
	4412.25	3.84	-2.06	-2.06	-2.56	-2.72	-0.66	-2.48
	4373.25	3.81	-1.79	-1.79	-2.28	-2.43	-0.64	-2.21
30	4885.77	5.07	-0.70	-0.70	-1.35	-1.39	-0.69	

* Normalization function removed

† Normalization function removed, zero-point error corrected, χ -dependence removed at $\mu = 1.0$ ‡ Empirically determined from final mean curve-of-growth at $\mu = 1.0$

TABLE 5 (Cont'd)

RMT No.	Wavelength	X_u	$\log(gf)_{CB}$	$\log(gf)_{CB}^*$	$\log(gf)_{CB_1}^+$	$\log(gf)_{CB_2}^+$	$\log(gf)_{EMP}^+$	$\Delta\log(gf)$	$\log(gf)_{BF}$
31	4789.34	5.11	0.05	0.05	-0.61	-0.69	-0.74		
	4829.37	5.09	-0.21	-0.21	-0.87	-0.62	-0.41		
32	4571.68	5.24	-0.09	-0.09	-0.77	-1.06	-0.97		
	4637.18	5.20	-0.57	-0.57	-1.24	-1.41	-0.84		
	4648.12	5.20	-0.81	-0.81	-1.48	-1.45	-0.64		
	4649.44	5.20	-0.64	-0.64	-1.31	-1.33	-0.69		
33	4529.85	5.27	-0.78	-0.78	-1.46	-1.48	-0.70		
	4541.07	5.26	-0.60	-0.60	-1.28	-1.32	-0.72		
	4535.15	5.26	-0.48	-0.48	-1.16	-1.22	-0.74		
	4539.79	5.26	-0.54	-0.54	-1.22	-1.08	-0.54		
35	4126.52	5.53	0.14	0.14	-0.57	-0.82	-0.96		
	4203.57	5.48	-0.27	-0.27	-0.98	-0.76	-0.49		
37	4026.17	5.61	0.11	0.11	-0.61	-0.85	-0.96		
38	3984.34	5.64	0.33	0.33	-0.40	-0.54	-0.87		-0.44
59	5238.97	5.07	-0.89	-0.89	-1.54	-1.47	-0.58		
60	5110.77	5.13	-0.67	-0.67	-1.33	-1.26	-0.59		
61	4745.32	5.31	-0.77	-0.77	-1.46	-1.58	-0.81		
62	4697.06	5.34	-0.27	-0.27	-0.96	-1.09	-0.82		
	4700.62	5.34	-0.49	-0.49	-1.18	-1.46	-0.97		
64	4295.76	5.59	0.01	0.01	-0.71	-0.59	-0.60		
	4381.12	5.53	-0.26	-0.26	-0.97	-0.98	-0.72		
65	4120.62	5.71	-0.21	-0.21	-0.95	-1.27	-1.06		
66	4077.07	5.74	-0.20	-0.20	-0.94	-1.13	-0.93		

TABLE 5 (Cont'd)

RMT No.	Wavelength	χ_u	$\log(\text{gf})_{\text{CB}}$	$\log(\text{gf})_{\text{CB}_1}^*$	$\log(\text{gf})_{\text{CB}_2}^+$	$\log(\text{gf})_{\text{EMP}}^\#$	$\Delta\log(\text{gf})$	$\log(\text{gf})_{\text{BF}}$
67	3992.83 3978.67	5.80 5.82	0.49 0.14	0.49 0.14	-0.26 -0.61	-0.20 -0.13	-0.69 -0.27	
81	4619.54 4501.78 4622.75	5.65 5.65 5.65	0.11 -0.45 -0.37	0.11 -0.45 -0.37	-0.62 -1.18 -1.10	-0.67 -0.99 -1.06	-0.78 -0.54 -0.69	
	4501.10 4498.73	5.65 5.66	-0.10 -0.10	-0.10 -0.10	-0.83 -0.83	-0.77 -0.99	-0.67 -0.89	
	4432.17	5.66	-0.12	-0.12	-0.85	-0.74	-0.62	
99	4693.95 4695.16	5.61 5.61	0.01 -0.39	0.01 -0.39	-0.71 -1.11	-0.94 -1.20	-0.95 -0.81	
104	4346.83	5.82	0.20	0.20	-0.55	-0.67	-0.87	-0.52
119	5719.82	5.17	-1.09	-1.09	-1.76	-1.87	-0.78	
127	4458.53 4465.36	5.78 5.78	0.37 -0.19	0.37 -0.19	-0.38 -0.94	-0.39 -0.93	-0.76 -0.74	
143	4922.27 4887.01 4870.80 4885.96	5.61 5.61 5.62 5.61	0.71 0.40 0.44 -0.44	0.71 0.40 0.44 -0.44	-0.01 -0.32 -0.29 -1.16	0.17 -0.17 0.00 -1.22	-0.54 -0.57 -0.44 -0.78	
144	4836.86	5.65	-0.53	-0.53	-1.26	-1.05	-0.52	-1.07
145	4737.35 4730.71 4724.42	5.69 5.69 5.69	0.48 0.39 0.02	0.48 0.39 0.02	-0.25 -0.34 -0.71	-0.20 -0.38 -0.68	-0.68 -0.77 -0.70	-0.03 -0.18 -0.49
147	4656.19	5.73	-0.36	-0.36	-1.10	-0.82	-0.46	
150	4540.72 4511.90	5.82 5.82	0.78 0.37	0.78 0.37	0.03 -0.38	-0.18 -0.52	-0.96 -0.89	-0.06 -0.35

TABLE 5 (Cont'd)

RMT No.	Wavelength	χ_u	$\log(\text{gf})_{\text{CB}}$	$\log(\text{gf})_{\text{CB}_1}^*$	$\log(\text{gf})_{\text{CB}_2}^{\dagger}$	$\log(\text{gf})_{\text{EMP}}^{\ddagger}$	$\Delta\log(\text{gf})$	$\log(\text{gf})_{\text{BF}}$
166	4954.81 4936.34	5.61 5.61	0.33 0.33	0.33 0.33	-0.39 -0.39	-0.44 -0.48	-0.77 -0.81	
168	4801.03	5.69	0.42	0.42	-0.31	-0.39	-0.81	
170	4680.86	5.73	-0.36	-0.36	-1.10	-0.80	-0.44	
186	4718.43 4708.04 4689.37 4669.34 4666.51 4664.80	5.81 5.78 5.75 5.81 5.79 5.77	0.82 0.70 0.24 0.10 0.26 0.37	0.82 0.70 0.24 0.10 0.26 0.37	0.07 -0.05 -0.50 -0.65 -0.49 -0.38	0.08 -0.10 -0.48 -0.48 -0.45 -0.25	-0.74 -0.80 -0.72 -0.58 -0.71 -0.62	
188	5787.99 5785.82 5785.00 5783.93 5783.11	5.45 5.45 5.45 5.45 5.45	0.12 -0.37 -0.28 -0.18 -0.04	0.12 -0.37 -0.28 -0.18 -0.04	-0.58 -1.07 -0.98 -0.88 -0.74	-0.47 -0.71 -0.67 -0.50 -0.71	-0.59 -0.34 -0.39 -0.32 -0.67	
191	5405.00 5386.97	5.65 5.65	-0.21 -0.07	-0.21 -0.07	-0.94 -0.80	-1.01 -0.72	-0.80 -0.65	
193	5221.77 5214.12	5.73 5.73	-0.02 -0.22	-0.02 -0.22	-0.76 -0.96	-0.57 -0.82	-0.55 -0.60	
196	4526.11	6.10	-0.23	-0.16	-0.95	-0.80	-0.57	
201	5243.40 5177.43 5200.19	5.74 5.80 5.75	-0.01 0.11 0.07	-0.01 0.11 0.07	-0.75 -0.64 -0.67	-0.71 -0.73 -0.62	-0.70 -0.84 -0.69	
203	5702.31 5628.65	5.60 5.61	-0.14 -0.15	-0.14 -0.15	-0.86 -0.87	-0.59 -0.82	-0.45 -0.67	
204	5480.50 5442.41	5.69 5.69	-0.19 -0.42	-0.19 -0.42	-0.92 -1.15	-0.98 -1.05	-0.79 -0.63	-0.80

TABLE 5 (Cont'd)

RMT No.	Wavelength	χ_u	$\log(\text{gf})_{\text{CB}}$	$\log(\text{gf})_{\text{CB}_1}^*$	$\log(\text{gf})_{\text{CB}_2}^+$	$\log(\text{gf})_{\text{EMP}}^{\ddagger}$	$\Delta\log(\text{gf})$	$\log(\text{gf})_{\text{BF}}$
206	5193.50	5.80	-0.37	-0.37	-1.12	-0.93	-0.56	
225	5272.00	5.78	0.12	0.12	-0.63	-0.50	-0.62	
	5287.18	5.76	-0.47	-0.47	-1.21	-1.01	-0.54	
	5304.18	5.79	-0.20	-0.20	-0.95	-0.81	-0.61	
	5312.86	5.76	-0.06	-0.06	-0.80	-0.79	-0.73	
	5318.78	5.75	-0.07	-0.07	-0.81	-0.87	-0.80	
	5344.76	5.75	-0.47	-0.47	-1.21	-1.14	-0.67	
	5340.46	5.74	-0.30	-0.30	-1.04	-0.80	-0.50	
231	4767.86	6.14	0.18	0.26	-0.53	-0.68	-0.86	
233	4622.49	6.22	0.57	0.68	-0.13	-0.08	-0.65	0.07
234	4413.85	6.35	0.41	0.56	-0.26	-0.38	-0.79	
239	5694.74	6.02	0.23	0.27	-0.51	-0.32	-0.55	
	5642.39	6.04	-0.29	-0.24	-1.02	-0.86	-0.57	
	5649.39	6.01	-0.08	-0.04	-0.82	-0.64	-0.56	
243	5746.42	5.99	-0.55	-0.52	-1.29	-1.10	-0.55	
247	4263.14	6.74	0.90	1.24	0.38	0.16	-0.74	0.33
248	4209.36	6.78	0.89	1.26	0.39	-0.06	-0.95	
249	4208.36	6.78	0.42	0.79	-0.08	-0.30	-0.72	
251	4039.10	6.89	1.13	1.57	0.68	0.18	-0.95	0.40
261	4131.36	6.83	0.48	0.88	-0.00	-0.17	-0.65	
	4152.77	6.82	0.33	0.72	-0.16	-0.17	-0.50	
272	4204.46	6.91	0.53	0.98	0.09	-0.20	-0.73	
282	6661.08	6.03	0.40	0.44	-0.34	-0.33	-0.73	
	6669.31	6.02	0.14	0.18	-0.60	-0.67	-0.81	

were done in exactly the same manner as described for the three thermal models. The dependence analysis and the mean abundance derived with each model is given in table 6.

Although the microturbulence models are quite different, the results are remarkably similar and the mean abundance at the center of the disk varies by only about 0.1 dex among the different models. The differences in the mean abundance are greater at $\mu = 0.5$ and $\mu = 0.3$. Note, in particular, that the center-to-limb variation is greatest with the de Jager-Neven model, which is isotropic. The other models all have a tangential microturbulence velocity which is greater than the radial velocity, and these do not show as large a center-to-limb variation. As was observed for the thermal models, the values of $\log \epsilon$ before and after the correction of the gf-values differ by exactly 0.7 dex in each case.

The depth-independent and Athay-Canfield models have the smallest center-to-limb variation. The ratio of the tangential velocity to the radial velocity is about the same in each, but the velocities are somewhat larger in the depth-independent model, resulting in a slightly smaller value of the mean abundance for this model.

The Holweger and Schmalberger models, both of which have velocities increasing with depth, show a small decrease in abundance towards the limb. This suggests that the tangential components of their velocities are too large relative to their radial components at the depths where the lines are formed.

Figure 24 shows the χ -dependence in the abundances computed with the five different microturbulence models at $\mu = 1.0$, using the original CB gf-values. The Holweger and Schmalberger models give a somewhat smaller dependence than the others. Figures 25 and 26 show the dependence of $\log \epsilon$ on λ

TABLE 6

Summary of Least Squares Abundance Analysis for Five Microturbulence Models with Elste Solar 10 Thermal Model

A. Results using CB gf-Values with normalization function removed

Relation	Microturbulence Model	$\mu = 1.0$		$\mu = 0.5$		$\mu = 0.3$	
		Slope	Intercept	Slope	Intercept	Slope	Intercept
$\log \epsilon$ vs λ	Depth-Independent	0.136 dex/ 10^3\AA	-7.60 dex	0.170 dex/ 10^3\AA	-7.80 dex	0.177 dex/ 10^3\AA	-7.82 dex
	Athay-Canfield	0.124	-7.53	0.155	-7.70	0.162	-7.71
	de Jager-Neven	0.109	-7.42	0.102	-7.33	0.105	-7.29
	Holweger	0.169	-7.82	0.212	-8.08	0.222	-8.13
	Schmalberger	0.180	-7.88	0.224	-8.16	0.228	-8.18
$\log \epsilon$ vs χ_u	Depth-Independent	-0.129 dex/eV	-6.24 dex	-0.111 dex/eV	-6.38 dex	-0.112 dex/eV	-6.35 dex
	Athay-Canfield	-0.149	-6.12	-0.130	-6.24	-0.137	-6.19
	de Jager-Neven	-0.162	-6.02	-0.192	-5.79	-0.209	-5.65
	Holweger	-0.093	-6.49	-0.059	-6.74	-0.053	-6.76
	Schmalberger	-0.082	-6.57	-0.050	-6.81	-0.050	-6.80
$\log \epsilon$ vs $\log \frac{W}{\lambda}$	Depth-Independent	0.060	-6.63 dex	0.033	-6.81 dex	0.055	-6.68 dex
	Athay-Canfield	0.122	-6.28	0.104	-6.41	0.138	-6.22
	de Jager-Neven	0.188	-5.91	0.345	-5.05	0.421	-4.62
	Holweger	-0.085	-7.44	-0.169	-7.92	-0.170	-7.92
	Schmalberger	-0.123	-7.65	-0.223	-8.22	-0.206	-8.13
Mean $\log \epsilon$	Depth-Independent		-6.94 dex		-6.97 dex		-6.96 dex
	Athay-Canfield		-6.92		-6.95		-6.93
	de Jager-Neven		-6.89		-6.83		-6.78
	Holweger		-7.00		-7.05		-7.05
	Schmalberger		-7.01		-7.07		-7.07

TABLE 6 (Cont'd)

B. Results using CB gf-Values with normalization function removed,
zero-point correction, and χ -dependence removed*

Relation	Microturbulence Model	$\mu = 1.0$		$\mu = 0.5$		$\mu = 0.3$	
		Slope	Intercept	Slope	Intercept	Slope	Intercept
log ϵ vs λ	Depth-Independent	0.113 dex/ 10^3\AA	-6.79 dex	0.146 dex/ 10^3\AA	-6.99 dex	0.154 dex/ 10^3\AA	-7.01 dex
	Athay-Canfield	0.0968	-6.69	0.127	-6.86	0.135	-6.88
	de Jager-Neven	0.0798	-6.58	0.0723	-6.48	0.0747	-6.44
	Holweger	0.151	-7.03	0.195	-7.30	0.205	-7.35
	Schmalberger	0.165	-7.11	0.209	-7.39	0.213	-7.41
log ϵ vs χ_u	Depth-Independent	0.001 dex/eV	-6.24 dex	0.019 dex/eV	-6.37 dex	0.017 dex/eV	-6.35 dex
	Athay-Canfield	0.001	-6.22	0.019	-6.34	0.013	-6.29
	de Jager-Neven	0.001	-6.19	-0.031	-5.97	-0.048	-5.82
	Holweger	0.001	-6.30	0.035	-6.54	0.040	-6.57
	Schmalberger	0.001	-6.31	0.033	-6.55	0.033	-6.55
log ϵ vs $\log \frac{W}{\lambda}$	Depth-Independent	-0.044	-6.47 dex	-0.080	-6.68 dex	-0.062	-6.57 dex
	Athay-Canfield	0.004	-6.20	-0.025	-6.37	0.005	-6.20
	de Jager-Neven	0.058	-5.89	0.205	-5.07	0.276	-4.66
	Holweger	-0.158	-7.12	-0.250	-7.64	-0.254	-7.65
	Schmalberger	-0.189	-7.29	-0.294	-7.89	-0.279	-7.81
Mean log ϵ	Depth-Independent		-6.24 dex		-6.27 dex		-6.26 dex
	Athay-Canfield		-6.22		-6.25		-6.23
	de Jager-Neven		-6.19		-6.13		-6.08
	Holweger		-6.30		-6.35		-6.35
	Schmalberger		-6.31		-6.37		-6.37

* χ -dependence removed using slope in Part A of Table 7 at $\mu = 1.0$

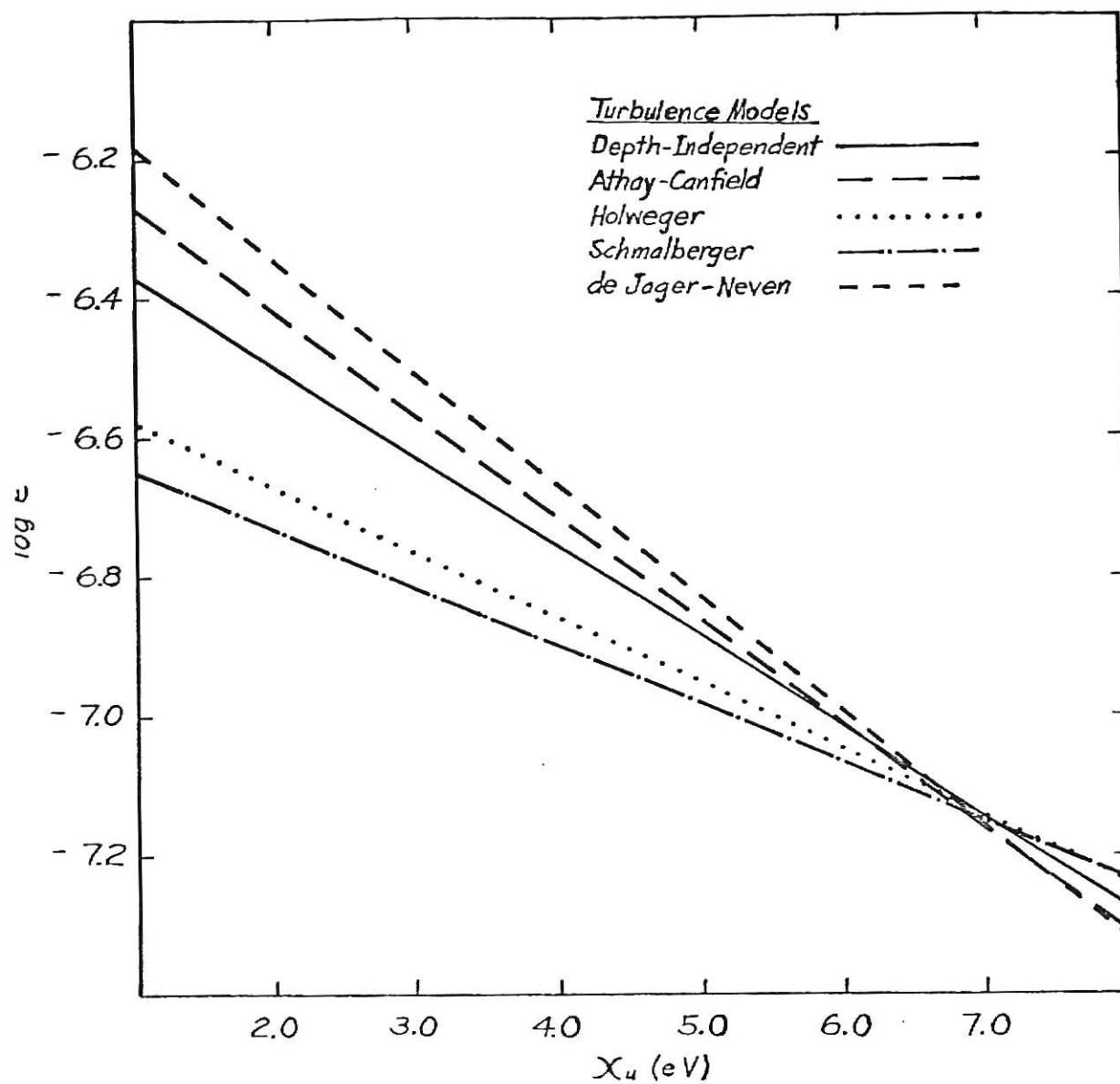


Fig. 24.— The dependence of $\log \epsilon$ on upper excitation potential, obtained from calculations with the Elste thermal model and the five different microturbulence models at $\mu = 1.0$ in part A of table 6.

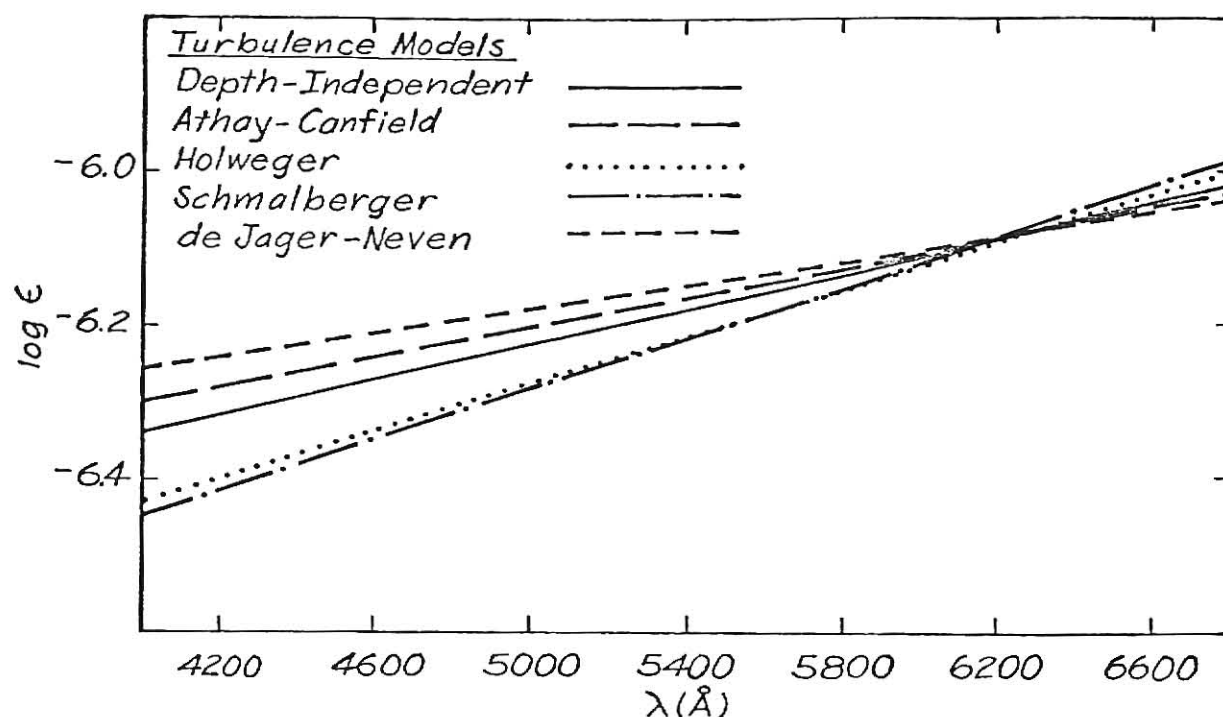


Fig. 25.— The dependence of $\log \epsilon$ on wavelength, obtained from calculations with the Elste thermal model and the five different microturbulence models at $\mu = 1.0$ in part B of table 6.

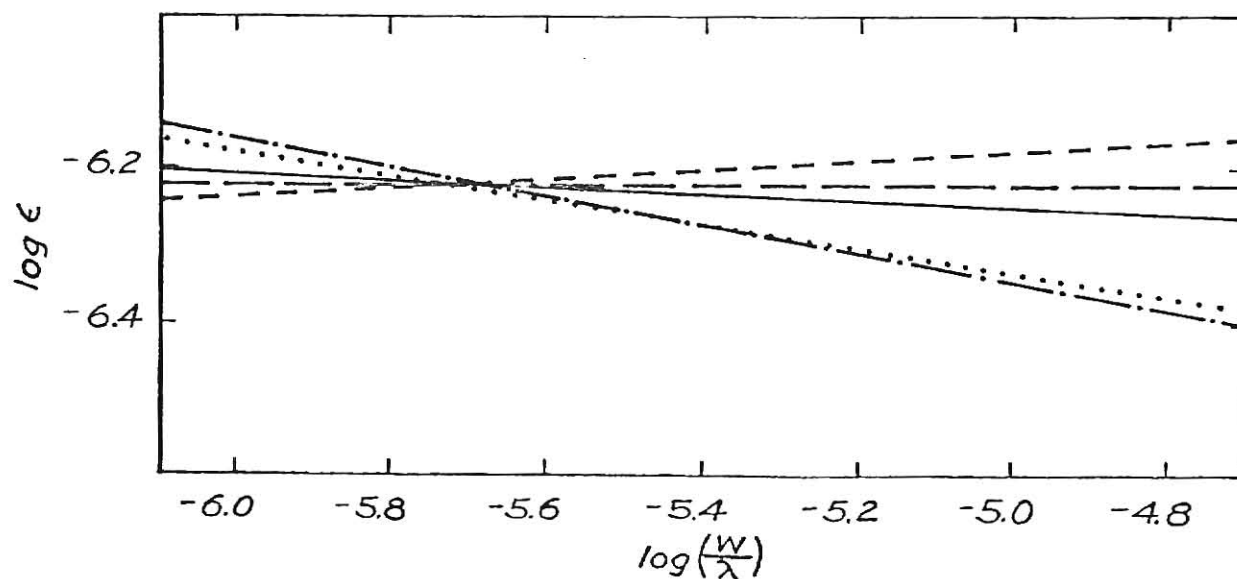


Fig. 26.— The dependence of $\log \epsilon$ on equivalent width, obtained from calculations with the Elste thermal model and the five different microturbulence models at $\mu = 1.0$ in part B of table 6.

and $\log(W/\lambda)$, respectively, after the zero-point error and the χ -dependence have been removed from the gf-values.

Although the effect of the microturbulence is small in this study, this would not be true in studies having a large number of lines on the saturation portion of the curve of growth. Note in figure 26 that the difference between models begins to become significant for lines having equivalent widths on the order of $\log(W/\lambda) = -4.8$.

i) The Final Chromium Abundance Derived from the Corrected
CB gf-Values and the Müller and Mutschlecner Equivalent Widths

Table 7 gives the quantities used to determine the empirical curve of growth and the computed $\log \epsilon$ for each of the 116 lines. These calculations were done with the Elste thermal model and the depth-independent, anisotropic microturbulence model. The first two columns are identical to table 5, while the third gives the lower excitation potential of the line. The gf-values are the CB gf-values, corrected for the zero-point error and χ -dependence. At each limb distance $\log C$, $\log(W/\lambda)$, and the computed $\log \epsilon$ are given; $\log C$ is computed from equation (17), and $\log(W/\lambda)$ is the MM equivalent width.

Table 8 summarizes the results of the computed line abundances in table 7. We have grouped the lines according to their range of excitation potential and the mean abundance for each group is given. The abundances are expressed in the form of the absolute chromium abundance, with $N_H = 12.00$. As mentioned previously, the lines were broken up into groups according to wavelength and excitation potential, and a separate curve of growth computed for each. Eleven curves of growth were used for the 116 lines and the mean abundance for all eleven calculations is given as the mean for all lines in table 8. The last row of table 8 gives the abundance which results from placing all the lines on a single curve of growth, as in figures 21, 22, and 23.

TABLE 7
Final Cr Abundance Analysis

RMT No.	λ in Å	χ_1	$\log gf^*$	$\mu = 1.0$			$\mu = 0.5$			$\mu = 0.3$		
				$\log C$	$\log \frac{W}{\lambda}$	$\log \epsilon$	$\log C$	$\log \frac{W}{\lambda}$	$\log \epsilon$	$\log C$	$\log \frac{W}{\lambda}$	$\log \epsilon$
6	6330.10	0.94	-2.89	1.11	-5.42	-6.13	1.25	-5.32	-6.43	1.33	-5.27	-6.41
8	5072.92	0.94	-2.70	1.30	-5.21	-6.35	1.47	-5.10	-6.36	1.57	-5.06	-6.36
9	4964.93	0.94	-2.74	1.25	-5.15	-6.21	1.41	-5.07	-6.26	1.51	-5.02	-6.21
10	4496.86	0.94	-1.39	2.61	-4.70	-6.34	2.79	-4.68	-6.56	2.89	-4.68	-6.58
	4545.96	0.94	-1.44	2.56	-4.72	-6.56	2.73	-4.69	-6.57	2.84	-4.69	-6.57
	4580.06	0.94	-1.67	2.34	-4.73	-6.20	2.51	-4.70	-6.38	2.61	-4.69	-6.34
18	5296.70	0.98	-1.79	2.19	-4.76	-6.12	2.36	-4.75	-6.30	2.46	-4.74	-6.23
	5300.75	0.98	-2.39	1.59	-4.98	-6.24	1.76	-4.93	-6.31	1.86	-4.90	-6.25
	5247.57	0.96	-1.87	2.13	-4.82	-6.30	2.30	-4.78	-6.37	2.39	-4.78	-6.34
20	5123.47	1.03	-3.03	0.89	-5.51	-6.32	1.06	-5.33	-6.28	1.15	-5.26	-6.26
21	4600.76	1.00	-1.50	2.45	-4.74	-6.35	2.63	-4.73	-6.62	2.73	-4.72	-6.60
	4591.40	0.96	-1.65	2.34	-4.83	-6.62	2.51	-4.79	-6.73	2.61	-4.77	-6.70
	4613.37	0.96	-1.84	2.15	-4.80	-6.31	2.32	-4.78	-6.51	2.43	-4.77	-6.51
22	4351.05	0.96	-1.56	2.40	-4.68	-6.06	2.58	-4.66	-6.26	2.68	-4.66	-6.25
	4412.25	1.03	-2.56	1.34	-5.21	-6.40	1.72	-5.11	-6.45	1.62	-5.07	-6.46
	4373.25	0.98	-2.28	1.25	-5.00	-5.97	1.42	-4.90	-5.96	1.52	-4.88	-5.95
30	4885.77	2.53	-1.35	1.14	-5.27	-6.28	1.28	-5.18	-6.30	1.35	-5.12	-6.25
31	4789.34	2.53	-0.61	1.87	-4.88	-6.32	2.02	-4.87	-6.45	2.09	-4.87	-6.47
	4829.37	2.53	-0.87	1.62	-4.85	-5.99	1.76	-4.80	-6.00	1.84	-4.79	-5.97

* $\log(gf)_{CB_2}$ in TABLE 5

TABLE 7 (Cont'd)

RMT No.	λ in Å	χ_1	$\log gf^*$	$\mu = 1.0$			$\mu = 0.5$			$\mu = 0.3$		
				$\log C$	$\log \frac{W}{\lambda}$	$\log \epsilon$	$\log C$	$\log \frac{W}{\lambda}$	$\log \epsilon$	$\log C$	$\log \frac{W}{\lambda}$	$\log \epsilon$
32	4571.68	2.53	-0.77	1.69	-5.07	-6.53	1.84	-5.02	-6.60	1.91	-4.99	-6.57
	4637.18	2.53	-1.24	1.23	-5.30	-6.41	1.38	-5.22	-6.45	1.45	-5.19	-6.46
	4648.12	2.53	-1.48	0.99	-5.33	-6.21	1.14	-5.22	-6.21	1.21	-5.21	-6.25
	4649.44	2.53	-1.31	1.16	-5.24	-6.26	1.31	-5.16	-6.29	1.38	-5.15	-6.33
33	4529.85	2.53	-1.46	1.00	-5.36	-6.26	1.15	-5.26	-6.27	1.22	-5.24	-6.30
	4541.07	2.53	-1.28	1.18	-5.24	-6.28	1.33	-5.18	-6.34	1.40	-5.15	-6.35
	4535.15	2.53	-1.16	1.30	-5.17	-6.30	1.45	-5.09	-6.32	1.52	-5.08	-6.35
	4539.79	2.53	-1.22	1.24	-5.08	-6.10	1.39	-4.98	-6.07	1.46	-4.97	-6.08
35	4126.52	2.53	-0.57	1.89	-4.93	-6.49	2.05	-4.90	-6.61	2.14	-4.87	-6.56
	4203.57	2.53	-0.98	1.49	-4.90	-6.02	1.65	-4.79	-5.94	1.73	-4.78	-5.93
37	4026.17	2.53	-0.61	1.84	-4.95	-6.48	2.00	-4.93	-6.62	2.09	-4.91	-6.60
38	3984.34	2.53	-0.40	2.05	-4.82	-6.38	2.21	-4.79	-6.50	2.29	-4.77	-6.46
59	5238.97	2.70	-1.54	0.77	-5.49	-6.17	0.88	-5.42	-6.21	0.95	-5.42	-6.25
60	5110.77	2.70	-1.33	0.96	-5.33	-6.17	1.09	-5.19	-6.10	1.15	-5.18	-6.12
61	4745.32	2.70	-1.46	0.83	-5.60	-6.36	0.96	-5.50	-6.38	1.03	-5.47	-6.40
62	4697.06	2.70	-0.96	1.32	-5.21	-6.37	1.46	-5.13	-6.38	1.53	-5.09	-6.35
	4700.62	2.70	-1.18	1.10	-5.50	-6.52	1.24	-5.44	-6.58	1.31	-5.37	-6.55
64	4295.76	2.70	-0.71	1.61	-4.89	-6.12	1.77	-4.77	-6.00	1.85	-4.75	-5.96
	4381.12	2.70	-0.97	1.36	-5.09	-6.25	1.52	-5.01	-6.28	1.59	-4.98	-6.26
65	4120.62	2.70	-0.95	1.35	-5.31	-6.56	1.51	-5.20	-6.56	1.59	-5.18	-6.60
66	4077.07	2.70	-0.94	1.36	-5.21	-6.43	1.51	-5.09	-6.41	1.59	-5.05	-6.39
67	3992.83	2.70	-0.26	2.03	-4.76	-6.18	2.19	-4.73	-6.30	2.26	-4.72	-6.29
	3978.67	2.70	-0.61	1.68	-4.74	-5.76	1.83	-4.69	-5.81	1.91	-4.67	-5.76

TABLE 7 (Cont'd)

RMT No.	λ in Å	χ_1	log gf*	$\mu = 1.0$			$\mu = 0.5$			$\mu = 0.3$		
				log C	$\log \frac{W}{\lambda}$	log ϵ	log C	$\log \frac{W}{\lambda}$	log ϵ	log C	$\log \frac{W}{\lambda}$	log ϵ
81	4619.54	2.97	-0.62	1.43	-5.08	-6.29	1.57	-5.01	-6.30	1.63	-4.98	-6.26
	4501.78	2.90	-1.18	0.93	-5.26	-6.05	1.06	-5.13	-6.00	1.13	-5.11	-6.00
	4622.75	2.97	-1.10	0.95	-5.36	-6.20	1.09	-5.25	-6.19	1.15	-5.22	-6.20
	4501.10	2.90	-0.83	1.28	-5.11	-6.18	1.41	-5.05	-6.22	1.48	-5.03	-6.21
	4498.73	2.90	-0.83	1.28	-5.26	-6.40	1.41	-5.21	-6.46	1.48	-5.18	-6.47
	4432.17	2.86	-0.85	1.29	-5.07	-6.13	1.43	-5.02	-6.18	1.49	-5.01	-6.18
99	4693.95	2.97	-0.71	1.35	-5.26	-6.47	1.48	-5.21	-6.53	1.55	-5.18	-6.54
	4695.16	2.97	-1.11	0.95	-5.47	-6.33	1.08	-5.35	-6.32	1.15	-5.33	-6.35
104	4346.83	2.97	-0.55	1.52	-5.06	-6.36	1.67	-5.02	-6.45	1.74	-5.00	-6.45
119	5719.82	3.00	-1.76	0.23	-6.17	-6.35	0.34	-6.04	-6.34	0.37	-5.97	-6.29
127	4458.53	3.00	-0.38	1.63	-4.95	-6.25	1.76	-4.92	-6.31	1.83	-4.90	-6.27
	4465.36	3.00	-0.94	1.07	-5.29	-6.23	1.20	-5.22	-6.27	1.27	-5.19	-6.27
143	4922.27	3.09	-0.01	1.93	-4.78	-6.06	2.05	-4.77	-6.14	2.11	-4.76	-6.05
	4887.01	3.07	-0.32	1.63	-4.89	-6.09	1.76	-4.83	-6.03	1.81	-4.79	-5.87
	4870.80	3.07	-0.29	1.66	-4.83	-5.95	1.78	-4.79	-5.94	1.84	-4.78	-5.86
	4885.96	3.07	-1.16	0.79	-5.58	-6.30	0.92	-5.43	-6.25	0.97	-5.39	-6.24
144	4836.86	3.09	-1.26	0.67	-5.45	-6.03	0.79	-5.36	-6.03	0.85	-5.34	-6.06
145	4737.35	3.07	-0.25	1.69	-4.91	-6.19	1.81	-4.89	-6.26	1.87	-4.91	-6.30
	4730.71	3.07	-0.34	1.60	-4.99	-6.28	1.72	-4.98	-6.37	1.78	-4.98	-6.38
	4724.42	3.07	-0.71	1.23	-5.17	-6.21	1.35	-5.08	-6.19	1.41	-5.04	-6.14
147	4656.19	3.07	-1.10	0.83	-5.27	-5.96	0.95	-5.16	-5.92	1.01	-5.12	-5.89
150	4540.72	3.09	0.03	1.96	-4.89	-6.45	2.09	-4.86	-6.50	2.15	-4.85	-6.47
	4511.90	3.07	-0.38	1.57	-5.05	-6.38	1.70	-5.01	-6.43	1.76	-4.99	-6.41
166	4954.81	3.11	-0.39	1.53	-5.03	-6.29	1.65	-4.99	-6.32	1.71	-4.97	-6.29
	4936.34	3.10	-0.39	1.54	-5.05	-6.33	1.66	-5.02	-6.39	1.72	-5.01	-6.38

TABLE 7 (Cont'd)

RMT No.	λ in Å	χ_1	$\log gf^*$	$\mu = 1.0$			$\mu = 0.5$			$\mu = 0.3$		
				$\log C$	$\log \frac{W}{\lambda}$	$\log \epsilon$	$\log C$	$\log \frac{W}{\lambda}$	$\log \epsilon$	$\log C$	$\log \frac{W}{\lambda}$	$\log \epsilon$
168	4801.03	3.11	-0.31	1.60	-5.01	-6.32	1.72	-4.97	-6.35	1.78	-4.96	-6.33
170	4680.86	3.08	-1.10	0.82	-5.26	-5.94	0.95	-5.11	-5.84	1.00	-5.08	-5.81
186	4718.43	3.18	0.07	1.90	-4.84	-6.23	2.02	-4.84	-6.33	2.08	-4.83	-6.27
	4708.04	3.15	-0.05	1.81	-4.90	-6.29	1.93	-4.89	-6.38	1.99	-4.87	-6.31
	4689.37	3.11	-0.50	1.40	-5.07	-6.22	1.52	-5.03	-6.27	1.58	-5.00	-6.22
	4669.34	3.15	-0.65	1.21	-5.09	-6.07	1.33	-5.03	-6.08	1.38	-5.00	-6.03
	4666.51	3.13	-0.49	1.38	-5.06	-6.20	1.51	-5.00	-6.20	1.56	-4.97	-6.14
	4664.80	3.11	-0.38	1.51	-4.95	-6.11	1.65	-4.87	-6.03	1.70	-4.86	-5.99
188	5787.99	3.31	-0.58	1.12	-5.21	-6.13	1.22	-5.11	-6.05	1.26	-5.09	-6.01
	5785.82	3.31	-1.07	0.63	-5.38	-5.88	0.73	-5.27	-5.56	0.77	-5.24	-5.52
	5785.00	3.31	-0.98	0.72	-5.35	-5.93	0.82	-5.24	-5.86	0.86	-5.22	-5.85
	5783.93	3.31	-0.88	0.82	-5.23	-5.86	0.92	-5.13	-5.78	0.96	-5.10	-5.73
	5783.11	3.31	-0.74	0.96	-5.38	-6.21	1.06	-5.27	-6.15	1.10	-5.24	-6.12
191	5405.00	3.36	-0.94	0.73	-5.65	-6.31	0.84	-5.56	-6.31	0.88	-5.56	-6.36
	5386.97	3.35	-0.80	0.88	-5.39	-6.16	0.99	-5.33	-6.17	1.03	-5.30	-6.16
193	5221.77	3.36	-0.76	0.90	-5.30	-6.05	1.00	-5.26	-6.09	1.05	-5.20	-6.02
	5214.12	3.35	-0.96	0.71	-5.49	-6.10	0.81	-5.46	-6.17	0.86	-5.44	-6.18
196	4526.11	3.36	-0.95	0.73	-5.45	-6.09	0.85	-5.29	-6.01	0.91	-5.26	-6.01
201	5243.36	3.38	-0.75	0.89	-5.42	-6.20	0.99	-5.36	-6.22	1.03	-5.34	-6.23
	5177.41	3.41	-0.64	0.97	-5.46	-6.33	1.08	-5.39	-6.34	1.13	-5.33	-6.29
	5200.19	3.37	-0.67	0.98	-5.34	-6.19	1.08	-5.25	-6.16	1.13	-5.24	-6.17
203	5702.33	3.43	-0.86	0.72	-5.38	-5.97	0.82	-5.34	-6.00	0.86	-5.31	-5.98
	5628.65	3.41	-0.87	0.72	-5.57	-6.19	0.82	-5.55	-6.28	0.86	-5.55	-6.31
204	5480.50	3.43	-0.92	0.64	-5.74	-6.30	0.74	-5.70	-6.37	0.78	-5.63	-6.33
	5442.41	3.41	-1.15	0.43	-5.79	-6.14	0.53	-5.70	-6.16	0.57	-5.66	-6.15

TABLE 7 (Cont'd)

RMT No.	λ in Å	χ_1	$\log gf^*$	$\mu = 1.0$			$\mu = 0.5$			$\mu = 0.3$		
				$\log C$	$\log \frac{W}{\lambda}$	$\log \epsilon$	$\log C$	$\log \frac{W}{\lambda}$	$\log \epsilon$	$\log C$	$\log \frac{W}{\lambda}$	$\log \epsilon$
206	5193.50	3.41	-1.12	0.49	-5.64	-6.05	0.59	-5.57	-6.08	0.64	-5.51	-6.05
225	5272.00	3.43	-0.63	0.97	-5.29	-6.11	1.07	-5.28	-6.19	1.11	-5.25	-6.17
	5287.18	3.42	-1.21	0.40	-5.72	-6.04	0.50	-5.61	-6.03	0.55	-5.61	-6.08
	5304.18	3.43	-0.95	0.63	-5.55	-6.10	0.73	-5.52	-6.16	0.78	-5.50	-6.17
	5312.86	3.43	-0.80	0.80	-5.52	-6.23	0.90	-5.42	-6.21	0.95	-5.40	-6.21
	5318.78	3.42	-0.81	0.80	-5.58	-6.30	0.90	-5.50	-6.31	0.95	-5.40	-6.21
	5344.76	3.43	-1.21	0.39	-5.85	-6.17	0.50	-5.81	-6.26	0.54	-5.79	-6.26
	5340.46	3.42	-1.04	0.57	-5.52	-6.00	0.68	-5.43	-5.99	0.72	-5.41	-6.00
231	4767.86	3.54	-0.53	0.97	-5.50	-6.39	1.08	-5.42	-6.40	1.13	-5.40	-6.41
233	4622.49	3.54	-0.13	1.36	-5.07	-6.19	1.48	-5.02	-6.20	1.52	-5.01	-6.19
234	4413.85	3.54	-0.26	1.29	-5.20	-6.36	1.42	-5.15	-6.47	1.48	-5.14	-6.50
239	5694.74	3.84	-0.51	0.69	-5.48	-6.05	0.77	-5.45	-6.10	0.80	-5.45	-6.12
	5642.39	3.84	-1.02	0.17	-5.97	-6.08	0.25	-5.97	-6.18	0.28	-5.86	-6.08
	5649.39	3.82	-0.82	0.39	-5.75	-6.06	0.47	-5.71	-6.12	0.50	-5.71	-6.14
243	5746.42	3.83	-1.29	-0.08	-6.18	-6.05	0.00	-6.17	-6.13	0.03	-6.16	-6.12
247	4263.14	3.83	0.38	1.66	-4.93	-6.46	1.78	-4.89	-6.53	1.83	-4.90	-6.55
248	4209.36	3.83	0.39	1.67	-5.16	-6.69	1.78	-5.12	-6.80	1.83	-5.09	-6.79
249	4208.36	3.83	-0.08	1.20	-5.42	-6.46	1.31	-5.32	-6.52	1.36	-5.30	-6.53
251	4039.10	3.83	0.68	1.96	-4.93	-6.74	2.05	-4.89	-6.81	2.10	-4.87	-6.83
261	4131.36	3.83	-0.00	1.28	-5.29	-6.41	1.38	-5.19	-6.47	1.43	-5.15	-6.46
	4152.77	3.83	-0.16	1.12	-5.28	-6.25	1.22	-5.19	-6.31	1.27	-5.16	-6.31
272	4204.46	3.96	0.09	1.26	-5.45	-6.53	1.36	-5.39	-6.63	1.40	-5.34	-6.62
282	6661.08	4.17	-0.34	0.55	-5.78	-6.23	0.62	-5.71	-6.24	0.64	-5.71	-6.26
	6669.31	4.16	-0.60	0.30	-6.08	-6.31	0.36	-6.03	-6.34	0.38	-6.00	-6.29

TABLE 8

Final Cr Abundances Derived for Different Ranges of Lower Excitation
Potential at Three Positions on the Solar Disk

χ_1 (eV)	$\log N_{\text{cr}}$			No. of Lines
	$\mu = 1.0$	$\mu = 0.5$	$\mu = 0.3$	
0.9 - 1.0	5.72	5.60	5.62	16
2.5 - 2.7	5.72	5.69	5.70	26
2.8 - 3.2	5.78	5.76	5.79	33
3.3 - 3.6	5.86	5.86	5.87	28
3.7 - 4.2	5.67	5.60	5.61	13
Mean for all lines	5.77	5.73	5.75	116
All lines on one curve of growth	5.78	5.74	5.76	116

Using the mean abundances at the three limb distances and the observed scatter of points on the curves of growth, we find the mean abundance of chromium to be $N_{\text{Cr}} = 5.75 \pm 0.15$. This confirms the CSE result of $N_{\text{Cr}} = 5.80 \pm 0.11$.

j) Conclusions

This study has led to the following conclusions on solar LTE curve of growth abundance calculations:

(i) The largest source of error in the abundance calculations is in the gf-values. The fundamental difference between our results and those of Müller and Mutschlecner has been from our use of the 0.7 dex zero-point correction to the CB gf-values.

(ii) Other systematic errors in the gf-values and the equivalent widths do not appreciably affect the computed abundance when a statistically large sample of lines is used, provided that the distribution in equivalent width is reasonably uniform, including weak lines.

(iii) The dependence of the chromium abundance on the thermal model is small, causing differences in the mean abundance of 0.15 dex or less among the three models.

(iv) The dependence of the chromium abundance on the microturbulence model is somewhat larger, but surprisingly small in view of the differences in the models. The mean abundances derived using the five models differ most at $\mu = 0.3$, where they vary by about 0.3 dex.

(v) No indication of departure from conditions of LTE is seen. The center-to-limb variation in the mean abundance for all 116 lines is less than 0.05 dex, confirming the conclusion of Müller and Mutschlecner that there is no center-to-limb effect.

REFERENCES

- Aller, L. H. 1960, in Stellar Atmospheres, ed. J. L. Greenstein (Chicago: University of Chicago Press), p. 156.
- _____. 1963, Astrophysics: The Atmospheres of the Sun and Stars (2nd ed.; New York: The Ronald Press Company).
- Aller, L. H., Elste, G., and Jugaku, J. 1957, Ap. J. Suppl., No. 25, 3, 1.
- Athay, R. G. 1970, Ap. J., 161, 713.
- _____. 1972, Radiation Transport in Spectral Lines (Dordrecht, Holland: D. Reidel Publishing Company).
- Athay, R. G., and Canfield, R. C. 1969, Ap. J., 156, 695.
- Bell, R. A., and Upson, W. L. 1971, Ap. Letters, 9, 109.
- Brault, J. W., Slaughter, C. D., Pierce, A. K., and Aikens, R. S. 1971, Solar Phys., 18, 366.
- Brault, J. W., and Testerman, L. K. 1972, Preliminary Edition of the Kitt Peak Solar Atlas, Kitt Peak National Observatory.
- Bridges, J. M., and Wiese, W. L. 1970, Ap. J. (Letters), 161, L71.
- Byard, P. L. 1968, J. Quant. Spectrosc. and Rad. Transf., 8, 1543.
- Cocke, C. L., Curnutte, B., and Brand, J. 1971, Astr. and Ap., 15, 299.
- Cocke, C. L., Stark, A., and Evans, J. C. 1973, Ap. J., 184, 653.
- Corliss, C. H., and Bozman, W. R. 1962, Experimental Transition Probabilities for Spectral Lines of Seventy Elements (NBS Monograph 53).
- Corliss, C. H., and Warner, B. 1966, Res. N.B.S., 70A, 325.
- Cowley, C. R. 1970, The Theory of Stellar Spectra (New York: Gordon and Breach).
- de Jager, C., and Neven, L. 1972, Solar Phys., 25, 277.
- Dreiling, L. A. 1970, M.S. thesis, Kansas State University.
- Edmonds, F. N., and Webb, C. J. 1972, Solar Phys., 25, 44.
- Elste, G. 1967, Ap. J., 148, 857.
- Evans, J. C. 1966, Ph.D. thesis, University of Michigan.
- Evans, J. C., and Elste, G. 1971, Astr. and Ap., 12, 428.

- Evans, J. C., and Schroeder, L. W. 1972, Pub. A.S.P., 84, 454.
- Foy, R. 1972, Astr. and Ap., 18, 26.
- Gingerich, O., de Jager, C. 1968, Solar Phys., 3, 5.
- Gingerich, O., Noyes, R. W., Kalkofen, W., and Cuny, Y. 1971, Solar Phys., 18, 347.
- Goldberg, L., Müller, E. A., and Aller, L. H. 1960, Ap. J. Suppl., No. 45, 5, 1.
- Gray, D. F., and Evans, J. C. 1973, J. Roy. Astr. Soc. Can., 67, 241.
- Gussman, E. A. 1967, Z. Astrophys., 65, 456.
- Hill, A. J., and King, R. B. 1951, J. Opt. Soc. Am., 41, 315.
- Holweger, H. 1967, Z. Astrophys., 65, 365.
- Huber, M., and Tobey, F. L. 1968, Ap. J., 152, 609.
- Labs, D., and Neckel, H. 1968, Z. Astrophys., 69, 1.
- Mihalas, D. 1970, Stellar Atmospheres, (San Francisco: W. H. Freeman and Company).
- Minneart, M., Mulders, G.F.W., and Houtgast, J. 1940, Photometric Atlas of the Solar Spectrum (Amsterdam: Schnabel).
- Mohler, O. C., Pierce, A. K., McMath, R. R., and Goldberg, L. 1950, Photometric Atlas of the Near Infrared Solar Spectrum (Ann Arbor: University of Michigan Press).
- Mohler, O. C., and Teske, R. 1961, unpublished photoelectric tracings of the solar spectrum.
- Moore, C. E. 1945, A Multiplet Table of Astrophysical Interest (NBS Technical Note 36).
- Moore, C. E., Minneart, M.G.J., and Houtgast, J. 1966, The Solar Spectrum 2935 Å to 8770 Å (NBS Monograph 61).
- Müller, E. A., and Mutschlecner, J. P. 1964, Ap. J. Suppl., No. 85, 9, 1.
- Nichols, C. S. 1970, M.S. thesis, Kansas State University.
- Pagel, B.E.J. 1965, Proc. 2nd Harvard-Smithsonian Conf. Stellar Atm., Cambridge, Massachusetts.
- Pecker, J. C. 1957a, Comp. Rend., 245, 499.
- _____. 1957b, ibid., 245, 639.

- Pierce, A. K. 1964, Appl. Opt., 3, 1337.
- _____. 1969, Solar Phys., 6, 498.
- Ramsey, L. W. 1973, M.S. thesis, Kansas State University.
- Schmalberger, D. C. 1963, Ap. J., 138, 693.
- Warner, B. 1964a, M.N.R.A.S., 127, 413.
- _____. 1964b, ibid., 128, 63.
- Wenstrand, D. 1972, Ph.D. thesis, Kansas State University.
- Wiese, W. L. 1970, Nuc. Inst. and Meth., 90, 25.
- Withbroe, G. L. 1969, Solar Phys., 9, 19.
- Wolnik, S. J., Berthel, R. O., Carnevale, E. H., and Wares, G. W. 1969, Ap. J., 157, 983.
- Wolnik, S. J., Berthel, R. O., Larson, G. S., Carnevale, E. H., and Wares, G. W. 1968, Phys. Fluids, 11, 1002.
- Wolnik, S. J., Berthel, R. O., and Wares, G. W. 1970, Ap. J., 162, 1037.

A STUDY OF THE LTE CURVE OF GROWTH METHOD AS USED IN
THE DETERMINATION OF THE SOLAR CHROMIUM ABUNDANCE

by

GARY JOHN GARWOOD

B.S., Kansas State University, 1967

AN ABSTRACT OF A MASTER'S THESIS

submitted in partial fulfillment of the

requirements for the degree

MASTER OF SCIENCE

Department of Physics

KANSAS STATE UNIVERSITY
Manhattan, Kansas

1974

The solar chromium abundance has been determined as a study of the LTE curve of growth method. Attention was given to the effect of known and suspected systematic errors in the laboratory gf-values and measured line equivalent widths. The gf-values of Corliss and Bozman (1962 NBS monograph No. 53) and the equivalent widths of Müller and Mutschlecner (1964 Ap. J. Suppl., 9, 1) at limb positions of $\mu = 1.0, 0.5$, and 0.3 for 116 Cr I lines were used in the investigation. The CB gf-values were corrected for a 0.7 dex zero-point error found by Cocke, Stark, and Evans (1973 Ap. J., 184, 653), and the erroneous CB normalization function was removed. The computed line abundances were analyzed for dependence on wavelength, excitation potential, and line equivalent width.

The theoretical curves of growth were calculated for three different homogeneous thermal models and five different microturbulence models to determine the influence of model-dependent effects on the mean abundance.

The computed line abundances gave a strong indication of a linear excitation-dependent error in the gf-values and this was removed before computing the mean abundance. The mean abundance is not strongly dependent on either the thermal or microturbulence model. No significant center-to-limb variation in the abundance was found which might be indicative of a departure from LTE. The mean chromium abundance was found to be

$$\log N_{\text{Cr}} = 5.75 \pm 0.15.$$